AD_____

GRANT NUMBER DAMD17-94-J-4133


TITLE:  A Study of Ultrasonic Wavefront Distortion Compensation


PRINCIPAL INVESTIGATOR:  Qing Zhu, Ph.D.


CONTRACTING ORGANIZATION:  University of Pennsylvania
                           Philadelphia, Pennsylvania   19104-3246


REPORT DATE:  September 1997


TYPE OF REPORT:  Annual


PREPARED FOR:  Commander
               U.S. Army Medical Research and Materiel Command
               Fort Detrick, Frederick, Maryland   21702-5012


DISTRIBUTION STATEMENT:  Approved for public release;
                         distribution unlimited


The views, opinions and/or findings contained in this report are
those of the author(s) and should not be construed as an official
Department of the Army position, policy or decision unless so
designated by other documentation.


19980226 068    DTIC QUALITY INSPECTED 3

| REPORT DOCUMENTATION PAGE | | Form Approved OMB No. 0704-0188 |
|---|---|---|

Public reporting burden for this collection of information is estimated to average 1 hour per response, including the time for reviewing instructions, searching existing data sources, gathering and maintaining the data needed, and completing and reviewing the collection of information. Send comments regarding this burden estimate or any other aspect of this collection of information, including suggestions for reducing this burden, to Washington Headquarters Services, Directorate for Information Operations and Reports, 1215 Jefferson Davis Highway, Suite 1204, Arlington, VA 22202-4302, and to the Office of Management and Budget, Paperwork Reduction Project (0704-0188), Washington, DC 20503.

| 1. AGENCY USE ONLY (Leave blank) | 2. REPORT DATE September 1997 | 3. REPORT TYPE AND DATES COVERED Annual (1 Sep 96 - 31 Aug 97) |
|---|---|---|

| 4. TITLE AND SUBTITLE | 5. FUNDING NUMBERS |
|---|---|
| A Study of Ultrasonic Wavefront Distortion Compensation | DAMD17-94-J-4133 |

**6. AUTHOR(S)**

Qing Zhu, Ph.D.

| 7. PERFORMING ORGANIZATION NAME(S) AND ADDRESS(ES) | 8. PERFORMING ORGANIZATION REPORT NUMBER |
|---|---|
| University of Pennsylvania Philadelphia, Pennsylvania 19104-3246 | |

| 9. SPONSORING/MONITORING AGENCY NAME(S) AND ADDRESS(ES) | 10. SPONSORING/MONITORING AGENCY REPORT NUMBER |
|---|---|
| Commander U.S. Army Medical Research and Materiel Command Fort Detrick, Frederick, Maryland 21702-5012 | |

**11. SUPPLEMENTARY NOTES**

| 12a. DISTRIBUTION / AVAILABILITY STATEMENT | 12b. DISTRIBUTION CODE |
|---|---|
| Approved for public release; distribution unlimited | |

**13**

High resolution and high contrast ultrasound imaging for early detection of breast lesions is limited by acoustic wavefront distortion which is developed as coherent waves propagate inside the breast tissue. Wavefront distortion causes image degradation. We have developed a novel signal processing technique, called Toward Inverse Filtering (TIF), to compensate such distortion. *In vitro* one-way distortion compensation has shown that contrast resolution has been improved significantly with TIF. We have applied TIF to two-way pulse-echo imaging data obtained from phantom. Preliminary results have shown that TIF offers more improvement of contrast of low echogenic lesions than existing compensation techniques. In addition to signal processing work, we have fabricated a prototype two-dimensional (2-D) ultrasound array operating at 1 MHz. Two-dimensional array will allow us to implement TIF in 2-D for further contrast improvement and will be used as a tool for clinical studies. In addition to wavefront compensation and array construction work, we have developed a novel method which combines ultrasound and near infrared diffused light to improve lesion detection sensitivity and specificity. This work was not proposed in original proposal but it is an important discovery along the track of the PI's breast cancer research.

| 14. SUBJECT TERMS Breast Cancer | | | 15. NUMBER OF PAGES 93 |
|---|---|---|---|
| | | | 16. PRICE CODE |

| 17. SECURITY CLASSIFICATION OF REPORT Unclassified | 18. SECURITY CLASSIFICATION OF THIS PAGE Unclassified | 19. SECURITY CLASSIFICATION OF ABSTRACT Unclassified | 20. LIMITATION OF ABSTRACT Unlimited |
|---|---|---|---|

NSN 7540-01-280-5500

Standard Form 298 (Rev. 2-89)
Prescribed by ANSI Std. Z39-18
298-102

# FOREWORD

Opinions, interpretations, conclusions and recommendations are those of the author and are not necessarily endorsed by the U.S. Army.

_____ Where copyrighted material is quoted, permission has been obtained to use such material.

_____ Where material from documents designated for limited distribution is quoted, permission has been obtained to use the material.

_____ Citations of commercial organizations and trade names in this report do not constitute an official Department of Army endorsement or approval of the products or services of these organizations.
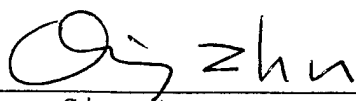
_____ In conducting research using animals, the investigator(s) adhered to the "Guide for the Care and Use of Laboratory Animals," prepared by the Committee on Care and Use of Laboratory Animals of the Institute of Laboratory Resources, National Research Council (NIH Publication No. 86-23, Revised 1985).

_____ For the protection of human subjects, the investigator(s) adhered to policies of applicable Federal Law 45 CFR 46.

_____ In conducting research utilizing recombinant DNA technology, the investigator(s) adhered to current guidelines promulgated by the National Institutes of Health.

_____ In the conduct of research utilizing recombinant DNA, the investigator(s) adhered to the NIH Guidelines for Research Involving Recombinant DNA Molecules.

_____ In the conduct of research involving hazardous organisms, the investigator(s) adhered to the CDC-NIH Guide for Biosafety in Microbiological and Biomedical Laboratories.


_____     9/29/97
PI - Signature                           Date

## INTRODUCTION

The objective of this research is to exploit signal processing methods to improve ultrasound resolution in the detection and classification of small breast lesions. Ultrasound is routinely used in conjunction with conventional x-ray mammography for the evaluation of variety of breast masses, and it is particularly useful for the differentiation of solid from cystic breast lesions. However, ultrasound resolution is limited and the major obstacle for the achievement of high resolution is acoustic wavefront distortion which is developed as coherent waves propagate through the inhomogeneous breast [1-6]. The primary distortion effect is the scattering of coherent energy. As a result, the target strength is reduced, the image lobe is broadened [1-2], the background level is increased and therefore the image contrast is reduced [7]. The secondary distortion effect is the multipath interference which produces ghost image artifacts or false targets in addition to true targets in the image [3]. Adaptive compensation of wavefront distortion is an active area of current research [8]. Two basic *phase* deaberration algorithms have been developed in [9-11]. These algorithms adjust time delays of received waveforms at different elements of a phased array to compensate delay errors due to an inhomogeneous medium and consequently reduce the scattered energy. These phase deaberration algorithms are very useful to partially remove phase distortion and build up the strength of the coherent field. Wavefront amplitude distortion remains, as does residual phase distortion, and produces a significantly high background level in the image. Measurements of 44 in *vivo* breasts obtained from the Hospital of the University of Pennsylvania have shown that this background level in the image caused by the amplitude distortion is 17 dB higher than that obtained from a homogeneous medium [5].

The simple models of Fig. 1 illustrate the effects of wavefront distortion upon a point source image or its angular spectrum (intensity distribution), and the effects of phase deaberration. Without medium induced distortion, the diffraction-limited coherent spectrum is shown in Fig. 1a. With medium induced scattering, the overall angular spectrum is the sum of coherent and scattered spectra [12] as shown in Fig. 1b. Because of scattering, the spectrum is broadened and reduced in strength. The background level is increased and, therefore, image contrast is reduced. A phase deaberration process removes some of phase distortion and therefore strengthens the coherent spectrum as shown in Fig. 1c; yet a significantly high incoherent background level remains in the spectrum due to residual phase errors and wavefront amplitude distortion. Any phase-deaberration procedure that provides a better phase error estimate would reduce this background level [13]. Algorithms that compensate wavefront amplitude distortion can further reduce this background level [13] . In multipath interference (Fig. 1d) the scattered energy removed by the phase deaberration process strengthens the primary spectrum (sharp peak) by folding the removed scattered energy into the primary field. The result is improvement in the ratio of primary to interference lobe level (Fig. 1e).
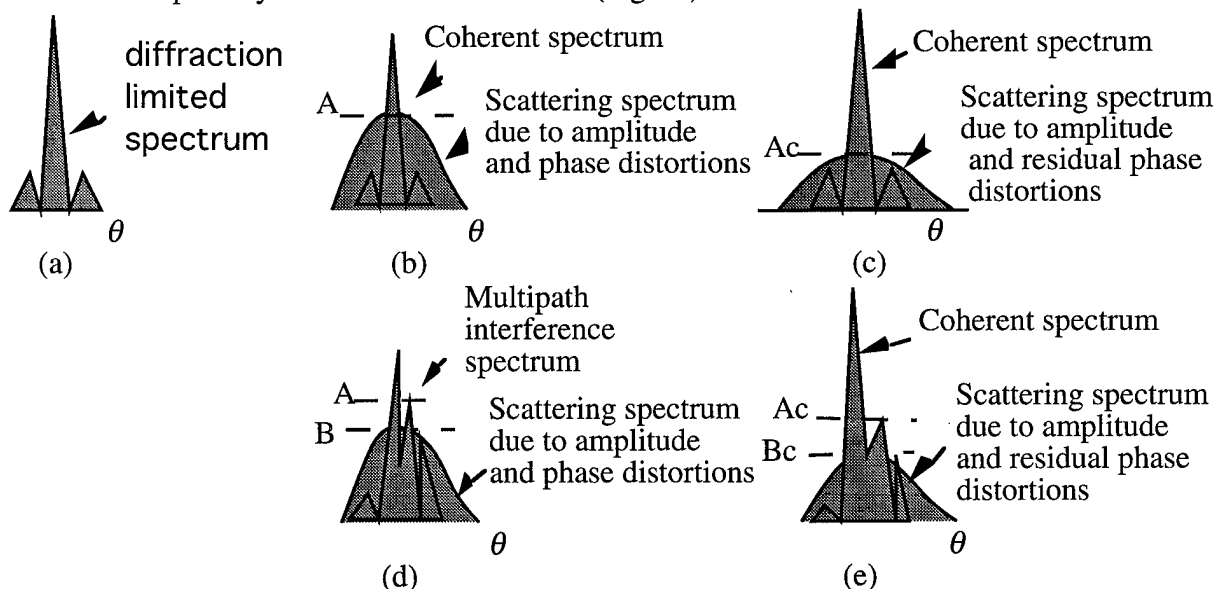


Fig. 1. Statistical models of angular source intensity distribution. (a) diffraction limited spectrum. (b) Scattering induced distortion. The spectrum is the sum of coherent spectrum and scattering spectrum. (c) After phase compensation of (b). (d) Multipath interference and scattering induced distortion. (e) After phase compensation of (d).

Full compensation of wavefront distortion presents a more difficult problem because there is no general way to reduce wavefront amplitude distortion. Liu and Waag [14] have improved time-delay compensation by backpropagating the received waveforms to an optimal distance and then performing time-delay compensation at this distance. Backpropagation partially compensates waveform distortion produced by wave propagation from the backpropagation distance to the receiving aperture. We have developed a novel spectrum amplitude compression technique, we call toward inverse filtering (TIF), during the first two years of this project for this purpose [7,13] (see Appendices A and B). Spectrum amplitude refers to the complex modulus at each discrete frequency within the signal band. TIF ,when used in combination with phase deaberration and backpropagation, provides a general means for reducing wavefront amplitude distortion and therefore reducing the incoherent background level in the image.

High resolution, high contrast breast imaging implies seeing a black cyst 60 dB weaker than a brightly speckled target. This implies that 30 dB contrast has to be achieved in one-way transmission and reception. Time-delay algorithms have been applied to *in vivo* breast data measured from one-dimensional phased arrays [2,5] and the improvement in image contrast is not significant. The ideal adaptive compensation must be a two dimensional (2-D) problem of capturing the entire 2-D wavefront and constructing a 2-D compensation vector for the array [15-16]. In the last two years, we found that by applying time-delay correction to *in vitro* one-way 2-D breast data, the algorithms suppressed scattered energy and folded it into the target image, restoring the mainlobe diffraction shape to the -20 dB region. [6,17]. We also found that an additional 4-5 dB improvement can be obtained by applying Liu and Waag's algorithm [13]. Additionally, with TIF, we are able to improve all the correction algorithms and restore the mainlobe diffraction shape down to -30 dB [13] which is the necessary one-way condition to image small breast lesions and lesion architecture.

There are two remaining tasks that need to be completed before we can apply wavefront compensation algorithms to clinical patients. First, we have demonstrated 30 dB suppression of the distortion sidelobes in one-way propagation experiments, and we need to further demonstrate that TIF is useful in two-way pulse-echo imaging. Second, 2-D compensation requires 2-D transducer arrays which are not commercially available. Therefore, we need to develop a 2-D array to implement wavefront compensation algorithms.

In our original proposal, we proposed to design a 2-D concave transducer which would reduce breast-curvature caused refractive-distortion effects upon images in addition to being a tool for implementing 2-D compensation algorithms. However, concave shape introduces complications in array design and fabrication. Since breast-curvature caused distortion effects can be largely reduced by using a planar transducer compressing against the examined breast, we have focused our research on design and fabrication of such a 2-D planar array.

In this report, we present our preliminary experimental results of wavefront compensation, using two-way pulse-echo phantom data. We also give our progress report on the development of a 2-D array. Deabrration results are reported in Part A and array development is in Part B.

In addition to ultrasonic wavefront deaberration and 2-D array fabrication work, we have done new work on coupling ultrasound and near infrared diffused light imaging methods. The objective is to increase detection sensitivity and specificity of breast lesions. Experimental results with phantoms are very encouraging, and clearly indicate that this novel method could be potentially very important. This work was not proposed in the original proposal, but it is directly related to PI's breast cancer research. Therefore, it is reported in Part C and the preprint submitted for publication is in Appendix C.

## PART A. WAVEFRONT COMPENSATION IN PULSE-ECHO USING TIF

### I. EXPERIMENTS AND DATA PROCESSING

The two-way pulse-echo data were down loaded from the world-wide web at http://bul.eecs.umich.edu and the detailed description of the data can be found in [A1]. Briefly, all data sets were acquired with a 1-D, 64-element, 15.4-mm array operating at 3.33 MHz with a fractional bandwidth of about 35%. Each complete data set consisting of 4096 RF A-scans sampled at a rate of 17.66 MHz with 10 Bit analog-to-digital conversion.

'Each record represents a single element acting as a transmitter and an independent element acting as a receiver. Three data sets were obtained from a standard graphite-gel AIUM resolution phantom with three aberration plates, made of RTV silicone rubber, placed between the transducer array and the phantom. The first plate introduces only a very small defocusing, and hence, is used as the control plate or reference plate. The second plate causes phase distortions less than $\pi$, while the third plate produces phase distortions within $2\pi$. In our preliminary experiments, we have selected first and third data sets and refer to these data sets as Plate 0 and Plate 2.

B-scan images without any correction were formed using conventional shift-and-add beamforming process upon these two data sets. The simple time-delay phase deaberration algorithm [A2] was used to correct phase errors of Plate 2. TIF was implemented after time domain phase correction and the steps were shown in the following diagram (right). First, Fast Fourier Transforms (FFT) of temporal waveforms at each element position of aperture were taken within a selected range window. Let complex signal at element position n of discrete frequency bin number m be represented as $A_m(n)e^{j\phi_m(n)}$. TIF Nth root operation was performed upon amplitude $A_m(n)$ and the resulting complex signal was $\sqrt[N]{A_m(n)}\,e^{j\phi_m(n)}$. Only square root was used in our experiments, because of signal-to-noise ratio consideration. Inverse FFTs of $\sqrt[N]{A_m(n)}\,e^{j\phi_m(n)}$ at each element position were taken to obtain *processed* RF signals. B-scan images were formed using shift-and-add upon *processed* RF signals. All images were formed with fixed focusing on transmission and reception.
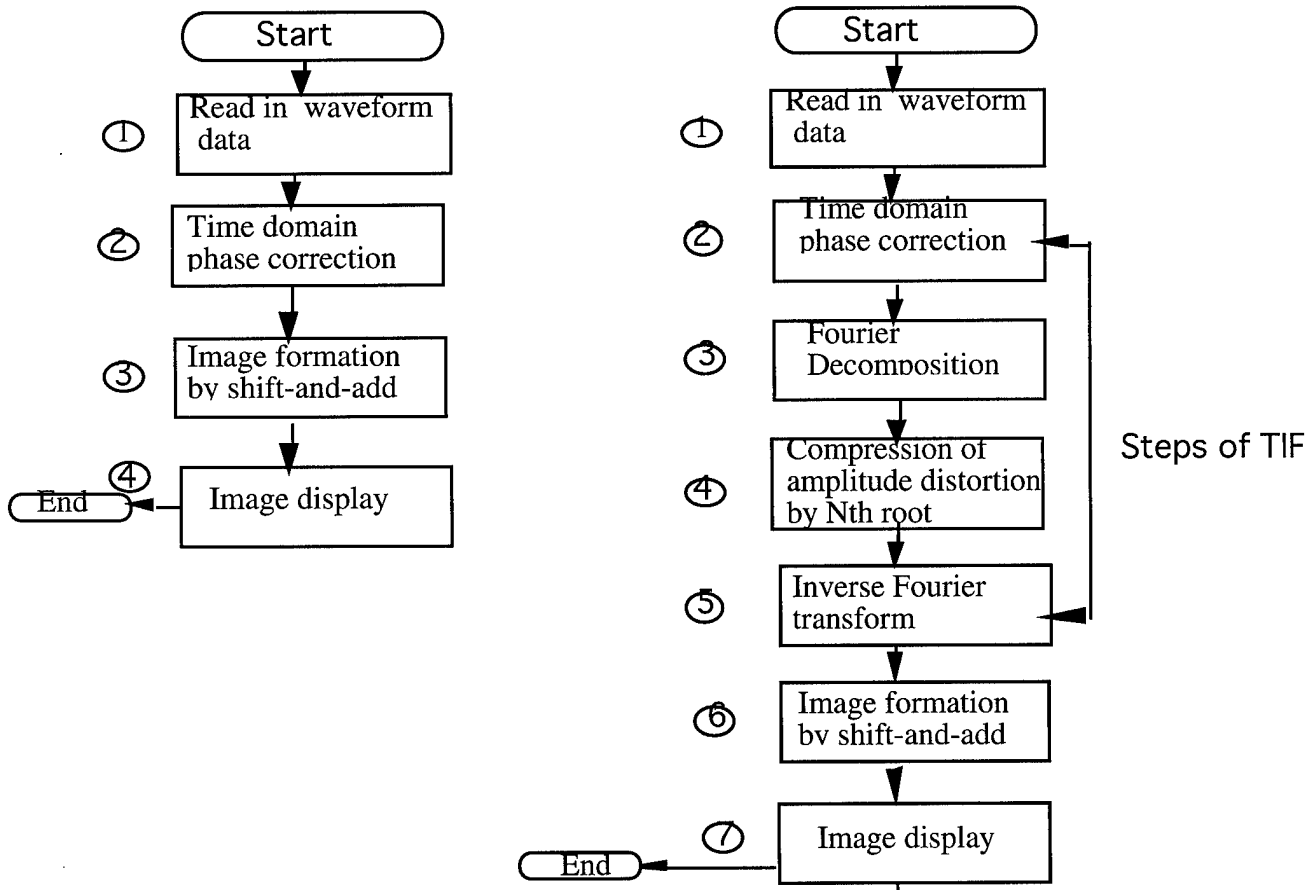
Fig.a1. Diagram of image formation with time-delay correction (left) and TIF correction (right).

## II. PRELIMINARY RESULTS

Fig.a2 is the B-scan image of Plate 0 and is used as the reference image. Several bright targets (wires) and two anechoic regions ("cysts") are shown in the figure. Wire targets allow us to evaluate 2-way system point-spread function and cysts allow us to evaluate system contrast resolution. Since cysts and most tumors appear anechoic, deaberration procedures should make them more "black" in order to identify them. A portion of B-scan images of Plate 2 is shown in Fig.a3. Because of the limitation of computing power, only the portion which contains the wire targets and the lower anechoic region in Fig.a2 is computed and shown in Fig.a3. The images shown in Fig.3a are results of no correction (part a), with phase correction (par b) and TIF correction (part c). Comparing parts a and b, we can see that the system point-spread function is improved by phase deaberration. The sidelobes of the close by wire target as pointed by upper arrows in both images are improved. However, the contrast improvement of anechoic region is marginal. With TIF correction (part c), the anechoic region is beginning to show up. There results are first, and clearly indicate that TIF offers better improvements on low contrast lesions.

## III. FUTURE WORK

We will further quantify the improvement brought about by TIF by measuring the contrast ratio of energy inside and outside aneconic regions. In addition, theoretical work will be undertaken to study the optimal compression parameter of TIF. Finally, the amplitude distribution as a function of the TIF compression parameter will be studied. Statistics of amplitude distribution are useful for tissue characterization.
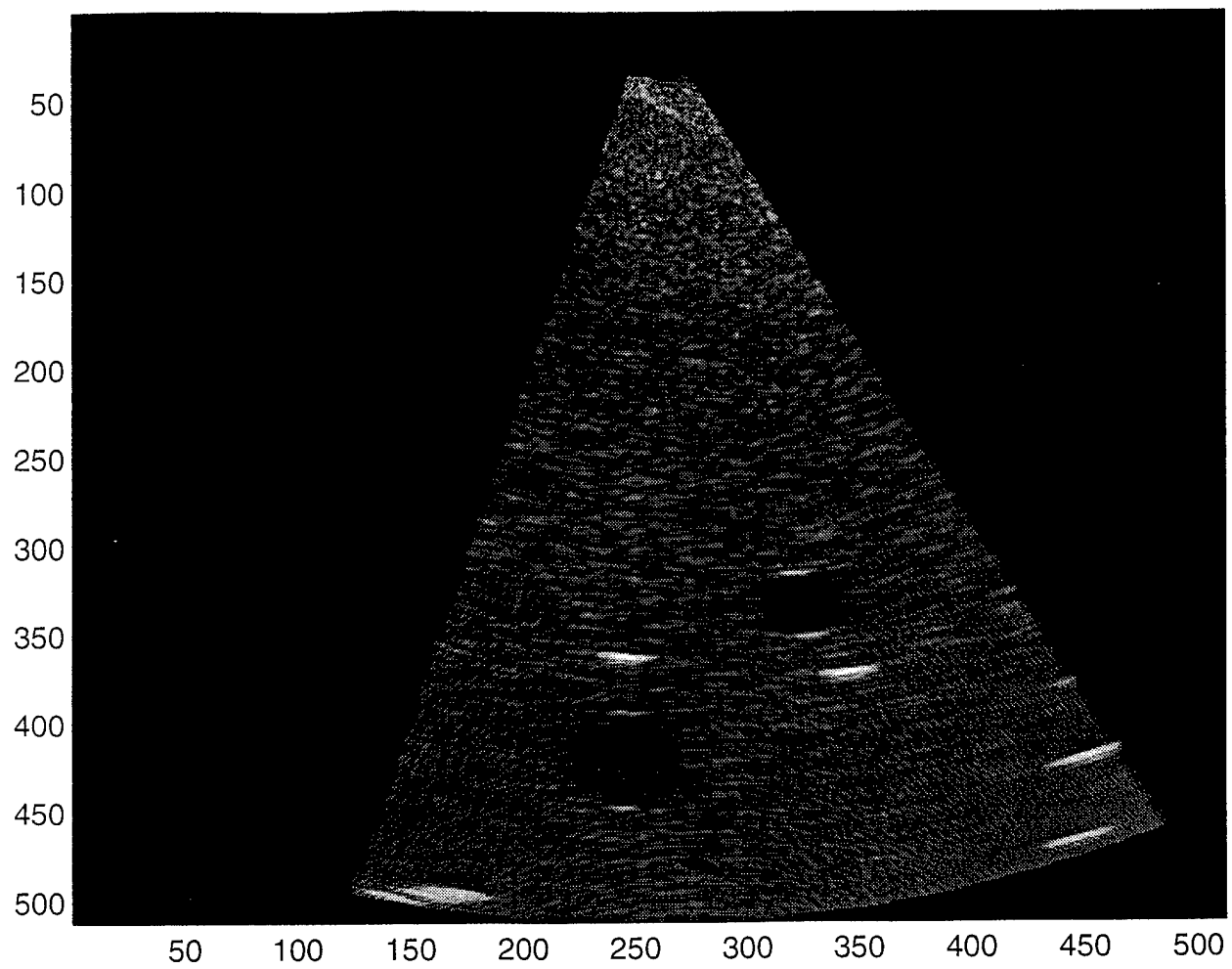
Fig.a2. B-Scan image of Plate 0. Wires are shown as bright targets and low contrast objects ("cysts") are shown as anechoic regions.
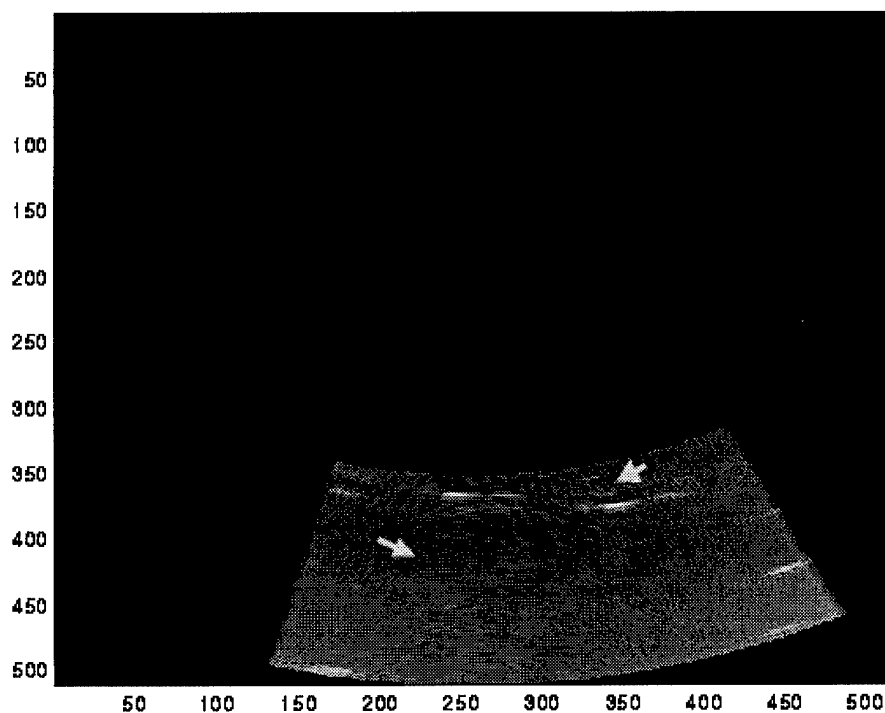
Plate 2, no correction

Fig.a3a. A portion of B-scan image of Plate 2. Upper arrow points to the sidelobes of the close by wire target and lower arrow points to the anechoic region.
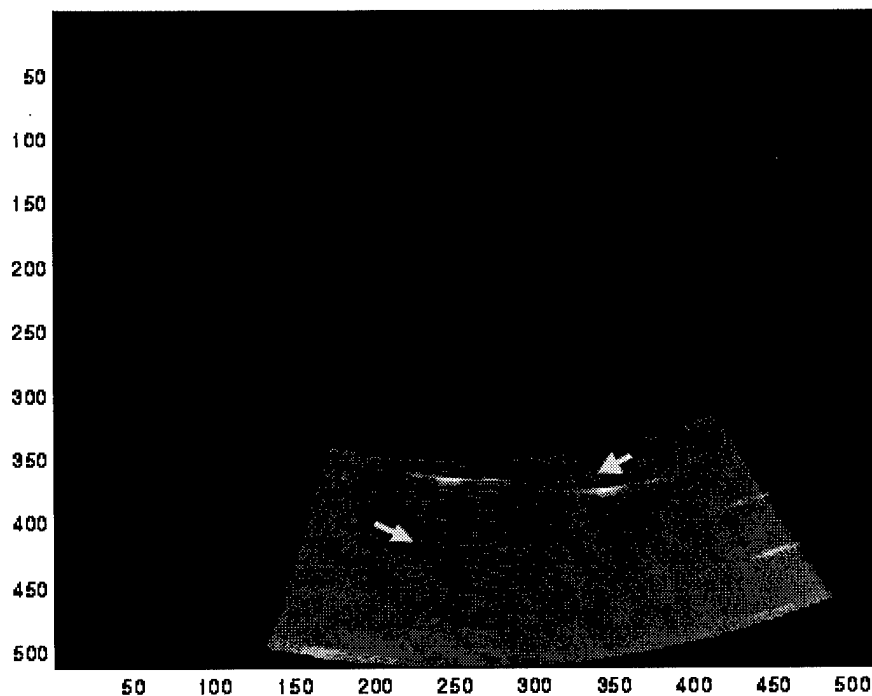


Plate 2, with phase correction

Fig.a3b. A portion of B-scan image of Plate 2 after phase deaberration. Upper arrow points to the sidelobes of the close by wire target and lower arrow points to the anechoic region. The sidelobe level has been improved but the improvement of contrast of anechoic region is marginal.
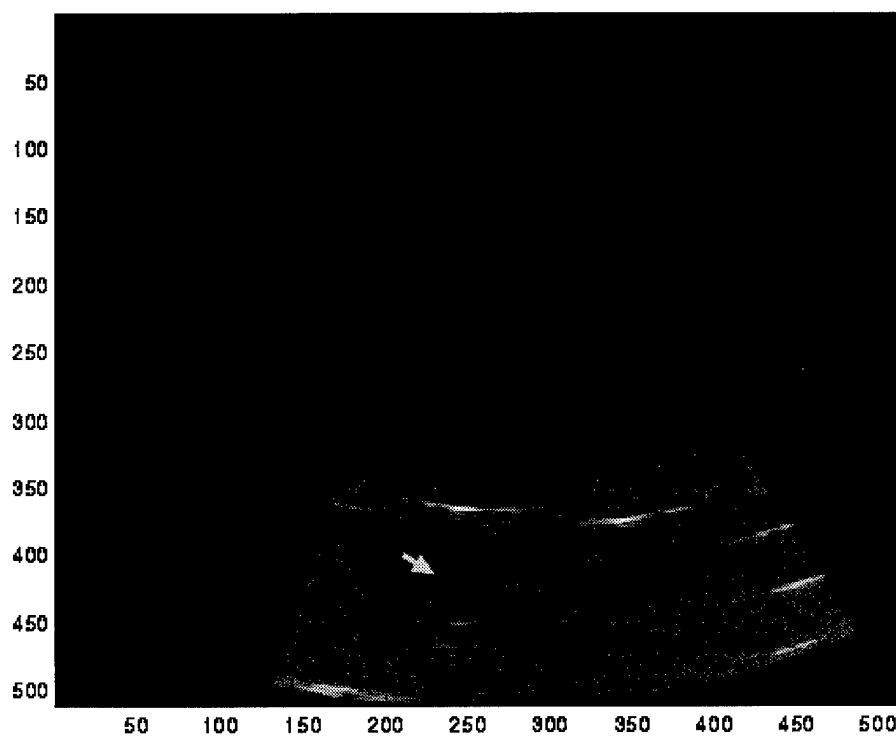
7

Plate 2, with TIF

Fig.a3b.  A portion of B-scan image of Plate 2 after TIF. The arrow points to the anechoic region.  The contrast of anechoic region is improved and the cyst beginning to show up.

# PART B. DESIGN, FABRICATION AND TESTING OF A TWO-DIMENSIONAL ULTRASONIC ARRAY

## I. INTRODUCTION

The goal is the development of two-dimensional (2-D) piezoelectric array transducers operating at 3.75 -10 MHz. The techniques are developed and refined in stages. A 2-D array of 2.5 cm x 2.5 cm size operating at 1 MHz is first built. The transducer head contains the transducer layer with ground metalization on the front side and individual electrodes on the back side. Connections to the back electrodes of all operational piezo-elements are provided through wires soldered to a PC board. A quarter wavelength impedance-matching front layer made of silver-filled epoxy is glued to the ground metalization side of the transducer layer. Design, fabrication and preliminary testing of the fabricated array are given below.

## II. DESIGN OF THE ARRAY
### A. Transducer Materials and Interconnects

A 1-3 type of piezoelectric composite consisting of PZT (lead zirconate titanate) ceramic rods in a polymer matrix serves as the material from which two dimensional addressable transducer arrays are constructed [B1]. Composites (combinations of two distinct solid phases with different connectivity patterns) can greatly enhance material utilization and properties by the synergy generated, the properties of the combination being better than the individual properties. Composites provide a much wider range of material properties than those of the standard ceramic and polymer transducers and are being actively studied in the medical ultrasonic field [B2].

In our design the individual rods with end faces individually electroded serve as transducer elements. Ideal characteristics are strong electromechanical coupling for efficient energy conversion, low acoustic impedance for good transmission into tissue, and a reasonably large dielectric constant for efficient electrical impedance matching [B3]. Further advantages of strictly periodic composite materials are control of lateral transducer resonances and reduction of crosstalk between individual electrodes in transducer arrays.

By utilizing the optimized 1-3 composite transducer design, high transmit efficiency, high receive sensitivity and broad bandwidth are achieved. Proper choice of transducer material and component dimensions optimizes electromechanical coupling and minimizes mechanical cross-talk and spurious low frequency lateral modes [B2], [B3-B6]. We note that the 1-3 composite exhibits ~30% higher thickness mode electromechanical coupling constant, $k_{3t}$, than bulk ceramic and that individual pixel $k_{3t}$ in the 1-3 composite approaches the free $k_{33}$ of an "ideal" long slender unconstrained piezo element [B2]. The monolithic bulk sample exhibits self-pinning and hence has $k_{3t} < k_{33}$.

### B. Design of Front and Back Layers

Fig.b1 is a sectional view of the array configuration along with front and back impedance-matching layers. The transducer's front surface is interfaced with a uniform $\lambda/4$ impedance-matching front layer. A patterned composite backing layer of polymer and microfabricated ceramic pillars [B7] can provide the piezoelements with the appropriate matching mechanical impedance, thus allowing its broadband operation with minimal signal degradation. The backing layer is patterned to match the active elements of the transducer. The material in the backing layer, which is between the positions of the operative piezo-elements is made of a compliant material (such as polyurethane) so as to maintain the mechanical independence of the individual ceramic elements.

The $\lambda/4$ plate, covering the front surface of the metallized transducer, can be fabricated from a composite material. Commercial impedance matching materials such as carbon and glass filled phenolic or silver-filled epoxy are available and can be machined to the appropriate thickness and glued in place. The patterned back layer can be constructed from a matching inactive array obtained from the same 1-3 composite supplier. The back layer microfabrication process will then consist of inserting conducting paths alongside the matching pillars or columns. They provide connection from the metallized electrodes to the commercial multiplexer boards.
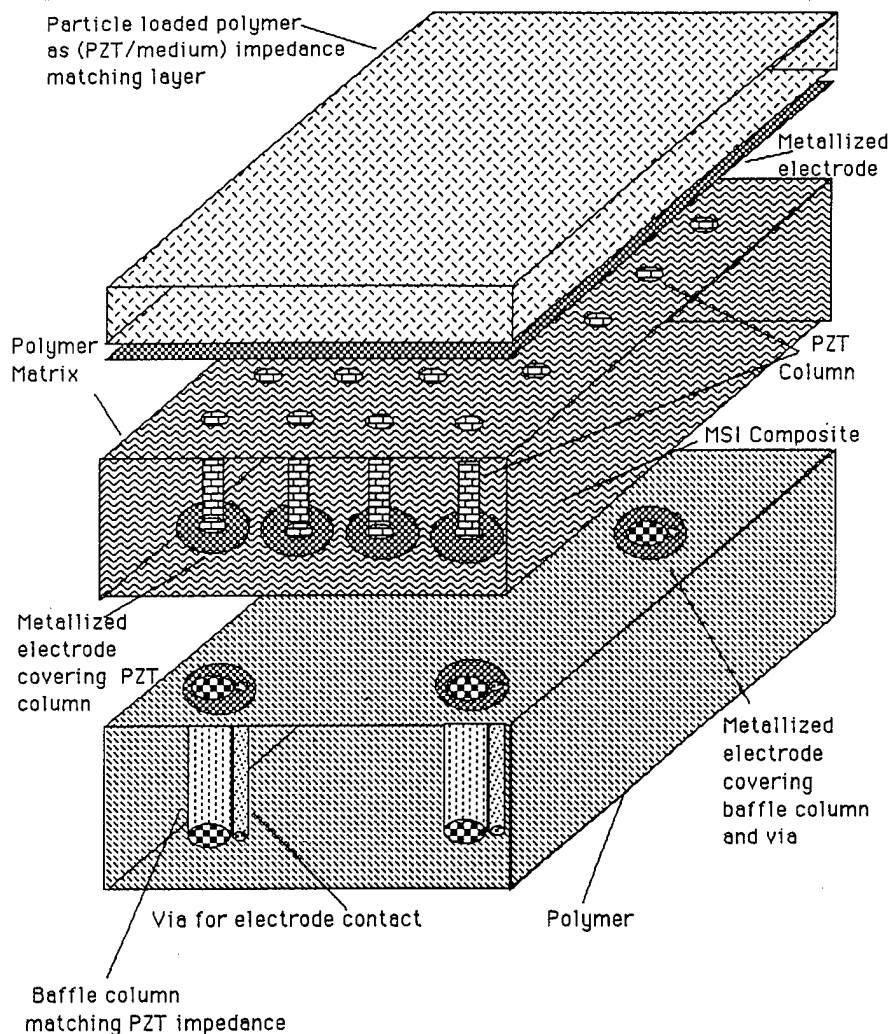
Particle loaded polymer
as (PZT/medium) impedance
matching layer

Metallized
electrode

Polymer
Matrix

PZT
Column

MSI Composite

Metallized
electrode
covering PZT
column

Metallized
electrode
covering
baffle column
and via

Via for electrode contact

Polymer

Baffle column
matching PZT impedance

Fig.b1. Sectional view of array configuration plus front and back impedance matching layers.

## III. FABRICATION OF THE ARRAY

Our fabrication of the array with a front layer and a back layer were done in a sequence of prototypes. Our first one was the array with back electrodes and ground plane metalization. The next step took this same first prototype and glued a quarter wavelength matching front layer made of silver-filled epoxy to the gold ground metalization. The final step will add a matching back layer with patterned conductive vias behind the transducer layer. Electronic and acoustic testing has been performed at each stage. A notable change in the SNR should be evident.

### A. PZT Composite Materials and Metallization

We have developed the procedures for making the final transducer array package by a series of steps. The arrays utilize PZT piezoelectric ceramic-polymer 1-3 composite materials obtained from Materials Systems, Inc.(MSI) [B1]. Our design utilizes the MSI periodic arrays of ceramic rods within a polymer matrix to construct a 2-D array with element size 0.75 $\lambda$ and element spacing 0.5 $\lambda$ (see Fig.b2). The array materials were obtained as 2.5 cm x 2.5 cm modules. Using DC Gold Sputtering metalization, carried out in our Dental School facilities [University of Pennsylvania], electrodes were applied to the entire front surface to serve as the ground plane. DC Sputtering, which occurs at room temperature, was used because the polyurethane (which holds together the piezo rod array) swells at temperatures above 100 degrees Celsius. This was deduced from our previous preliminary

array with only 12 transducers which resulted with an open circuit on the ground plane. The thin electrode of about 300 angstroms of gold was thickened through Gold Electroplating at 65 degree Celsius, so as to have at least 1000 angstroms of Gold. The non-grounded plane of the array had individual contacts on selected array elements. These contacts were manually painted silver epoxy pads which matched the silver epoxy that was used to bond the individual wires to the pads.
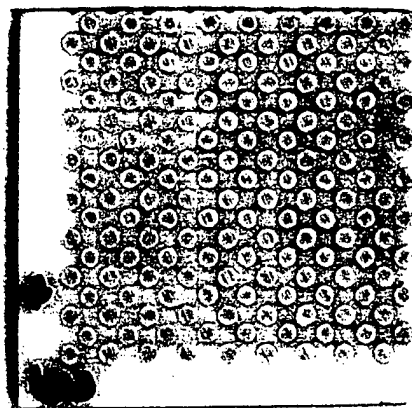


Fig. b2. 2.5 cm x 2.5 cm, 1MHz transducer module.
The module shown in the picture is enlarged by 2. The module consists of 306 elements.

## B. Bonding and Interconnections

A 7 cm by 7 cm PC board with 40 microns of copper metalization on both sides was used to provide mechanical support to the individual connections of selected array elements. From the PC board soldered wires were connected to the array of piezo rods (see Fig.b3). Since the piezo-composite fabrication process of MSI yielded a quasi-periodic element arrangement, the photolithographic process masks for the etching of the copper metalization of the PC board were obtained from digitizing actual piezo-composite array photos [B9], a technique we have used in the past. This allowed for ohmic patterns which correspond to the piezo rods. The copper pattern on the front side of the PC Board consists of .5 mm squares (which locations correspond to the piezo rods) with lines to pads (which correspond to a 54 pin socket). The design of the ohmic lines, not including the contacts for the pin socket, can be seen on Fig. b3. The side view of the copper pattern and its location on one side of the PC board can be seen on Fig. b4. The squares have 0.25 mm holes which are filled with a copper wire (0.13mm in diameter) which stick out to a length which would contact the piezo rods. The only copper pads that do not have lines are four center elements which are to be connected to individual copper wires. On the backside of the board (see Fig. b4, #5) there are: a copper pattern, spacers, and locating pins. The copper pattern, which consists of filled in circles (which was possible with the digitized picture of the piezo rods and photolithographic processes), served as additional support for the wires of center receiving elements and for wires that needed solder repair, more accurate positioning of the locating pins, and visual confirmation that the wires would accurately connect to a piezo rod. Spacers were soldered wires which provide evenly spaced pressure points needed when connecting the board to the array. Locating pins are soldered copper wires (0.8mm in diameter) into 1.1 mm holes on the PC board. The array has six matching holes corresponding to the farthest elements from the center which are not in use. (See Fig. b5 for the cross section view of array assembly.)

## C. Electronic Connections

There were 54 receiving elements which were connected to a pin socket. This allows for the manual changing of each receiving element by inserting a wire that is soldered to a coaxial cable. Future work includes a multiplexer with built in preamplifier. Four transmitting elements were chosen from the center. These had individual wires which plug into a contact to a coaxial cable.

## IV. TRANSDUCER ARRAY TESTING

11

A. Electrical Testing

Selected elements of the array were characterized throughout the design process to provide data for optimization of interfacing between the active piezoelectric elements and the first stage of electronics. These measured characteristics are important as the overall performance of the imaging system is crucially dependent on the sensitivity of the front-end design and its SNR.
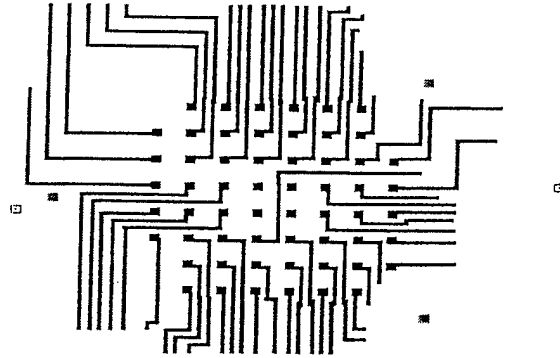


Fig.b3. The array of squares connected to lines are the receiving elements. The four center squares without lines are transmitting elements. Six of the surrounding squares without lines are locations of the position pins.
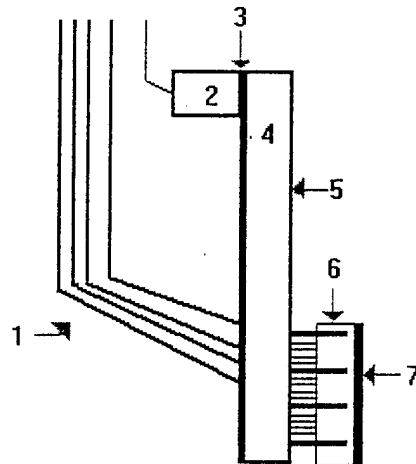


Fig.b4. The ohmic contacts for the individual elements are illustrated by the above picture and the below description. 1. four wires to transmitting transducers. 2. 54 pin socket. 3. copper pattern on the PC board. 4. PC board with wires, spacers and locating pins. 5. backside of PC board. 6. array holes for 6 locating pins. 7. ground metalization side of array.

Optimization of SNR involves knowledge of the piezoelectric element impedance and information on the possible changes in the impedance due to ohmic contacts of the piezoelectric structure using different auxiliary materials. Similar measurements should also be made for the final array prototype with selected individual elements appropriately connected.

On an Impedance Meter each of the 57 elements were tested for impedance from 0.1 to 19.6 kHz in increments of 0.5 kHz. 52 (3 transmitting and 49 receiving) elements demonstrated uniform impedance ranging

12

from 9.77 to 0.341 Mohms (see Fig.b6). One of the 57 elements served as a control for bad contacts, because it did not have a wire connecting from the PC board to the array. Four transducers had high impedance similar to the control (e.g. at 10kHz ranging from 2.2 to 13Mohms). Thus it can be deduced that the difference in impedance is due to bad contacts on the wire. Of the intended 57 total elements, 52 proved to have good contacts. The average capacitance was 23.1 pF.
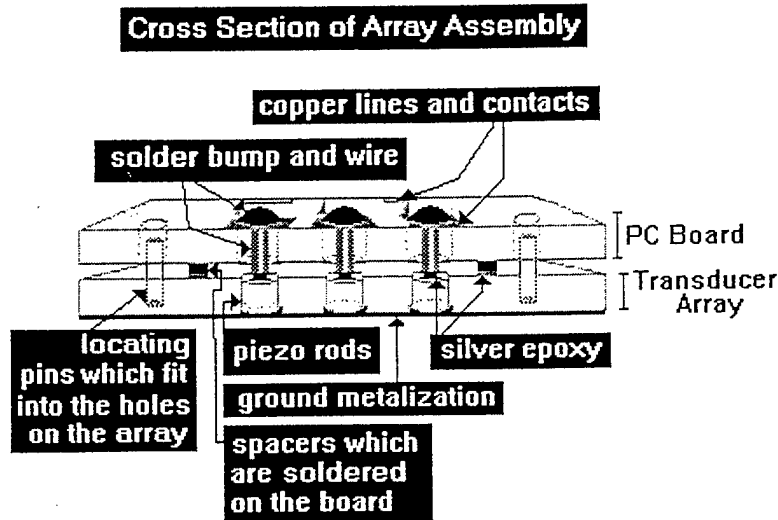


Fig.b5. The array assembly consists of a PC board with copper wires soldered to copper contacts, soldered spacers and soldered locating pins. On the top side of the PC board are copper contacts and lines that lead to a 54 pin socket. Locating pins fit into holes in the array. Copper wires are bonded to the rod metalization with silver epoxy. Spacers prevent bent wires and short circuits and bond to the array with silver epoxy for mechanical support.
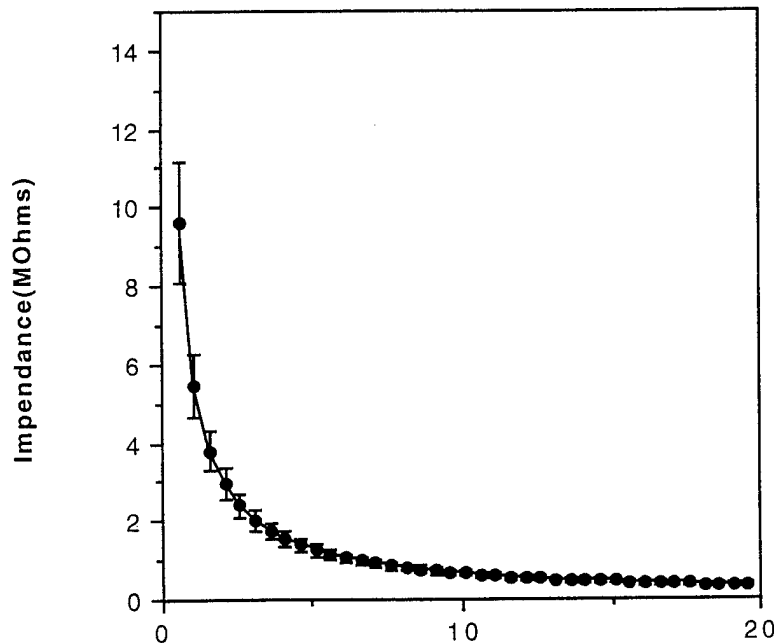


Fig.b6. The impedance ($1/ljwCl$) of 52 out of 57 elements were uniform and of the order of Mohms (<0.4Mohm for f>20kHz). The standard deviation is drawn by error bars.

13

## B. Acoustic Testing

Fig.b7 is a block diagram of our water tank testing system. The first tests were made in transmission, where each selected transducer element acts as a transmitter and a needle hydrophone (0.6 mm in diameter) as a receiver. An ultrasound pulser (Reflectoscope) generates RF pulses that drive the selected element one at a time. The received RF signals are amplified by the low noise preamp and amp inside the pulser. A digital scope (Tek 2230) samples the 16 bit RF data at 500 MHz which is well above the Nyquist frequency. The digital data are transferred to PC through a GPIB board.
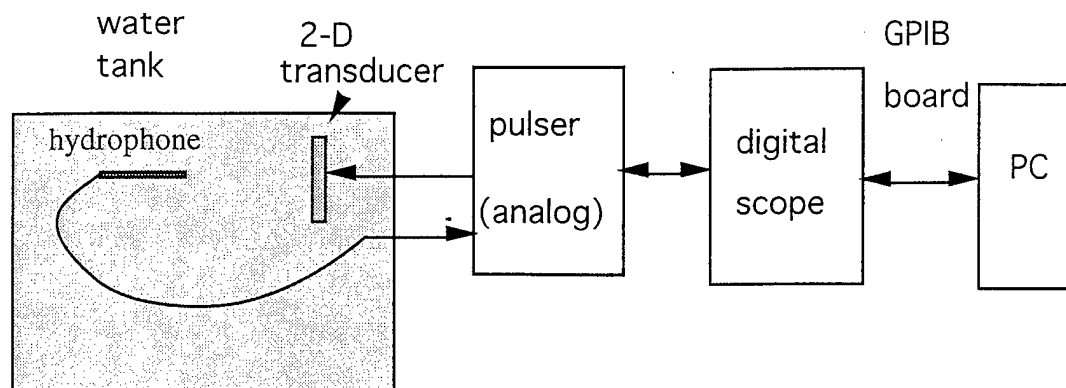


Fig.b7. Block diagram of water tank testing system.

Fig.b8 is a typical impulse response of a single element without front and back layers. The SNR is 24 dB which is very good. SNR should be further improved when the front and back layers are added to the transducer layer. As of the writing of this report, a quarter wavelength front layer has been glued to the transducer array but the contact is not good for making measurements. We need to reglue the front layer with better contact.
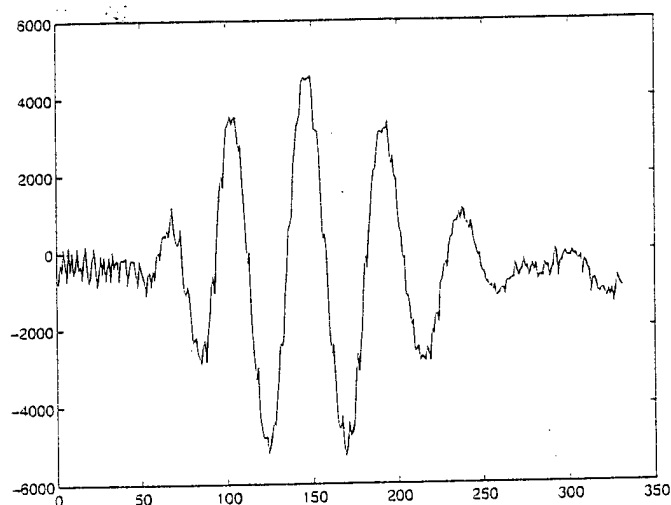


Fig.b8. Impulse response of a single element.

## V. SUMMARY

From this preliminary prototype we deduced that the patterned PC board with soldered wires worked as a good mechanical support of ohmic lines and provided accurate contact. The few that were detected to have bad contact can easily be prepared by replacing the wire and resoldering. The PC board can thus be reused with different arrays of the same make by removing the present array. Removing the present array will allow us to glue a back layer between the PC board and the array. This removal is possible because the array is held together

with silver epoxy. When force is applied, the epoxy will separate from the array. The next step involves using this same prototype at first, however, a back layer will be added to the transducer layer .

## VI. FUTURE WORK
### A. ELECTRONICS OF THE FABRICATED ARRAY

Currently, transducer testing is performed by manually selecting transmitting and receiving array elements. A high voltage multiplexer which allows electronic selection of any array elements has been purchased from Matrix Cooperation and the expected delivery date is middle October this year. With this multiplexer, we will be able to perform acoustic testing with the fabricated array described below.

### B. ACOUSTIC TESTING

The fabricated array with back layer will be fully tested acoustically. Testing parameters are the following.

Impulse response: Similar to the test discussed early.

Acoustic cross-talk: This measurement will be made by operating a selected individual element of the array in transmit mode and simultaneously monitoring the output signals at the terminals of the adjacent elements of the array operating in the receive mode.

Pulse-echo sensitivity: Pulse-echo sensitivity will be measured by the standard method of bouncing the launched acoustic pulse off a perfect reflector and monitoring the transmitted and received signals.

Single element directivity pattern: The directivity pattern of a single element will be measured in pulsed transmit mode. A needle hydrophone probe will be placed in the plane of the far field of the selected element and the lateral beam profile of the element will be measured.

Radiation pattern of entire array: The 2-way radiation pattern of the fabricated array will be measured in pulse-echo mode using synthetic aperture technique. The center transmitting elements will provide a broad transmitting beam. As a result, the measured 2-way radiation pattern is the 1-way radiation pattern of the receiving aperture. Main lobe and sidelobe characteristics can be evaluated from the measured radiation pattern.

### C. ARRAY DEVELOPMENT

After the completion of acoustic testing of the 1MHZ array, we will have complete knowledge about array fabrication procedures and pitfalls. Our next milestone is the development of a 3.75 MHz, $0.75\lambda$ array with an element size of 0.3 mm. This frequency is suitable for breast imaging.

## PARTC. COUPLING ULTRASOUND AND DIFFUSED LIGHT IMAGING METHODS
### I. INTRODUCTION

Standard ultrasound is excellent in differentiating cysts from solid lesions and is routinely used in conjunction with x-ray mammography. Ultrasound can resolve objects a few mm in size in a homogeneous medium, and its resolution in the inhomogeneous breast is steadily improving as described early. However, ultrasound sensitivity and specificity are low which may be due to the fact that even when tissues are pathologically different, their ultrasound properties are often quite similar [C1]. Near infrared (NIR) diffusive light is expected to have high sensitivity and specificity because it affords four novel biochemistry parameters (blood volume, blood O2 saturation, mitochondrial light scattering and levels of contrast agents) which differ in tumors and normal breast tissues. Three of the four parameters are easily obtainable noninvasively. The fourth requires i.v. delivery of optical contrast agents which may achieve a significant increase of specificity and afford a positive benefit/risk, particularly if the contrast agents indicate not only the extent of the tumor vascular bed and extravasation. Further, NIR may eventually indicate more fundamental biological characteristics of tumors such as mitochondrial membrane potential, intracellular calcium levels, and plasma membrane potentials, as a potential result of researches in this rapidly developing field [C2]. However, NIR diffused light suffers poor spatial resolution because of the diffuse nature of NIR light in tissue. Currently, typical reconstructions can distinguish simple structures of approximately 1 cm in size, sharp edges are typically blurred by a few millimeters [C2]. The novel combination of ultrasound and NIR light methods reported here has the potential to improve detection sensitivity and specificity of either single method. Combination took advantage of ultrasound imaging capability

15

and NIR high sensitivity/specificity potentials to increase detection sensitivity and specificity of small targets. NIR data provided a Region of Interst (ROI) for human observers to search for possible targets and lesions in ultrasound images. As a result, detection sensitivity and specificity has been improved significantly in phantom studies. Further clinical investigations are needed. If successful, this could potentially result in a low cost screening device which could assist x-ray mammography for early detection of breast cancers and reduction of the number of normal breast biopsies, and could have a highly beneficial impact on the early treatment of breast tumor.

## A. OPTICAL SPECTROSCOPY AND IMAGING

Over the last two decades, the scope and importance of research being conducted on optical methods for spectroscopy and imaging has increased dramatically [C2]. Spectroscopy is useful for the measurement of time-dependent variations in the absorption and scattering of large tissue volumes. For example, brain oxymetry (hemoglobin spectroscopy) can reveal internal bleeding caused by head injury. Imaging is critical when localization of heterogeneities inside tissues is involved, such as, an early detection of breast or brain tumors. Optical spectroscopy and imaging of body structure and function is made possible by a spectrum window that exists within tissues in the 700 - 900 nm region (near infrared), in which photon transport is dominated by scattering rather than absorption (Fig.c1). Thus, to a very good approximation, NIR photons diffuse through relatively thick tissues, such as 10-20 cm of a large human breast.

Compared with other imaging methods, the optical method has numerous advantages. NIR light is expected to have high sensitivity and specificity because certain characteristics differ in tumors and normal breast tissue: 1) The amount of blood needed to serve the tumor's metabolic needs is increased over that of normal background tissue; 2) Hemoglobin desaturation in tumors is increased due to the high oxygen demand of cancers; 3) Light scattering properties of the tumor are expected to be enhanced due to the increased mitochondria population with respect to the background of normal cells [C3]; 4) The angiogenesis phenomenon [C4] allows tumor identification by observing the delivery of contrast agents, such as the well-characterized NIR absorber indocyanine green (ICG), through the permeable vascular beds to the extravascular space surrounding the tumor. The intense absorption band of ICG at 800 nm affords a high contrast of the tumor extravascular space as compared with the background capillary network of the normal tissue. In addition, ICG has an interesting redshifted fluorescence property [C5]. It absorbs radiation at the source wavelength of 780 nm and reradiates photons at 830 nm. In this process, the tumor extravascular space is converted into a source of secondary diffuse waves with reduced background. Finally, the contrast agents could be linked to tumor-specific antibodies or to specific sites in the tumor such as their mitochondria membranes. In addition, the NIR device requires relatively low manufacturing and operating costs, NIR light is non-invasive to the human body and the device is compact and easily portable.
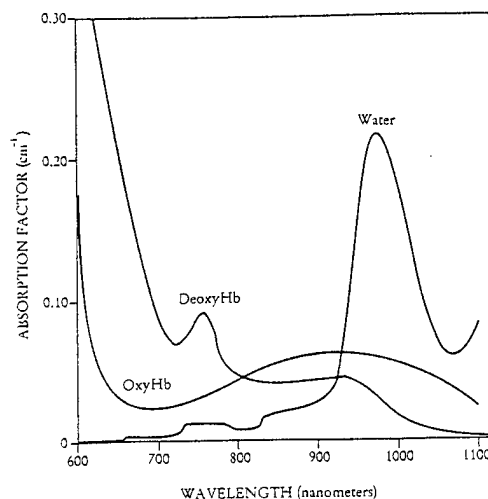


Fig.c1. *In vitro* absorption spectra of hemoglobin and water, showing a spectral window in tissue in the NIR. The window is brought about by first a decrease in blood (oxy- and deoxyhemoglobin) absorption and then an increase in water absorption with increasing wavelength (from [C2]).

16

However, there are intrinsic difficulties in obtaining images with high spatial resolution because of the diffuse nature of light propagation in human tissue. In essentially all imaging algorithms are based on computer tomographic (CT) reconstruction techniques [C8-C9,C38-C44]. Tomographic approaches require one to invert the diffusion equation or to use iterative techniques and the problem is more complicated than the x-ray CT approach because photons do not travel along straight lines. Currently, typical reconstructions can distinguish simple structures of approximately 1 cm in size; sharp edges are typically blurred by a few millimeters [C2].

## B. OPTICAL PHASED ARRAY:

A different approach to localization for NIR detection is given in [C10]. In Ref. [C10], a simple optical phased array system (OPAS) for object positioning has been constructed that measures the interference of intensity-modulated NIR diffuse light signals (in-phase, $0^O$ and out-of-phase, $180^O$) at detector positions equidistant from two spatially separated sources. In the absence of heterogeneities (Fig.c2a) the signals will cancel, and the null plane or line is always at the bisecting plane or line and the deviation between null and bisecting lines is zero. If a hidden heterogeneity is present in the medium (Fig.c2b), the balance of the sources on the bisecting line is perturbed and the null line will deviate. This deviation is used as an indicator in the scanner to detect an inhomogeneous object with respect to a homogeneous background. The line-of-sight of the heterogeneity is obtained from the newly formed null line through either mechanical or electronic scanning. This type of "pointing" device affords highly sensitive localization of a very small (~1 mm) single objects to an angular accuracy of a few degrees [C22]. *In vivo* experiments have demonstrated clear-cut amplitude nulls and sharp phase transitions [C10,C11]. Simple imaging, referred to as optical phased array imaging or null imaging in the following text, can be made by displaying spatial derivatives of the phase and/or amplitude curves obtained from scanning in one and two dimensions [C12]. A larger derivative may indicate the existence of a larger mass while a smaller derivative may indicate a smaller mass. However, exact object shape and size information and optical properties (absorption, scattering coefficients, etc.) cannot be obtained from the null imaging.
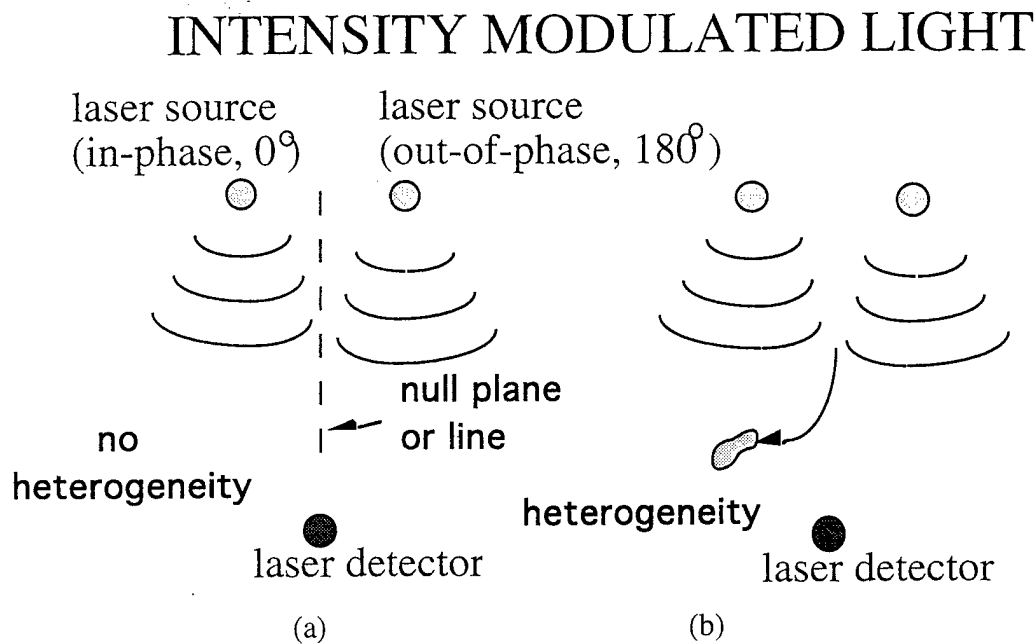
# INTENSITY MODULATED LIGHT

laser source
(in-phase, $0^O$)

laser source
(out-of-phase, $180^O$)

null plane
or line

no
heterogeneity

heterogeneity

laser detector

laser detector

(a)

(b)

Fig.c2. Illustration of object detection by optical phased array positioner.

## C. PULSE-ECHO ULTRASOUND IMAGING

The concept of pulse-echo ultrasound imaging is well known [C13]. A short burst of acoustic pulses is generated by a piezoelectrical transducer array, which is capable of converting electrical energy to acoustic energy and vice versa, and is directed into the body along any desired scan direction; echoes are generated and travel back to the transducer for detection. These echoes vary in intensity according to the type and structure of tissue. A B-scan image is formed by sweeping a narrow acoustic beam through a plane and producing display of the received echoes, such that there is a correspondence between the display scan line and the direction of acoustic propagation in the tissue. Ultrasound has many advantages; its manufacturing and operating costs are low; it is non-invasive

to the human body and it provides real-time images. The use of ultrasound to examine the breast was first described in [14]. Now, ultrasound is frequently used in conjunction with x-ray mammography to differentiate cysts from solid lesions. However, ultrasound applications with respect to early detection of small solid lesions were disappointing [C15]. Ultrasound sensitivity in the detection of palpable solid masses less than 2 cm in size was 71%, which was about 10% less than the sensitivity of physical examination [C16]. The sensitivity in the detection of small invasive lobular carcinomas (<1 cm) was only 25% [C17]. Ultrasound specificity was low due to the considerable overlap of acoustic characteristics between benign and malignant lesions [C18-C19]. More recently, the imaging capability of ultrasound equipment has been improved. For example, the results reported by Stavros et al. were very encouraging [C20]. Although no lesion size was documented in [C20], of 125 malignant lesions, 123 were correctly classified as intermediate or malignant (98.4% sensitivity).

## II. EXPERIMENTS AND RESULTS

A novel combination of the two suboptimal systems, namely ultrasound and OPAS, reported in [C21] and the Appendix C has shown a superior performance in detection sensitivity and specificity compared with ultrasound alone in phantom studies. The combination took advantage of ultrasound imaging and OPAS localization capabilities, and directed human observers to look for possible targets and lesions within a ROI in the ultrasound image. The ROI was determined from highly sensitive optical line-of-sight information. As a result, the detection sensitivity and specificity of a few mm object buried in a scattering phantom has been improved significantly. Experimental set-ups, examples and statistics are described in the following paragraphs.

In our phantom studies [C21], we incorporated the simple NIR positioner into an ultrasound imaging system (Fig.c3). An ultrasound phased array probe is coaxially mounted with the two laser diode sources, referred to as the coaxial probe in the figure, and the coaxial probe and the optical detector assembly is mechanically translated together on a rigid frame by a stepping motor. This simple combined system was tested using models consisting of a single emulated tumor of a few mm size buried in a scattering phantom. The homogeneous scattering phantom was made of an acrylamide gel (7.5 x 12 x 14 cm³), and scattering particles at optical and ultrasound wavelength scales were added to the acrylamide solution before the gel was formed. In each test, the combined system was mechanically translated to scan for the small object. In a typical experiment, 1 mm step size was used. At each scanning position, optical amplitude and phase data and an ultrasound sector scan image were acquired. The object line-of-sight information was obtained from the optical data and was coded into ultrasound images after scanning. A total of 30 targets with various acoustic and optical absorption and scattering properties were studied, and ultrasound images without and with line-of-sight information were graded on a five-point scale (see Table I) by two experienced radiologists in the Breast Imaging Section of the Radiology Department. A typical example of optical scanning and ultrasound image evaluation is demonstrated as follows.



(a)

2.0 cm    laser diode transmitters
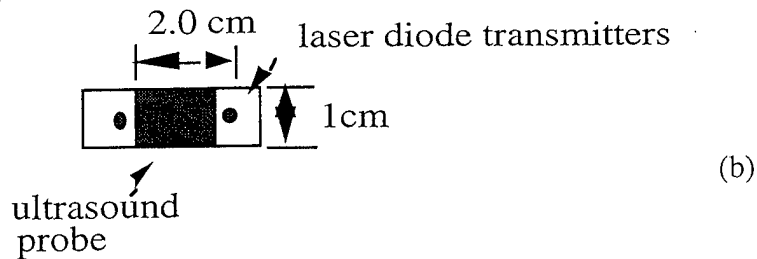
1cm

(b)
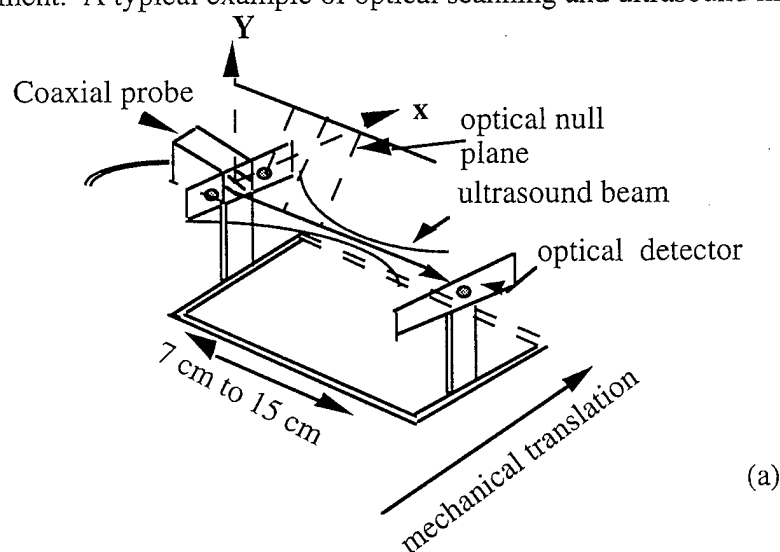
ultrasound
probe

Fig.c3. (a) Coaxial ultrasound and optical probe and optical detector assembly. (b) front view of the coaxial probe.

Fig.c4 shows optical amplitude and phase responses when concentric black-plastic tubes of 1.9 and 1.7 mm diameters filled with 0.5% intralipid (optical scattering medium) were inserted into the scattering phantom at approximately 6 cm depth. The testing object is an optical absorber which also generates an inhomogeneous ultrasound echotexture (see Fig.c5) as some tumors may do. The sharp phase transition and amplitude null correspond to the object line-of-sight. As a result of mechanical translation, a sequence of ultrasound images was obtained. Since weak targets in a sequence of images were more readily detected than in a single image, triple images taken in 1 mm steps at the neighborhood of the optical phase transition and amplitude null were selected in each test. The criteria of triple image selection are described in detail in Appendix A. Since the optical assembly and ultrasound probe are coaxially mounted, the object in the triple images always appears along the ultrasound scan axis. To avoid giving any prior knowledge to human observers about the object location, we chose different image windows in different tests to randomize the object location. In each test, the image windows used for triple images were the same and the object position shift was caused by the 1 mm lateral translation of the imaging system. In this example, three images taken at phase transition and amplitude null positions (16, 17, 18 mm) are shown in Fig.c5. The image of the object, indicated by an arrow, is highly obscured by speckle noise. Two observers evaluated the triple image using the form given in Table I. They were told that they could mentally average these images to filter out artifacts and noise. One observer picked up the target and marked category 4 on the evaluation form. When the same images coded with optical line-of-sight information, shown by dashed lines in Fig.c6, were presented to the observer, his detection confidence increased from category 4 to 5. Another observer completely missed the target in ultrasound-alone images and marked category 1 on the form. When the images with object line-of sight information were presented, the second observer picked up the target and selected category 3 on the form. This example shows the improvement in detection sensitivity when the combined method is used.

Table I.  Evaluation form

Please check for possible lesions or targets.

Target #1
    1. No lesion or target present
    2. Probably no lesion or target present
    3. Lesion or target may be present
    4. Lesion or target probably present
    5. Lesion or target definitely present

Target #2
    1. No lesion or target present
    2. Probably no lesion or target present
    3. Lesion or target may be present
    4. Lesion or target probably present
    5. Lesion or target definitely present

Target #3...
Target #4...
    Lesions, or targets may be hyperechogenic or hypoechogenic. If you identify any lesions please circle and number them on images.

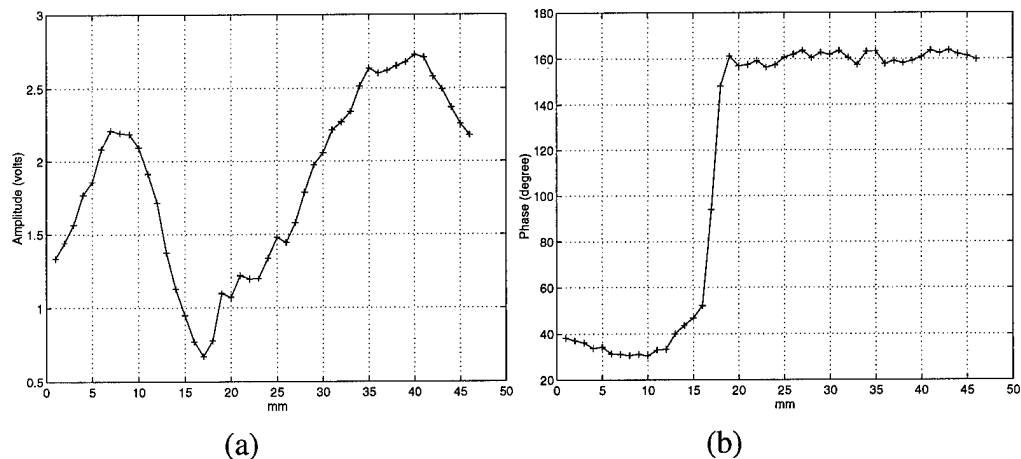(a)                                                    (b)

Fig.c4. Optical response when concentric black plastic tubes of 1.9 and 1.7 mm diameters filled with 0.5% intralipid were inserted into the scattering phantom. (a) Amplitude response and (b) phase response. The amplitude null and phase transition are indications of the object line-of-sight.
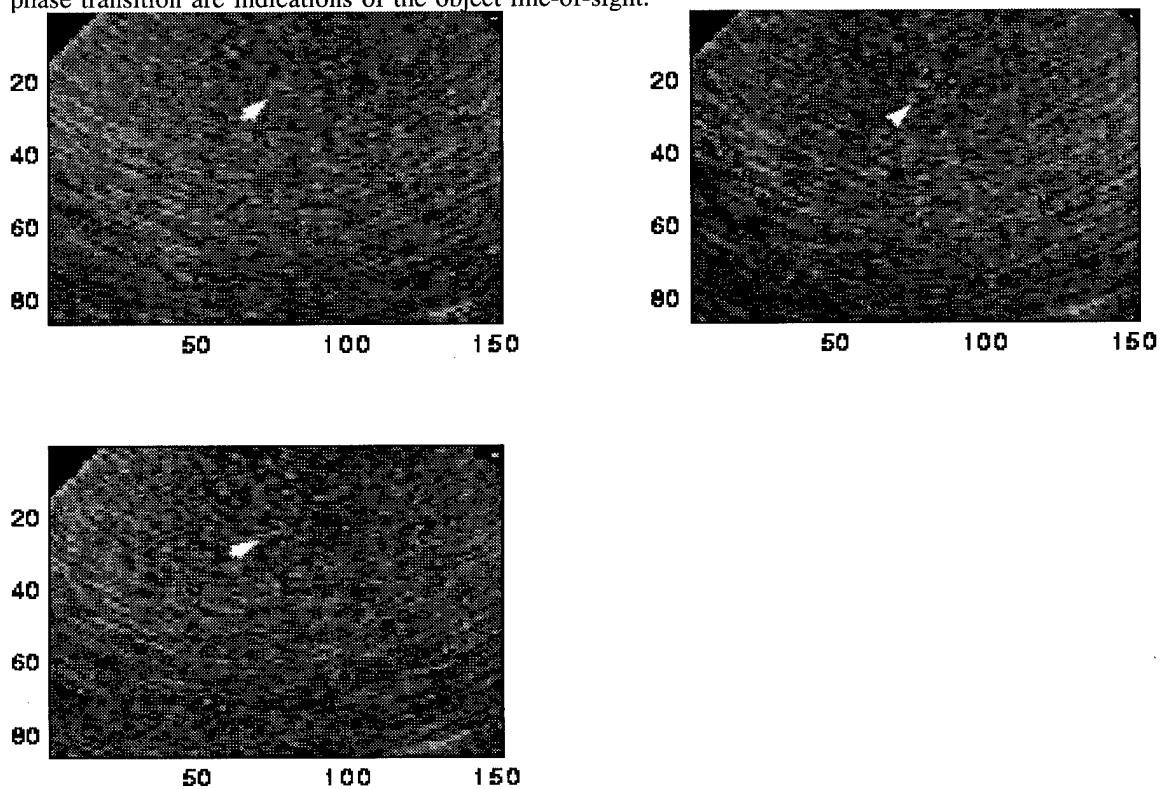


Fig.c5. The triple images taken at lateral positions 16, 17, 18 mm. Target is indicated by arrow.
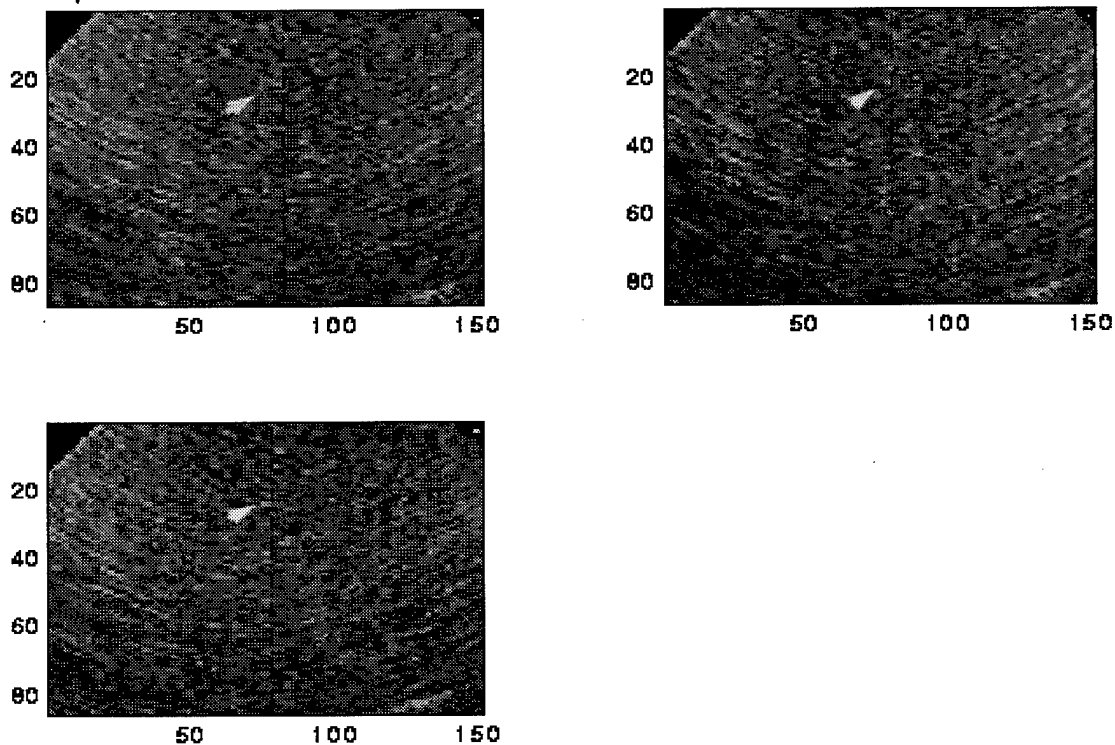
Fig.c6. The same triple images as shown in Fig.c5 but optical line-of-sight information was coded in the images as indicated by dashed lines. Target is indicated by arrow.

Figs c7-c19 show another example. Fig.c7 shows optical amplitude and phase responses when a 4.5 mm white Teflon bar was inserted into a scattering phantom at approximately 6 cm depth and was imaged using the combined system. The testing object is an optical scatterer which generates a slightly hyperechoic echotexture. The triple images taken at the neighborhood of optical phase transition and amplitude null at 1mm steps (20, 21, 22 mm) are shown in Fig.c8 with the object indicated by the upper arrow in the images. The image of the object is highly obscured by speckle noise. One observer missed the target entirely and marked category 1 on the evaluation form. When the images with object line-of-sight (Fig.c9) were presented, the observer identified the target and circled category 3 on the form. Another observer missed the target completely and selected an artifact, pointed by the lower arrow, and circled category 4 on the form. Once the images with object line-of-sight were presented, the observer identified the target and circled category 3 on the form. This example shows the combined method can significantly improve detection sensitivity and specificity of ultrasound.
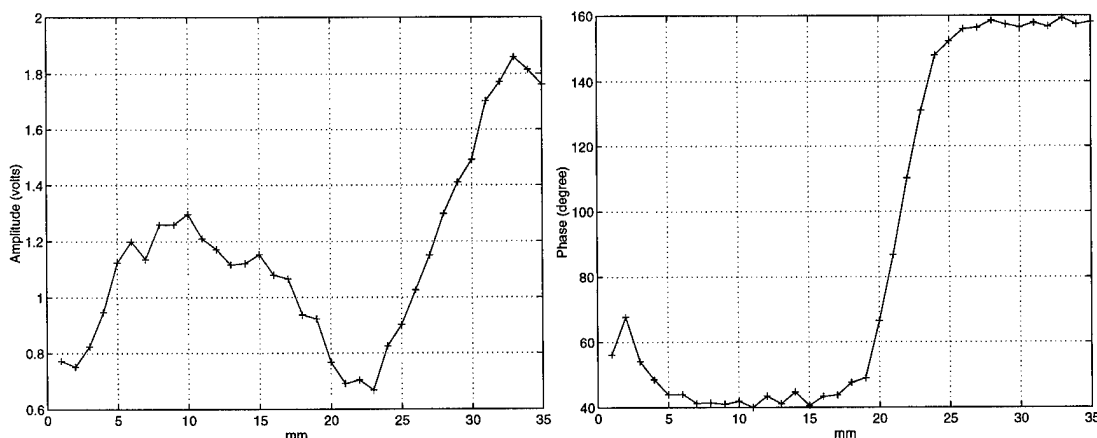


Fig.c7. Optical response when a 4.8 mm white Teflon rod was inserted into the scattering phantom. (a) Amplitude response and (b) phase response. The amplitude null and phase transition are indications of the object line-of-sight.
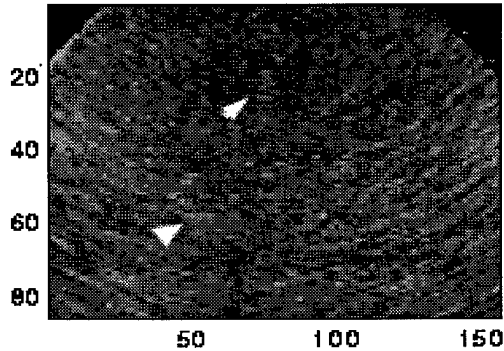
21
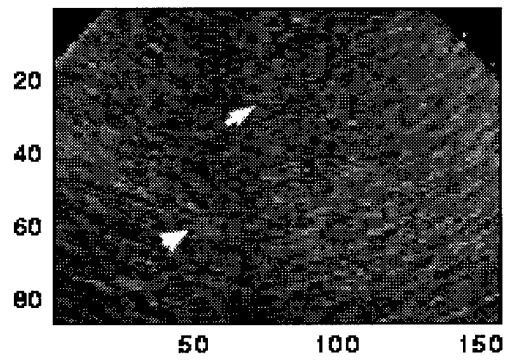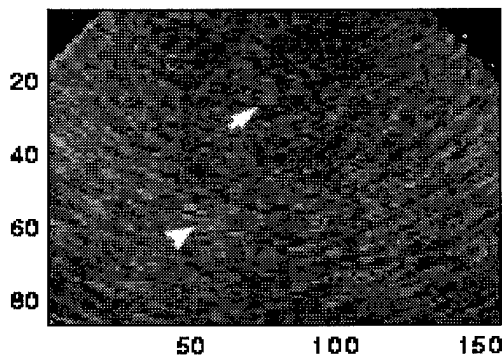
Fig.c8. The triple images taken at lateral positions 20, 21, 22 mm. Target and artifact are indicated by arrows. Object is a 4.8 mm white Teflon rod.
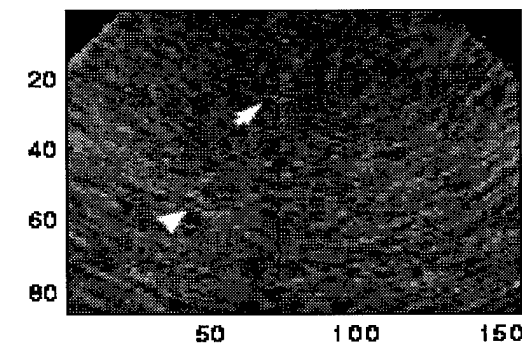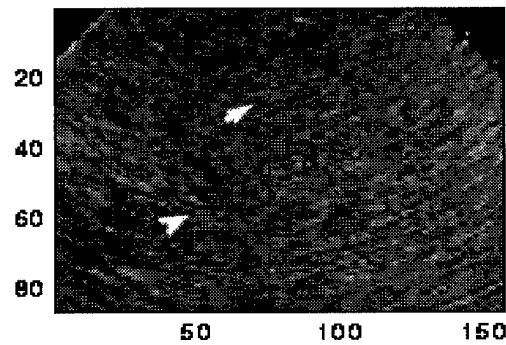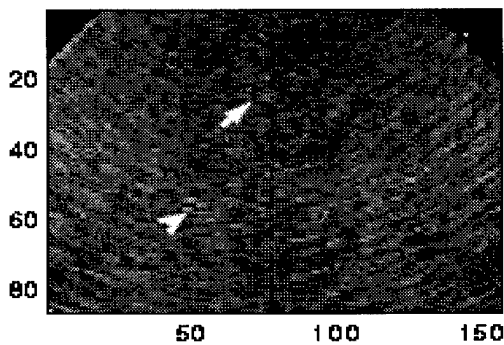


Fig.c9. The same triple images as shown in Fig.c8 but optical line-of-sight information was coded in the images as indicated by dashed lines. Target and artifact are indicated by arrows.

We have studied a total of 30 positive trials and 21 negative trials. In the positive trials, the testing objects used were optical absorbers and scatterers which emulated to a large extent tumor optical properties and generated various acoustic echo textures. The sizes of the testing objects range from 1.6 mm to 8.2 mm with an average of 3.64 mm (std. 1.97 mm). In the negative trials, images of the scattering phantom obtained at three consecutive

22

'lateral positions in 1 mm steps were presented. Receiver-Operator Characteristic (ROC) curves, commonly used to depict figures of merit for clinical methods of detecting lesions or differentiating among diseases [C22,C23], are measured from the readings of the two radiologists. Average empirical ROC curves of ultrasound (solid) and ultrasound-light (dashed) of two independent readings from the two observers are shown in Fig.c10. The superior performance of ultrasound-light is shown by the higher ROC curves. The area under the ROC curve provides a measure of discriminatory efficacy: an area of 100% denotes an ideal system and 50% denotes an ineffective system. The calculated areas under ROC curves of ultrasound and ultrasound-light of observer #1 are 53.9% and 79.2%, and of observer #2 are 49.5% and 85.8%, respectively. The mean values are 51.7% for ultrasound and 82.5% for ultrasound-light. The difference in area between the two methods is statistically significant ($p < 0.05$, see Appendix of [C21]).
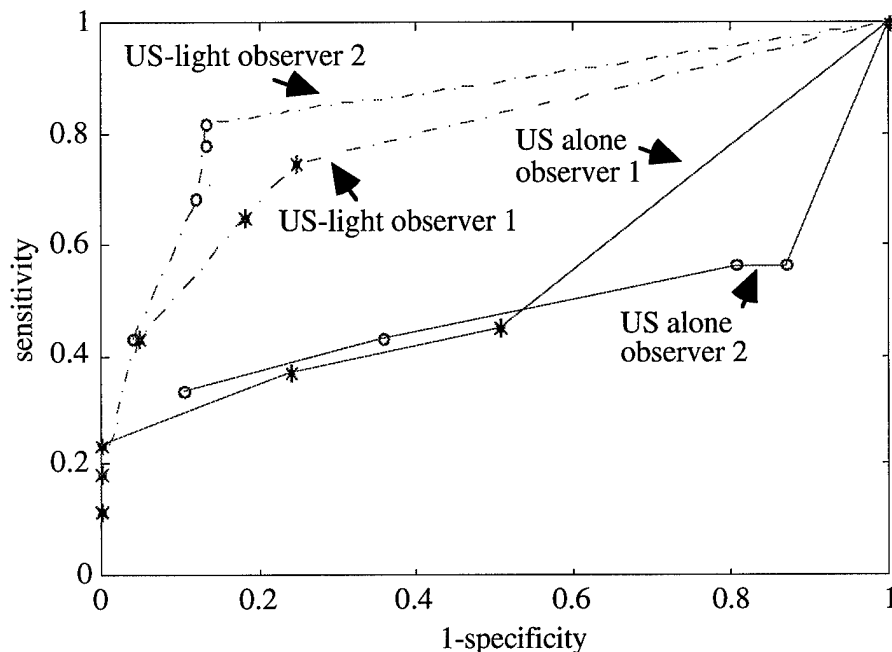


Fig.c10. Average ROC curves of two readings from two observers. The ROC curves of ultrasound method are plotted in solid lines and ROC curves of ultrasound-light are plotted in dashed lines.

III. CONCLUSION

A novel imaging method which combines ultrasound and near infrared diffuse light has been introduced in this paper. The combined method utilizes object line-of-sight information provided by a highly sensitive optical positioner to confine human observers along the object direction to search for possible lesions or targets in ultrasound images. As a result, the detection sensitivity and specificity of a small target of a few mm size have been improved significantly over the conventional ultrasound. The average areas under ROC curves from 2 radiologists are much higher for the combined method (82.5%) than for ultrasound alone (51.7%). Thus the combined method affords a significant improvement in detection sensitivity and specificity compared with conventional ultrasound. Further clinical investigations are required to evaluate this new method in breast cancer detection. Currently, we are applying funds to explore the utility of this new, exciting method through clinical trials.

**PUBLICATIONS**

**Zhu, Q.**, Chance, B, Sullivan, D, and Dambro, T. , "Coupling Ultrasound and Light Methods to Increase Detection Sensitivity and Specificity of Ultrasound," submitted to IEEE Transactions on Ultrasonic, Ferroelectrics and Frequency Control, (May, 1997).

**Zhu, Q.** Chance, B, Sullivan, D, "Optically Guided Ultrasound Imaging System for High Specificity Breast Imaging," Proc. of SPIE on Optical Tomography and Spectroscopy of Tissue: Theory, Instrumentation, Model, and Human Studies II, pp. 48-58, (1997).

Zhu, Q. and Steinberg, B.D., "Modeling and Correction of Incoherent Wavefront Distortion" Special issue of I'nal. J. Sci. Tech. Imaging, Wiley, (03) 322:335, 1997.

Zhu, Q., and Steinberg, B.D., "Deaberration of Incoherent Wavefront Distortion: An Approach Toward Inverse Filtering," IEEE Transactions on Ultrasonic, Ferroelectrics and Frequency Control, (40), No.3, 575-589, May 1997.

Zhu, Q. and Chance, B, "A Novel Optically Guided Ultrasound Imaging System," Proc. IEEE Ultrasonic Symp. 1345-1348, (Nov. 1996).

Zhu, Q. and Steinberg, B.D., "Toward Inverse Filtering Approach for Ultrasonic Wavefront Compensation," Proc. IEEE Ultrasonic Symp. 1357-1361 (Nov. 1996).

FUTURE CONFERENCE PRESENTATIONS
Zhu, Q., Chance, B, Sullivan, D, and Dambro, T. , "Combined ultrasound and NIR diffused light imaging", 1997 IEEE Ultrasonic Symp. (Toronto Cannada,Oct. 5-8, 1997).
Zhu, Q. "Ultrasonic Wavefront Distortion Compensation in Pulse-Echo Using Toward Inverse Filtering Technique," 42nd Annual Convention of American Institute of Ultrasound in Medicine, (March 1998).

## REFERENCES
[1] Moshfeghi, M. and Waag, R.C., *In Vivo* and *in Vitro* Ultrasound Beam Distortion Measurements of a Large Aperture and a Conventional Aperture Focused Transducer, *Ultrasound Med. Biol. 5,* 415-428 (1988).
[2] Trahey, G.E., Freiburger, P.D., Nock, L.F., and Sullivan, D.C.,"*In Vivo* Measurements of Ultrasonic Beam Distortion in the Breast," Ultrason. Imag. 13, 71-90 (1991).
[3] Zhu, Q. and B. D. Steinberg, "Large-Transducer Measurements of Wavefront Distortion in the Female Breast," Ultrasonic Imaging **14**: 276-299 (1992).
[4] Freiburger, P.D., Sullivan, D.C., LeBlanc, B. H., Smith, S. W., and Trahey, G.E., "Two Dimensional Ultrasonic Beam Distortion in the Breast: *In vivo* measurements and effects," Ultrason. Imag. 14(4), 398-414 (1992).
[5] Zhu, Q., Steinberg, B. D. and Arenson, R., "Wavefront Amplitude Distortion and Image Sidelobe Levels -Part II: *In Vivo* Experiments," IEEE Transactions on Ultrasonic, Ferroelectrics and Frequency Control (40) 754-761 (1993).
[6] Hinkleman, L.M., Liu, D-L., Waag, R.C., Q. Zhu and B.D.Steinberg, "Measurement and correction of ultrasonic pulse distortion produced by the human breast," JASA (97) No.3, 1958-1969 (1995).
[7] Zhu,Q. and Steinberg,B.D., "Modelling and Correction of Incoherent Wavefront Distortion," Invited paper, I'nal. J. Sci. Tech. Imaging, Wiley, Vol 8, 322-335, 1997.
[8] Phase Deaberration Section of IEEE Ultrasonic Symposium, pp:1353-1370 and pp:1391-1418, 1996.
[9] Flax, S. W. and O'Donnell, M. "Phase Aberration Correction using Signals from Point Reflectors and Diffuse Scatterers: Basic Principles," IEEE Trans. Ultrason. Ferroelec. Freq. Cont., 35(6):758-767, Nov. 1988.
[10] Nock, L., Trahey, G. E., and Smith, S.W., "Phase Aberration Correction in Medical Ultrasound Using Speckle Brightness as a Quality Factor," J. Acoust. Soc. Am., **85**(5) 1819-1833 (1989).
[11] Attia, E.H. and Steinberg,B.D. (1989), "Self-Cohering Large Antenna Arrays Using the Spatial Correlation Properties of Radar Clutter," IEEE Trans. Antennas Prop., AP-37(1), 30-38 .
[12] Ishimaru, A. (1978),*Wave Propagation and Scattering in Random Media*, Academic Press, New York.
[13] Zhu, Q., and Steinberg, B.D., "Deaberration of Incoherent Wavefront Distortion: An Approach Toward Inverse Filtering," IEEE Transactions on Ultrasonic, Ferroelectrics and Frequency Control, (40), No.3, May 1997.
[14] Liu D-L and Waag, R.C., "Correction of Ultrasonic Wavefront Distortion Using Backpropagation and Reference Waveform Method for Time-shift Compensation," J. Acoust. Soc. Am. 96, 649-660 (1994).
[15] Trahey, G.E., Freiburger, P.D., " An Evaluation of Transducer Design and Algorithm Performance for two Dimensional Phase Aberration Correction," Proc. IEEE Ultrasonic Symposium (1991).
[16] Liu and Waag, "A Comparison of Wavefront Distortion and Compensation in One-dimensional and Two-dimensional Apertures," IEEE Trans. Ultrason., Ferroelec. Freq. Contr.,Vol. 42, No.4, 726-733,1995.

[17] Zhu, Q. and Steinberg, B. D., "Modeling, Measurement and Correction of Wavefront Distortion Produced By Breast Specimens," Proc. IEEE Int'l Symp. Ultrason. Ferroelec. Freq. Cont., Cannes, Nov. 1994.

[A1] Krishnan S., Rigby K.W. and O'Donnell M.," Improved Estimation of Phase Aberration Profiles," IEEE Trans. Ultrason., Ferroelec. Freq. Contr.,Vol. 44, No.3, may,1997.
[A2] Flax, S. W. and O'Donnell, M. "Phase Aberration Correction using Signals from Point Reflectors and Diffuse Scatterers: Basic Principles," IEEE Trans. Ultrason. Ferroelec. Freq. Cont., 35(6):758-767, Nov. 1988.

[B1] Bowen, L.J., Gentilman, R.L., Pham, H.T., Fiore, D.F., and French, K.W., "Injection Molded Fine-Scale Piezoelectric Composite Transducers," IEEE Ultrasonics Sympos. Proc., 499-503 (1993).
[B2] Oakley, C.G., "Design Considerations for 1-3 Composites Used in Transducers for Medical Ultrasonic Imaging," *Proc. of the IEEE 6th Internat. Symp. on the Applic. of Ferroelectrics*, 233-236 (1991).
[B3] Auld, B.A., "High Frequency Piezoelectric Resonators," *Proc. of the IEEE 6th Internat. Symp. on the Applic. of Ferroelectrics*, 288-295 (1986).
[B4] Gururaja, T.R., Schulze, W.A., Cross, L.E., Newnham, R.E., Auld, B.A., and Wang, Y.J., "Piezoelectric Composite Materials for Ultrasonic Transducer Applications. Part I: Resonant Modes of Vibration of PZT Rod-Polymer Composites," *IEEE Transac. on Sonics and Ultras.*, SU-32, 481-498 (1985a).
[B5] Gururaja, T.R., Schulze, W.A., Cross, L.E., Newnham, R.E., "Piezoelectric Composite Materials for Ultrasonic Transducer Applications. Part II: Evaluation of Ultrasonic Medical Applications," *IEEE Transac. on Sonics and Ultras.*, SU-32, 499-513 (1985b).
[B6] Smith, S.W., Trahey, G.E., and von Ramm, O.T., "Two-dimensional arrays for medical ultrasound," Ultrasonic Imaging 14, 213-233 (1992).
[B7] Smela, Elizabeth, PhD Dissertation, University of Pennsylvania (1992).
[8] Yin, Xiaoqing, PhD Dissertation, University of Pennsylvania (1995).
[B9] Davidsen, R. E., J.A. Jensen, and S. W. Smith,"Two-Dimensional Random Arrays for Real Time Volumetric Imaging," Ultrasonic Imaging 16, 143-163, (1994).
[B10] Schlaberg, H.I.and Duffy, J.S., "Piezoelectric Polymer Composite Arrays for Ultrasonic Medical Imaging Applications," *Sensors and Actuators, A.* (1994).

[C1] Goldberg BB, Liu JB, Forsberg F: Ultrasound Contrast agents: A review. Ultrasound Med Biol 20:319, 1994.
[C2] Yodh A and Chance B,"Spectroscopy and imaging with diffusing light," Physics Today, March 1995.
[C3] Beauvoit B, Evans S, Jenkin T.W, Miller EE, Chance B,"Correlation between light scattering and the Mitochondrial Content of Normal Tissues and Transplantable Rodent Tissues," Anal. Biochem., in press. 1995.
[C4] Folkman J," Introduction: angiogensis and cancer," Cancer Biology 1992; 3:47-71.
[C5] O'Leary M. A, Boas D A, Chance B and Yodh AG,"Reradiation and Imaging of Diffuse Photon Density Waves Using Fluorescent Inhomogeneities," Journal of Luminescence, Vol. 60-61, PP.
[C6] Franceschini, M.A., Moesta, K.T., Fantini, S., Gaida, G., Gratton, E., Jess, H.,Seeber, M., Schlag, P.M.,Kashke, M.,"Frequency-domain techniques enhance optical mammography: initial clinical results, Proc. Of Nat. Ac. of Sci. (in press).
[C7] Fantini, S., Franceschini, M.A., Gaida, G., Gratton, E., Jess, H., Mantulin, W,M., Moesta, K.T., Schlag, P.M., and Kashke, M.,"Frequency-domain optical mammography: Edge effect corrections, Med. Phys. 23, 1-9 (1996).
[C8] Arridge, S. R., in Medical Optical Tomography:Functional Imaging and Monitoring, ed. G.Muller et al., SPIE Optical Engineering Press, Bellignham, WA, Vol. IS11, 31-64 (1993).
[C9] O'Leary, M. A., Boas, D. A., Chance, B. and Yodh, A. G., "Experimental Images of inhomogeneous turbid media by frequency-domain diffusing-photon tomography", Optical Letters 20, 426-428 (1995).
[C10] Chance B, Kang K, He L, Weng J, and Sevick E,"Highly sensitive object location in tissue models with linear in-phase and anti-phase multi-element optical arrays in one and two dimensions," Proc. NAtl. Acad. Sci. , vol. 90, pp. 3423-3427, April 1993, Medical Science.
[C11] Zhou SM, Xie CH, Nioko S, Liu HL and Chance B, "Phased Array Instrumentation Appropriate to High-Precision Detection and Localization of Breast Tumor," SPIE Proceeding, 1997 in press.

[C12] Hirth C, Zhou S, Xie C, Nioka S and Chance B, "Noninvasive optical imaging of localized absorption and scattering changes during functional activation of the human brain: an evaluation and feasibility study," SPIE 1997, in press.

[C13] Havlice JF and Taenzer JC,"Medical Ultrasonic Imaging: An Overview of Principles and Instrumentation," Proceedings of the IEEE, Vol. 67, No.4, April 1979.

[C14] Wild JJ and Neal D., "Use of high frequency ultrasonic waves for detecting changes of texture in living tissues,"Lancet 1951, 1:655-657.

[C15] Jackson V, "The role of US in breast imaging, Radiology 1990; 177: 305-311.

[C16] Dam PAV, Goethem MLAV, Kersschot E, Vervliet JV, et al., "Palpable Solid Breast Masses: Retrospective Single-and Multimodality Evaluation of 201 Lesions," Radiology 1988; 166:435-439.

[C17] Paramagul C, Helvie MA, Adler DD,"Invasive Lobular Carcinoma: Sonographic Appearance and Role of Sonography in Improving Diagnostic Sensitivity, Radiology 231-234, 1995.

[C18] Sickles EA, Filly RA, Callen PW, "Benign breast lesions:ultrasound detection and diagnosis, "Radiology 1984; 151:467-470.

[C19] Kopans DB, Meyer JE, Lindfors KK, "Whole-breast US imaging:four-year follow-up." Radiology 1985; 157:505-507.

[C20] Stavros TA, Thickman D, Rapp C, "Solid breast nodules: Use of sonography to distinguish between benign and malignant lesions," Radiology 1995; 196: 123-134.

[C21] Zhu Q, Chance B, Sullivan D and Dambro T,"Coupling Ultrasound and Light to Increase Detection Sensitivity and Specificity of Ultrasound," Accepted by IEEE Ultrasonic, Ferroelectrics and Frequency Control, (Sept. 1997).

[C22] Metz CE., "ROC methodology in radiologic imaging, "Invest. Radiol., vol 21, pp. 720-733.

[C23] Swets JA, "ROC analysis applied to the evaluation of medical imagery techniques," Invest. Radiol., vol. 14, pp. 109-121, 1979.

[C24] Chance B, Kang K, He L, Liu H and Zhou S,"Precision Location of Hidden Absorbers with Phased-Array Optical Systems, " Rev. Sci. Instru. 67 (12), 4324:4332, 1996.

# Modeling and Correction of Incoherent Wavefront Distortion

Qing Zhu,[1] Bernard Steinberg[2]

[1] Department of Radiology, University of Pennsylvania, Philadelphia, PA 19104

[2] Valley Forge Research Center, Moore School of Electrical Engineering, University of Pennsylvania, Philadelphia, PA 19104

**ABSTRACT:** There are two types of wavefront distortion inside the female breast: incoherent scattering and coherent interference. Adaptive wavefront compensation algorithms developed so far are useful for correction of incoherent distortion caused by scattering. The performances of these algorithms differ according to the extent of wavefront amplitude distortion. It is shown analytically and experimentally in this article that the matched filtering approach, while optimal for detection, is not so for imaging when the wavefront amplitude is distorted in addition to phasefront distortion. Matched filtering algorithms increase wavefront amplitude variance and therefore decrease image contrast. The inverse filtering approach, while ideal for fidelity, is not stable when the signal-to-noise ratio is low. An approach toward inverse filtering, amplitude compression operation in addition to phase deaberration, is introduced in this article. Analysis and experiments show that its performance is superior to matched filtering algorithms and to time-delay type correction algorithms without introducing stability problems. © 1996 John Wiley & Sons, Inc. Int J Imaging Syst Technol, 8, 322–335, 1997

**Key words:** ultrasound; wavefront compensation; inverse filtering; wavefront model

## I. INTRODUCTION

In principle, high ultrasound resolution can be achieved with very large ultrasound transducers. However, large transducers are more susceptible to wavefront distortion caused by inhomogeneous tissue, because the transducers cover large volumes of tissue and the beams interact with more spatial variations in tissue composition. The distortion inside the female breast falls into two categories: incoherent scattering reduces the target strength, broadens the image lobe [1,2], and raises the background level, and therefore lowers the image contrast [3,4]. Refraction creates coherent multipath interference that produces false targets or image artifacts in addition to true targets in the image [4,10]. The interference problem is more severe when the aperture is large.

Numerous efforts have been made to correct wavefront distor-

tion produced by breast, liver, and abdominal wall [9,13–17]. Basic deaberration algorithms [5–7] are recognized to be suitable only for weak scattering that can be modeled as a thin random-phase screen located in the plane of the receiving aperture [8–9,18]. Extensions of the basic algorithms are made to correct amplitude distortion caused by strong scattering or distributed scattering [8,9]. A model-based approach that uses a priori information of the speeds of the rectus muscle layers inside the abdominal wall has been developed to correct double image artifacts caused by refraction [17]. The proposed technique is not model based and therefore is freed from the necessity of having a priori information about the source of the distortion.

The motivation of this study stems from the following. The algorithms [5–9] that require no a priori knowledge about the propagating medium function differently upon incoherent scattering and coherent interference; therefore, it is important to understand the effects of the two distortion processes upon the image and then apply suitable correction mechanisms to the algorithms. The scattered energy increases with the propagation depth in the breast; therefore, the performance of descattering algorithms [5–9] is expected to deteriorate with depth. Modeling and quantification of depth-dependent distortion and correction are extremely valuable for the design of next-generation high-quality breast scanners.

In this article we analyze, through modeling and experiment, image distortion caused by scattering and coherent interference, and the extent to which image quality improvements are affected by deaberration. Wavefront compensation algorithms based on matched filtering are first recognized to be unsuitable for imaging in distributed scattering because the algorithms increase wavefront amplitude distortion and therefore decrease image contrast. A compression operation on wavefront amplitude, akin to inverse filtering, which can significantly reduce wavefront amplitude variance is introduced. We demonstrate through experiments that a combination of the amplitude compression and either phase deaberration at the aperture or backpropagation plus phase deaberration at some optimal distance from the aperture can significantly improve image contrast and restore the mainlobe diffraction shape to a −30-dB level. Linear regression analysis of side-lobe energy versus propagation depth from available data
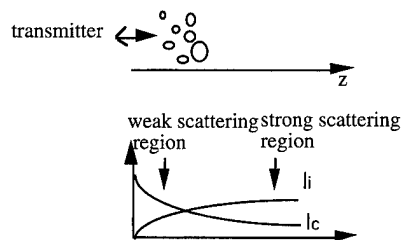
**Figure 1.** Approximate behavior of the coherent intensity $I_c$ and the incoherent intensity $I_i$.



**Figure 2.** Angular source intensity distribution. Statistical model. (a) Before phase deaberration, showing reduced coherent spectrum and of incoherent spectrum. (b) After phase deaberration.

indicates that good focusing with high-contrast resolution throughout the 100-mm propagation depth by deaberration is possible.

## II. SCATTERING MODELS

The wave propagation problem is formulated similarly to the line-of-sight propagation problem through a tenuous distribution of particles [19]. A narrowband wave is used to simplify the description and derivation. The analytic results can be taken as rules of thumb applicable to the wideband case to characterize contrast resolution due to wavefront amplitude and phase distortions.

An ultrasound wave (either spherical or planar) propagates in an inhomogeneous medium (Fig. 1). It consists of coherent and incoherent waves. The incoherent wave is also called a scattered wave. As the wave propagates, the coherent intensity $I_c$ is attenuated due to absorption and scatter, and the incoherent intensity $I_i$ is scattered broadly.

### A. Weak Scattering.
The field $E$ at a receiving aperture is predominantly coherent and the magnitude of the incoherent field is much smaller than that of the coherent field. $E$ is the sum of the coherent and incoherent fields.

$$E(x) = E_c(x) + E_i(x) \tag{1}$$

$$E_c(x) \gg E_i(x), \quad \langle E_c(x1)E_i(x2) \rangle = 0$$

$$\text{and} \quad \langle E_i(x) \rangle = 0 \tag{2}$$

where $\langle \ \rangle$ is the ensemble average and $x$ is the spatial variable at the receiving aperture.

The spatial correlation or mutual coherence function of the field at the aperture is given by $\Gamma = \langle E(x1)E(x2) \rangle$. Since $\langle E_i(x) \rangle = 0$ and $\langle E_c(x1)E_i(x2) \rangle = 0$, the spatial correlation function satisfies $\Gamma = \Gamma_c + \Gamma_i$. If the receiver is located in the far field or within the focal region of the source, the angular source intensity distribution or intensity image is the Fourier transform of the spatial correlation function and equals the summation of the coherent and statistically smoothed symmetrical incoherent spectra [Fig. 2(a)]. For each realization, however, the incoherent spectrum can have valleys and hills. The Fourier relationship between the incoherent spatial correlation function $\Gamma_i$ and incoherent spectrum is commonly known as the Van-Cittert Zernike theory [20].

The wavefront distortion is primarily in the phasefront and can be modeled approximately as due to a thin, random-phase screen located in the plane of the receiving aperture and defined
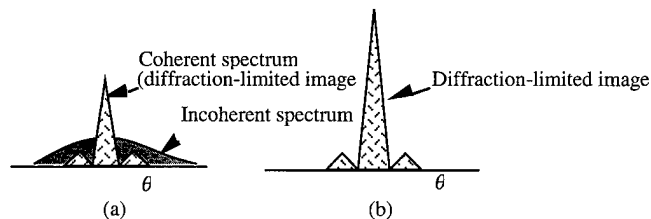
by a spatial correlation distance. Such distortion is correctable by phase-deaberration or time-delay compensation algorithms [5–7]. The algorithms operate upon the incoherent field. They fold the scattered energy into the coherent field and thereby restore the full diffraction-limited image [Fig. 2(b)].

The most relevant wavefront measurement in a weak scattering field is the spatial correlation function of the phasefront or time-delay profile as reported by several groups [1,16,21,22]. From this information, the performance of the phase-deaberration process can be predicted.

### B. Strong Scattering or Distributed Scattering.
The coherent component is attenuated and the incoherent component is scattered broadly. Wavefront amplitude is distorted in addition to phase-front distortion. A more suitable representation of the field is the Rytov model. A distributed random distortion medium can be represented as a cascade of thin, independent distortion layers [Fig. 3(a)] or phase screens [19]. At the $i$th layer, the field can be written as $E_i = A_i\exp(j\phi_i)$. Phase-front distortion is developed owing to time shift through each layer. Wavefront amplitude distortion is developed as the phase-aberrated wavefront propagates through the medium to successive layers [Fig. 3(b)]. Let $E_0 = A_0\exp(j\phi_o)$ be the reference field. The distorted field is then a product of contributions from each layer

$$E(x) = E_oE_1E_2 \cdots E_i \cdots E_N \tag{3}$$

The amplitude of $E(x)/E_0(x)$ denoted as $A_t$ is $A_t = A_1A_2 \cdots A_i \cdots A_N$ and the phase $\phi_t = \phi_1 + \phi_2 + \cdots \phi_i \cdots + \phi_N$. Assume that the layers are statistically independent and have common statistics; therefore, $A_i = \bar{A} + \delta A_i$ and
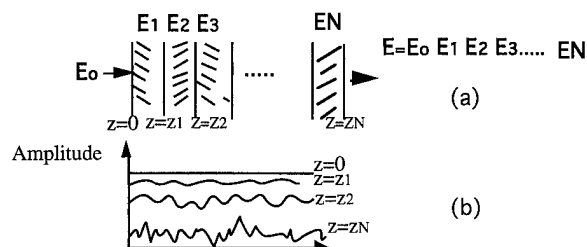


**Figure 3.** The field is the product of contributions from each layer. Wavefront amplitude fluctuation increases as wave propagates.
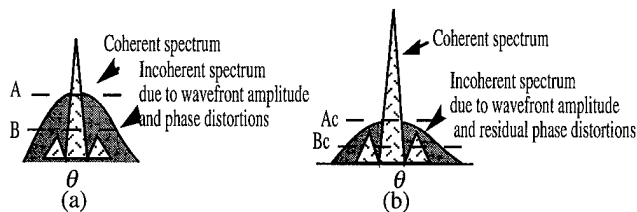
**Figure 4.** Statistical models of angular source intensity distribution. (a) Before phase correction. (b) After phase correction.

$$A_t = (\bar{A})^N \prod_{i=1}^{N} \left( 1 + \frac{\delta A_i}{\bar{A}} \right)$$

$$= (\bar{A})^N \left( 1 + \sum_{i=1}^{N} \frac{\delta A_i}{\bar{A}} + \text{higher-order products} \right) \quad (4)$$

Since $\bar{A}$ is close to unity and $\delta A_i/\bar{A}$, $i = 1, 2, \cdots N$, are independent variables, the amplitude variance of $A_t$ normalized to $(\bar{A})^N$ is $\sigma_{A_t}^2 \approx N\sigma_{\delta A/\bar{A}}^2$, where $\sigma_{\delta A/\bar{A}}^2$ is the normalized amplitude variance of a single screen. $\sigma_{A_t}^2$ grows linearly with the total number of phase screens $N$ and therefore with the propagation distance $D$. The phase variance $\sigma_{\phi_t}^2 = N\sigma_\phi^2$, where $\sigma_\phi^2$ is the variance of a single phase screen; therefore, $\sigma_{\phi_t}^2$ grows linearly with $N$ and $D$.

The overall spectrum (sum of coherent and incoherent spectra) is broadened [Fig. 4(a)] and reduced in strength. The background level is increased, and therefore image contrast is reduced.

The scattered energy increases with the propagation depth. The energy ratio (ER), which is the energy outside the main image lobe to the energy inside the main image lobe, is a useful tool to quantitatively evaluate the depth-dependence distortion upon image contrast. The relationship between ER and propagation depth $D$ (see Appendix for derivation) is

$$\text{ER} = C(\sigma_{\phi_t}^2 + \sigma_{A_t}^2) = CN(\sigma_\phi^2 + \sigma_{\delta A/\bar{A}}^2)$$

$$= C\frac{D}{d}(\sigma_\phi^2 + \sigma_{(\delta A/\bar{A})}^2) \quad (5)$$

where $C$ is a function of the source illumination profile and $d$ is the thickness of the screen and is approximately the correlation distance of the medium. ER linearly grows with the propagation distance. This relationship is analogous to the average side-lobe floor in the radiation pattern of an array with errors [23] and to the average side-lobe floor in an arbitrary source distribution imaged through a distorting medium [18]. Equation (5) can be applied to wideband as an approximation.

So long as certain correlation properties exist in the wavefront, phase compensation algorithms are still useful in strong scattering to partially remove phase distortion and build up the strength of the coherent field [Fig. 4(b)]. Wavefront amplitude distortion remains, as does residual phase distortion, and produces a significantly high incoherent background level in the spectrum. Any phase-deaberration procedure that provides a better phase error estimate than that of the basic algorithms [5–7] can reduce this background level. Wavefront-deaberration algorithms that take amplitude distortion into account can further reduce this back-

ground level if the algorithms reduce wavefront amplitude variance.

Consider the distortion vector $\mathbf{f} = E/E_o = A_t \exp(j\phi_t)$. Figure 5 shows such a distortion vector $\mathbf{f}$ for some instantaneous sample of the radiation field. The optimum compensation weight vector or transformation $w_{opt} = A_t^{-1}\exp(-j\phi_t)$ is the rightmost one which carries the distortion component of the complex sample to the intersection of the $x$-axis and the unit circle, for then both amplitude and phase are exactly corrected. The leftmost transformation $w = A_t\exp(-j\phi_t)$ is matched filtering (MF) which squares the amplitude and conjugates the phase. MF is theoretically optimum for maximizing signal-to-noise ratio (SNR) on a white, Gaussian channel. It is an optimum solution for detection but not when fidelity is an important criterion, as in imaging. But it does satisfy the requirement for phase correction. Examples of MF algorithms are dominant scatterer algorithm (DSA) [24] and time-reversal mirror (TRM) [8]. We should expect that MF algorithms are useful when wavefront distortion resides principally in phase, with amplitude relatively unaffected. Otherwise MF algorithms would be less effective than if amplitude were ignored and phase only were corrected. Later we show that by squaring the amplitude, an MF algorithm increases the wavefront amplitude variance and thereby increases the energy in the side-lobe region.

Consider what happens when a phantom consisting of a random phase screen is placed at a receiving transducer. The element signal samples are correct in amplitude and distorted only in phase by a random additive component. Phase aberration correction (PAC), consisting of phase conjugation (PC), is then the optimum compensator. The signal amplitude is unchanged. This operator is represented by the second (from the left) transformation. Time-delay compensation (TDC) [5–7] is in the same class.

The rightmost transformation which corrects both amplitude and phase is the inverse filter (IF). It is theoretically ideal for fidelity but has drawbacks. Because the IF adjusts the channel gain to be the reciprocal of the signal strength, at points in the receiving aperture where signal strength is weak the enhanced channel gain raises the noise to the point where SNR can be impaired. This is particularly troublesome when there is coherent refractive interference in the receiving array. A second potential
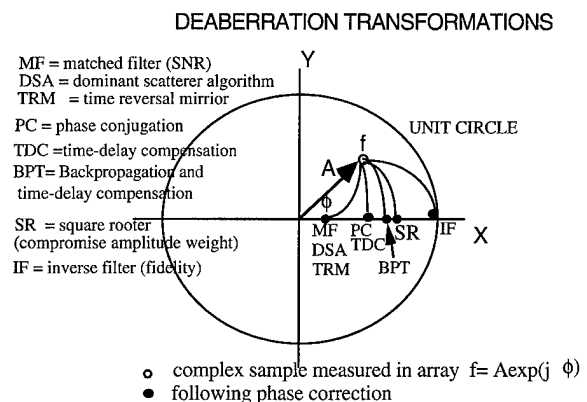


**Figure 5.** Deaberration transformations. $\mathbf{f}$ is distortion vector for instantaneous sample of the radiation field. Transformations to the real axis all correct phase. Left (MF) maximizes SNR but increases amplitude distortion. Right (IF) maximizes imaging fidelity but increases noise. SR is a good compromise.

problem, which we have avoided by not working to close to the IF point, is that an IF is unstable when the distorting medium has zeroes in the complex plane. Thus, the rightmost transformation carries the correction too far.

The complex weights of MF, PC, and IF are, respectively, $A_t$, 1, and $A_t^{-1}$, each multiplied by $\exp(-j\phi_t)$. The signal after weighting is $A_t^2$, $A_t$, and 1. The first and last are far from optimum for the reasons given. The third from the left transformation is a compromise. The correction vector is $A_t^{-1/2}\exp(-j\phi_t)$. The signal after weighting is $A_t^{1/2}$ (called later the square rooter). Another transformation to the right of the square rooter is fourth rooter (signal amplitude is $A_t^{1/4}$ after weighting). In general, the correction vector is $A_t^{-(M-1)/M}\exp(-j\phi_t)$ and signal amplitude is $A_t^{1/M}$ after transformation of the $M$th rooter. In the next section, we demonstrate experimentally that low-order rooters (square rooter and fourth rooter), in addition to phase deaberration at the aperture, can significantly improve contrast resolution without encountering the stability problem.

The DSA developed in narrowband radar [24] is designed for adaptively focusing a large distorted receiving array upon a point target and is a matched filter process in space. DSA creates a compensating weight vector $w$ from the complex conjugate of the received echo, i.e., $w = A_t\exp(-j\phi_t)$. The DSA-corrected receiving beam is the Fourier transform of $wA_t\exp(j\phi_t) = A_t^2$. Consequently, DSA uses wavefront amplitude to provide additional SNR gain than phase conjugation only, for which $w = \exp(-j\phi_t)$. However, when the wavefront amplitude is distorted, the amplitude weight further increases the side-lobe level in the beam. The measure in the increase is the increased wavefront amplitude variance. Since $A_t^2 = A_1^2 A_2^2 \cdots A_i^2 \cdots A_N^2$; therefore, Equation (4) is changed to

$$A_t^2 = (\bar{A})^{2N} \prod_{i=1}^{N} \left(1 + \frac{\delta A_i}{\bar{A}}\right)^2$$

$$= (\bar{A})^{2N}\left(1 + \sum_{i=1}^{N} 2\,\frac{\delta A_i}{\bar{A}} + \text{higher-order products}\right) \quad (6)$$

The variance of square amplitude $\sigma_{A_t^2}^2 \approx 4N\sigma_{\delta A/\bar{A}}^2$, which is four times larger than without amplitude weight. Assuming phase error $\sigma_{\phi_t}^2$ is compensated, ER will rise from $C(D/d)\sigma_{\delta A/\bar{A}}^2$ to $C(D/d)4\sigma_{\delta A/\bar{A}}^2$, which is about a 6-dB decrease in image contrast.

The TRM developed by Fink [8] provides optimal focusing of a wideband transducer upon a target through a scattering medium and is a matched filter process in both space and time (waveform). The operation reverses the received waveforms, retransmits them through the medium, and then focuses the array on the target. The transmitting beam pattern is the convolution of the received waveforms and their time-reversed version. In the frequency domain, TRM is a phase conjugation procedure (with amplitude weight) at each frequency within the signal band. It is anticipated that TRM focusing produces poorer illumination in the neighborhood of the target than does phase conjugation focusing, for the reason discussed in the previous paragraph.

Square root amplitude weighting changes Equation (4) to

$$A_t^{1/2} = (\bar{A})^{N/2} \prod_{i=1}^{N} \left(1 + \frac{\delta A_i}{\bar{A}}\right)^{1/2}$$

$$= (\bar{A})^{N/2}\left(1 + \sum_{i=1}^{N} \frac{\delta A_i}{2\bar{A}} + \text{higher-order products}\right) \quad (7)$$
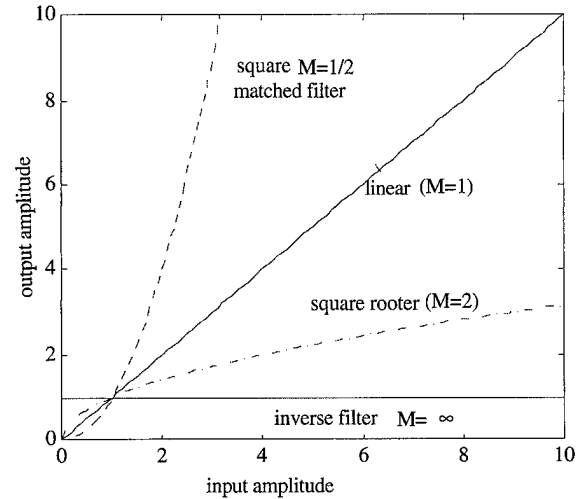


**Figure 6.** Plots of the input and output amplitude transforms.

The amplitude variance $\sigma_{A_t^{1/2}}^2 \approx N\sigma_{\delta A/\bar{A}}^2/4$, which is four times less than with unit amplitude weight. Assuming phase error is compensated. ER will reduce from $C(D/d)\sigma_{\delta A/\bar{A}}^2$ to $C(D/4d)\sigma_{\delta A/\bar{A}}^2$, which implies about a 6-dB increase in image contrast. $M$th rooter will reduce the amplitude variance by $2\,M$ if the SNR is still adequate. This nonlinear transformation upon wavefront amplitude is a compression operation (Fig. 6). The detailed evaluation of the effects of this compression operation upon image can be performed by studying the amplitude distributions of images before and after the operation. This is a subject of a later study.

Backpropagating the received wavefront to an optimal backpropagation distance and performing phase deaberration at this optimal distance (BPT) [9] provides first-order correction of wavefront amplitude distortion due to propagation from the backpropagation distance to the receiving aperture and therefore performs better than phase deaberration at the aperture. In the next section, we demonstrate experimentally that the BPT transformation is somewhere to the right of TDC and PC and left of PC and rooter. We also demonstrate that square rooter in addition to BPT can significantly improve the performance of BPT.

The relevant measurement in a strong scattering region is wavefront amplitude variance [15] (narrowband) or wavefront energy fluctuation [16,21] (wideband) in addition to arrival time variance. Since wideband waveforms can be Fourier decomposed into a set of narrowband complex wavefronts within a signal band, waveform distortion therefore implies complex wavefront amplitude distortion, and vice versa. In the following text, waveform distortion and wavefront amplitude distortion are used indistinguishably.

### C. Correction upon Scattering Samples.
To develop an understanding of deaberration, our studies have concentrated on one-way propagation measurements and corrections of point source fields. The two-dimensional (2D) measurement system and procedure were described elsewhere [11,16]. Briefly, a breast specimen was placed between hemispherical source and receiving array. The 2D array consisted of a 92-mm 1D linear array translated 46 mm perpendicular to its axis to form a synthetic 2D array 92 × 46 mm. Element pitch in the receiving transducer was
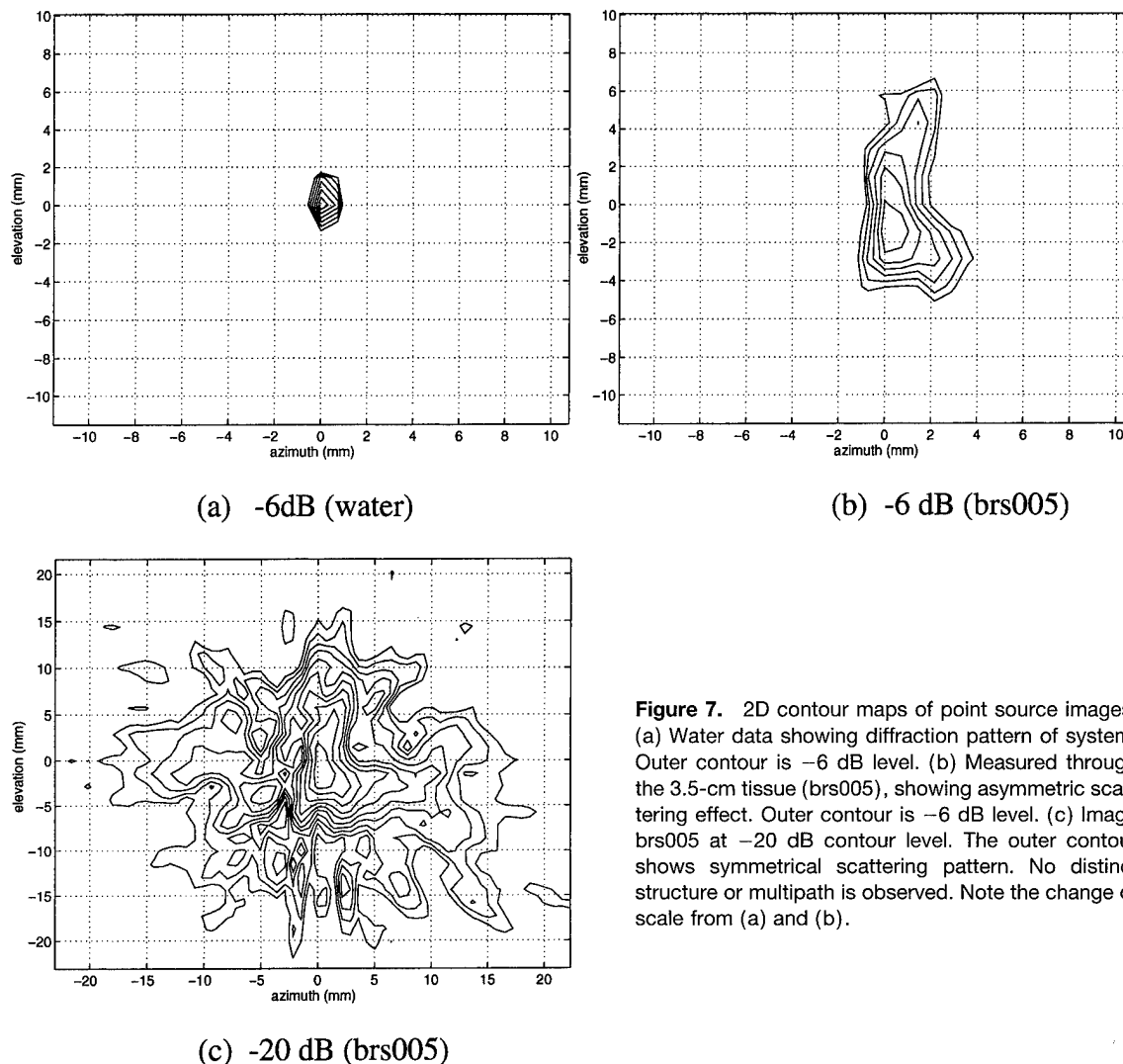
(a) -6dB (water)



(b) -6 dB (brs005)



(c) -20 dB (brs005)

**Figure 7.** 2D contour maps of point source images. (a) Water data showing diffraction pattern of system. Outer contour is −6 dB level. (b) Measured through the 3.5-cm tissue (brs005), showing asymmetric scattering effect. Outer contour is −6 dB level. (c) Image brs005 at −20 dB contour level. The outer contour shows symmetrical scattering pattern. No distinct structure or multipath is observed. Note the change of scale from (a) and (b).

0.72 mm and a reflecting mask reduced the receiving elevation to 1.44 mm. Frequency was 3.7 MHz. Bandwidth was 2 MHz. Waveforms were measured at each element, from which 2D wavefronts were reconstructed as functions of time. 3D image data were calculated by (1) Fourier decomposition of the temporal waveforms at each $(x, y)$ position in the aperture, (2) calculation of a complex CW 2D image at each Fourier frequency in the focal plane by using the angular spectrum technique [18], and (3) summation of the 2D images to form the 3D transient image. The final 2D image used in this report was obtained by detecting the peak pressure value at each $(xf, yf)$ position in the image plane within the transient period. Contour maps of 2D point source images at different thresholds were used to quantitatively evaluate image quality. The implementations of different correction methods and correction results were reported in [11]. The total measurements made were 16 with breast sample thickness varied from 1 to 4 cm. The following is a typical example of correction upon a scattering sample.

Figure 7(a) and 7(b) shows −6-dB contour plots of images obtained from the water path and the 3.5-cm breast tissue path (brs005). Contour spacing is 1 dB. Abscissa and ordinate are azimuth and elevation in millimeters in the image plane. Figure

7(a) shows the system diffraction pattern at −6 dB. The azimuthal beamwidth is about 1.5 mm (at a distance of 180 mm), meaning that the point (or lateral) resolution is 1.5/180 or 8.3 mrad. Because the size of the receiving array in elevation is half the size in the array direction, the width of the image in elevation is twice as large as in azimuth. When tissue is present (b), the image lobe is broadened. In (b) the beamwidth has grown from 1.5 to 3 mm in azimuth and 3.1 to 9.3 mm in elevation, and the point resolution has worsened approximately 2:1 in azimuth and 3:1 in elevation. A symmetrical scattering pattern appears when the threshold is reduced. Figure 7(c) shows a −20-dB contour plot of the sample image brs005. Contour spacing is 2 dB. Energy is spread out over a large area. No distinct structure or multipath lobe can be identified from the image.

Figure 8(a–g) shows the correction result of the sample image brs005 by using different methods. Part (h) is the −30-dB level contour of a water path image. The contour spacings in Figure 8 are the outer contour levels divided by 10. Figure 8(a–c) shows TDC at −6-, −20-, and −30-dB levels [see Fig. 7(b) and 7(c) for comparison]. Image quality improved significantly and the system diffraction pattern is restored up to −20-dB level. The symmetrical scattering pattern outlined by outer contours at
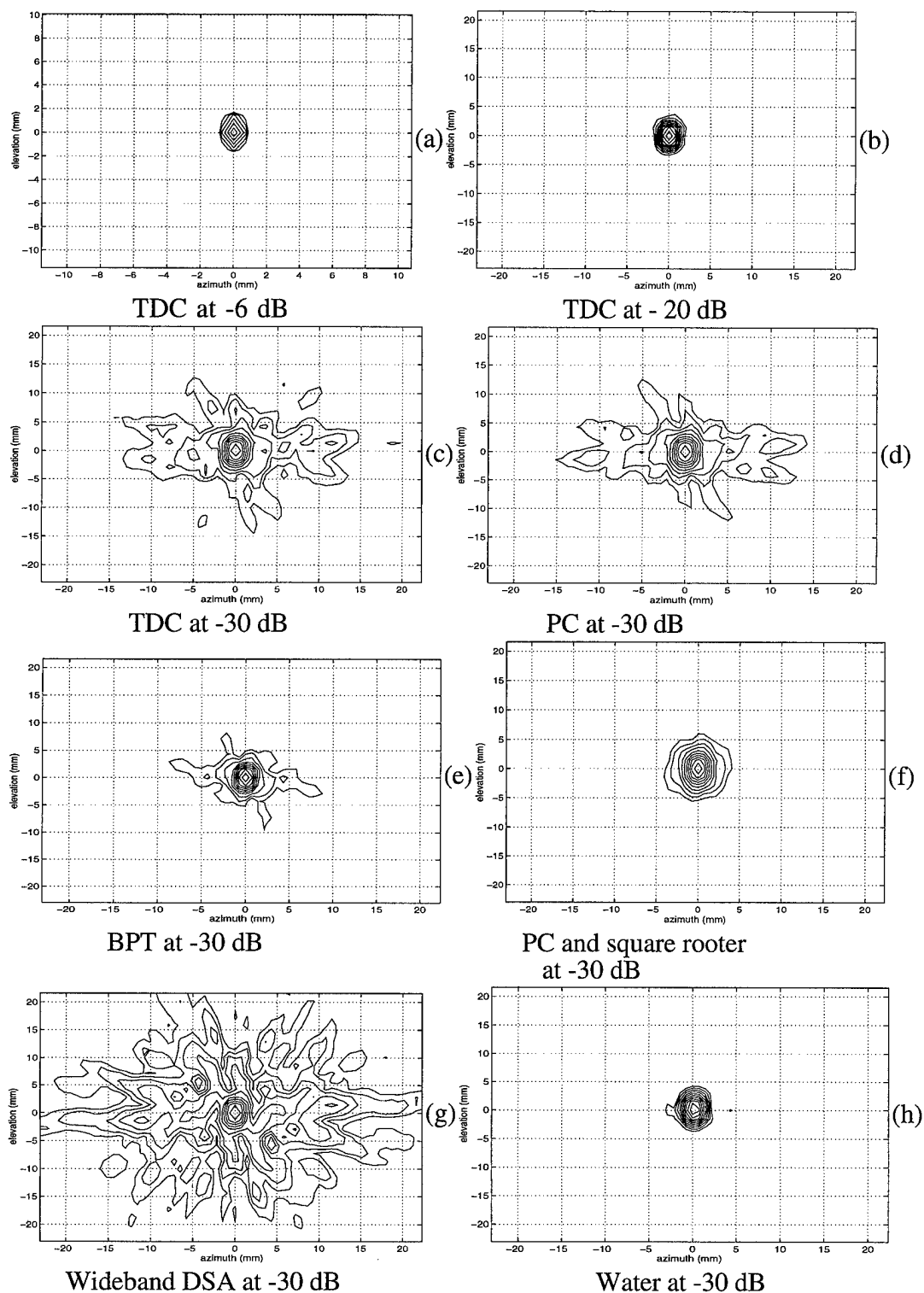
**Figure 8.** Distortion-corrected contour maps of the sample image brs005 [see Fig. 7(b) and 4(c) for comparison]. (a) TDC at −6 dB. (b) TDC at −20 dB. (c) TDC at −30 dB. (d) PC at −30 dB. (e) BPT at −30 dB. (f) PC and square rooter at −30 dB. (g) Wideband DSA at −30 dB. (h) Water at −30 dB. Note the scale change of (b−h) from (a).

the −30-dB level is caused by residual phase errors after phase deaberration and incoherent amplitude distortion. Figure 8(d) is the correction result of PC at the −30-dB level. Because of the complete removal of phase errors except for a $2\pi$ jump, the

scattering pattern is further improved as compared to Figure 8(c). Figure 8(e) is the result of BPT, and the scattering pattern is much better than that of PC at the aperture. The optimum back-propagation distance of this tissue sample is 30 mm. It is interest-

**Figure 9.** The field is the original field plus refracted fields.

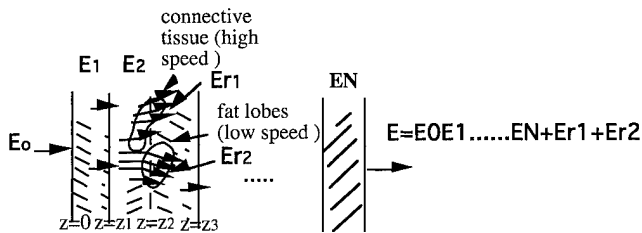ing to note that the beamwidth is narrower than that obtained through other methods. The reason is that the actual aperture is moved 30 mm closer to the source and the beamwidth is ($R$-optimal backpropagation distance) $\lambda/L$ instead of $R(\lambda/L)$, where $R$ is the distance between source and the receiving aperture, and $L$ is the aperture size. Figure 8(f) is the correction result of PC and square rooter on wavefront amplitude at $-30$ dB. The pattern is very close to the system diffraction pattern [see Fig. 8(h) for comparison]. Figure 8(g) is the result of wideband DSA at the $-30$-dB level. The correction result is worse than those of other methods.

Correction statistics of a simple metric, the lowest level at which main-lobe diffraction shape is maintained when different methods are used, are given in [11]. The average levels of using wideband DSA, PC, and PC and rooter are 14.8 (standard deviation 2.34), 19.5 (2.61), and 25.4 dB (2.55 dB), respectively. These results closely agree with the analysis in Section II of a 6-dB decrease and increase in image contrast from squaring the amplitude (DSA) to amplitude intact (PC) and amplitude intact to square root of the amplitude (PC and rooter). The average levels of using TDC and BPT are 19.3 (2.43) and 24.0 dB (1.99).

## III. SCATTERING AND REFRACTION MODEL

### A. Strong Scattering and Refraction Model.
In a refractive medium, coherent rays can be bent and split after they pass through tissue beds with different sound speeds [10]. The interference of refracted coherent ray bundles with incident rays produces image artifacts which appear as false targets. A simple representation of such a field is

$$E(x)$$

$$= E_oE_1E_2\cdots E_i\cdots E_N + E_{r1}(x)e^{[jf_1(x)]} + E_{r2}(x)e^{[jf_2(x)]} \quad (8)$$

where $f_1(x)$ and $f_2(x)$ define directions of secondary fields caused by refraction (Fig. 9).

The angular source intensity distribution is the superposition of the intensity image lobe, coherent interference lobes, and inco-

herent spectrum [Fig. 10(a)]. The strengths and the numbers of interference lobes depend on orientations, curvatures, sizes, and numbers of refractive bodies in the insonified medium, and may not be directly related to propagation depth. Although the chance of incident rays passing through more refractive bodies increases with the propagation depth, the strengths of interference lobes resulting from multiple refraction may not be significant compared with those resulting from single refraction. One quantitative measure of coherent interference phenomenon is the ratio of a large interference lobe or artifact to image lobe. For nine samples that were determined to have significant levels of coherent interference, the ratio varied randomly from sample to sample and showed no increase with thickness. The average strength (peak value) is 10 dB (standard deviation 4 dB) [11]. Another quantitative measure is the total number of large refractive lobes in each image. The average is 2 and standard deviation is 0.53. The lobe number is independent of propagation depth. The refractive lobes are tightly clustered around the main lobe with an average radius of 5.6 mm (standard deviation 1.8), which is about 2°. This is because the speed variations across glandular tissue and fat boundaries are small (5–10%).

The correction mechanism in a strong scattering and refraction medium is interesting. If the primary field is stronger than secondary refraction fields, the scattered energy removed by the deaberration process strengthens the primary field by folding the removed scattered energy into the primary field. As a result the ratio of image lobe to interference lobe is improved [Fig. 10(b)]. If, however, the primary field is weaker than the refracted field, the scattered energy removed by the deaberration process may strengthen the refracted field. The corrected result could then be worse than without correction. However, we have seen no evidence of this so far in our experiments reported in [11].

Time-reversal mirror or wideband DSA on reception is a matched filter process in both space and time, resulting in maximization of the signal relative to the background white noise. Correlation-based time-delay compensation algorithms, on the other hand, perform a different function; they adjust time delay to maximize image sharpness or image contrast. In a refractive medium, the problem is more complicated. Neither TRM or wideband DSA nor time-delay algorithms have a way of knowing which signal is real and which is an artifact caused by coherent multipath. Because TRM or wideband DSA is a spatial matched filter, its weight vector forms a lobular radiation pattern that matches the sum of both the real and false signals. Hence all targets, whether real or false, are enhanced. In our experiments reported in [11], with nine samples that have well-defined multipath artifacts, we found an average 5 dB (standard deviation 2.5) increase in peak artifact to image lobe ratio by using wideband DSA rather than by using time-delay compensation.
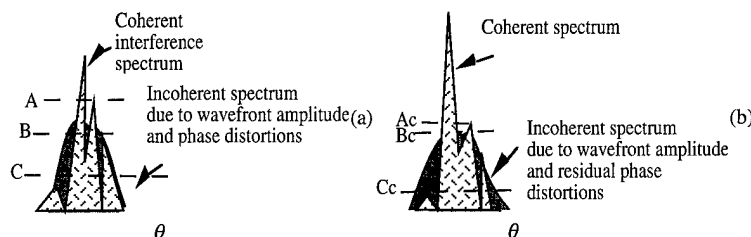


**Figure 10.** Before (a) and after (b) phase compensation.

BPT backpropagates waveforms to the optimum distance before applying time-delay compensation. It removes wavefront amplitude distortion caused by propagation and reduces residual phase distortion by improving the performance of time-delay correction, but will not remove large lobes caused by refraction. A simple thought experiment is convincing: Backpropagating two plane waves produces two plane waves at whatever distance the waves are backpropagated.

Thus, it is important to understand the deaberration operations and to design appropriate algorithms that offer optimal performance in the corresponding distorting medium. Aperture measurement alone cannot distinguish between wavefront distortions caused by refraction or by strong scattering. Distinction can be made in the image domain where refraction appears as large, coherent interference lobes while strong scattering spreads into an incoherent background. While the refracted energy may or may not be significantly larger than the energy in the incident wave, it nevertheless produces image artifacts which will destroy the quality of a high resolution image.

## B. Correction upon Samples with Well-Defined Multipath.

In most breast samples (nine of 16), scattering and coherent interference are both present. Figure 11(a) and 11(b) is −10-dB contour plots of images obtained from the water path and the 4-cm breast tissue path (brs006). Contour spacing is 2 dB. In tissue image (b), three lobes instead of one central image lobe appear. Inner contours of the image lobe are close to the system diffraction pattern [Fig. 11(a)], while the outer contours are highly irregular owing to scattering. The point resolution is worsened by approximately 2:1 in azimuth and 3:1 in elevation. Two refractive lobes appear at (−4, −2.5) and (3.5, 1.5), and their strengths are −6 and −8 dB. A closer examination is obtained from 45° cuts (Fig. 12) of the Figure 11(a) and 11(b) images. In Figure 12(a), the peak sidelobe is −36 dB, which is the best we can obtain from the measurement system. In the tissue image, two large side lobes (−6 and −8 dB) appear on either side of the main lobe. The two nulls between the lobes are deep (left: −13 dB below peak, right: −15 dB), which is a typical coherent interference phenomenon [10].

A symmetrical scattering pattern generally appears when the threshold is reduced, as shown in Figure 11(c) with a −16-dB threshold contour and contour spacings of approximately 1.5 dB. The outer contours show a roughly symmetrical pattern typical of scattering, while the inner contours show an asymmetric lobular interference pattern.

Figure 13 shows correction results of the sample image brs006 after applying different methods. The contour spacings are the outer contour levels divided by 10. Figure 13(a) is the −16-dB contour map of applying TDC [see Fig. 11(c) for comparison]. Image quality improved significantly because of the minimization of the phase-front distortion caused by scattering. The area within the −16-dB inner contour is reduced by a factor of 11. The mainlobe pattern is close to the system diffraction pattern, although the area is still 1.6 times larger than the area in water at the same level. Two large lobes remain as expected and appear as two additional sources. Figure 13(h) is the correction result at a −16-dB level of applying wideband DSA. It is evident that the procedure enhances interference in this example; the artifacts are 5 dB higher than in Figure 13(a). Figure 13(b) and 13(c) shows −25- and −30-dB contour plots of TDC. In Figure 13(b) the outer contours show an asymmetric interference pattern with

scattered energy distributed around the two interference lobes. In Figure 13(c) the outer contours show the more symmetrical scattering pattern caused by incoherent wavefront amplitude distortion and residual phase distortion. Figure 13(d) is the result of PC at −30 dB. The approximately symmetrical scattering pattern outlined by outer contours in Figure 13(c) is improved because of better phase deaberration. The energy is more concentrated around the image lobe and interference lobes. Part (e) is the result of BPT, and the scattering pattern is further improved as compared with the result of PC at the aperture. The backpropagation distance of this sample is 50 mm. Part (f) is the result of PC and square rooter at −30 dB. The pattern is very close to the system diffraction pattern. PC and fourth rooter shown in Figure 13(g) restores the diffraction-limited image to a −30-dB level.

It is interesting to note that the strengths of the two interference lobes are also reduced by 8 dB after TDC and PC. They are further reduced by 5, 7, and 15 dB after BPT, PC and square rooter, and PC and fourth rooter, respectively. The improvement comes from the scattered energy which is originally distributed around the main lobe and each of the refracted multipath lobes. This energy is coherently added back, by the deaberration process, to the dominant lobe, which in this case is the main lobe. The overall result is an improvement of the image lobe to the interference lobe ratio.

Determination of whether interference was coherent or scattered was based on whether large lobes could be removed by applying phase-deaberration algorithms. Another indicator is whether a lobe location moves (scattering) or remains relatively the same (refraction) after the phase deaberration process. Both means were used to identify whether these lobes were produced by refraction or scattering. Large lobes in nine samples are believed to be caused by the interference process. In these samples, we have found an average of a 10-dB (standard deviation 4) improvement in the range of 5–16 dB after TDC, owing to the coherent strengthening of the mainlobe.

## IV. EXPERIMENTS

The significance of appropriate amplitude weighting discussed in Section II is experimentally evaluated using ER introduced in Equation (5). When phase error is removed, ER is proportional to $\sigma_{A_t}^2$. The detailed measurement procedures of ER and $\sigma_{A_t}^2$ are reported in [11]. Figure 14 shows regression plots of ER, measured after reducing the phase error using PC, wideband DSA, and PC and square rooter, versus $\sigma_{A_t}^2$. The three methods compensate phase errors. ER and $\sigma_{A_t}^2$ measured in water using the three correction procedures are also incorporated into the three data sets to represent the system performance. The linear relationships are statistically significant. The average ERs are 103% (standard deviation 33.9%), 25% (6.9%) and 6.8% (1.6%) when wideband DSA, PC, and PC and rooter are used, respectively. An approximate factor of 4 reduction in ER from amplitude squaring (wideband DSA) to amplitude intact (PC) and amplitude intact to square root of amplitude (PC and rooter) is obtained. The results agree with the analysis in Section II and indicate that intelligent use of amplitude weighting is crucial for improving image contrast.

Scattered energy increases with the propagation depth as predicted by Equation (5) and performances of descattering algorithms deteriorate with propagation depth. In [11], regression plots of ER versus approximate thickness of 16 breast
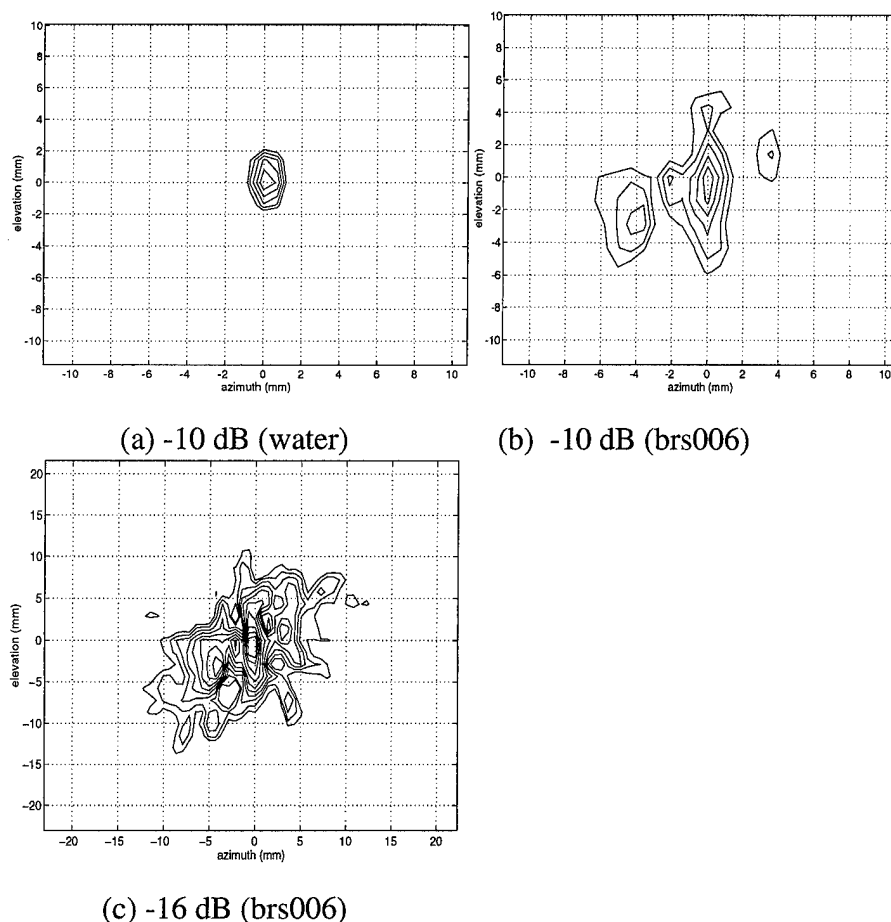
(a) -10 dB (water)

(b) -10 dB (brs006)

(c) -16 dB (brs006)

**Figure 11.** 2D contour maps of point source images. (a) water data showing diffraction pattern of system. Outer contour is −10 dB level. (b) measured through the 4-cm tissue (brs006), showing highly asymmetric interference pattern. Outer contour is −10 dB level. (c) Image brs006 at −16 dB contour level. The outer contour shows more symmetrical scattering pattern. Note the change of scale from (a) and (b).

samples were given by using seven descattering procedures. The regression plot without correction was also given. The linear relationships were statistically significant. Figure 15 shows partial results taken from [11]. The five curves in the figure are obtained by using wideband DSA (circle), TDC (solid square), PC (triangle), PC and rooter (solid triangle), and no correction (solid circle). ER reduction from amplitude weighting (wideband DSA) to square root of amplitude weighting (PC and rooter) is clearly shown by the regression plots. The regression lines are extrapolated to 100-mm propa-
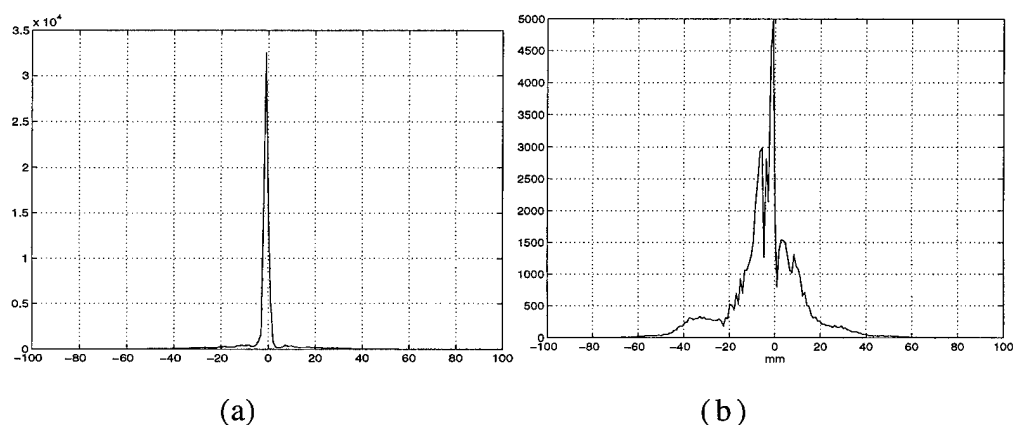


(a)

(b)

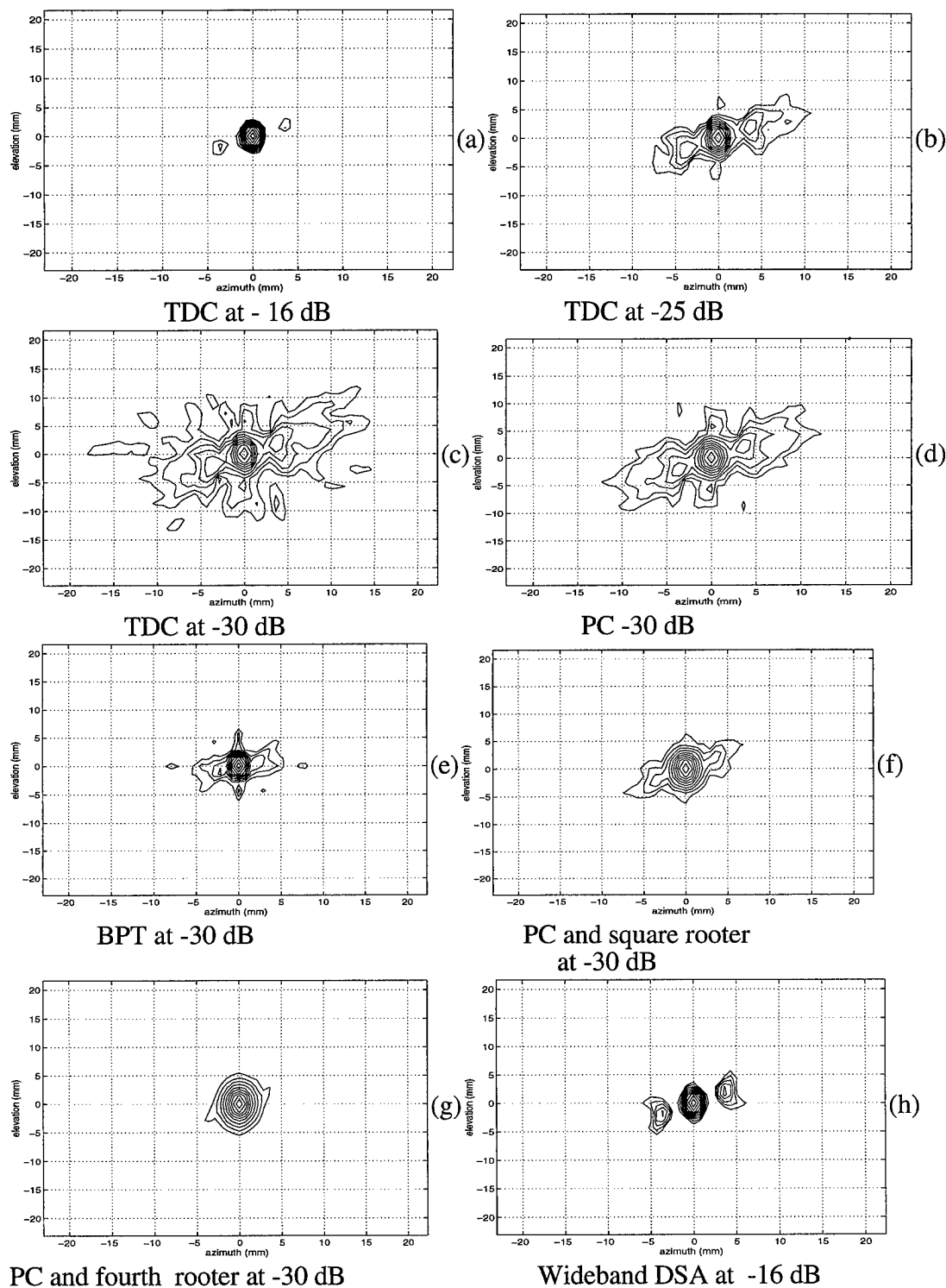**Figure 12.** (a) 45° cuts of 2D images: (a) water, (b) brs006.

**Figure 13.** Distortion corrected contour maps of the sample image brs006 [see Fig. 11(b) and 11(c) for comparison]. (a) TDC at −16 dB level. (b) TDC at −25 dB level and (c) TDC at −30 dB level. (d) PC at −30 dB level. (e) BPT at −30 dB. (f) PC and square rooter at −30 dB. (g) PC and fourth rooter at −30 dB. (h) Wideband DSA at −16 dB. Artifacts are 5 dB higher than time-delayed correction shown in Figure 13(a).

gation depth, which is considered the average maximum penetration depth required for breast.

Before we discuss the predicted performance of the descattering algorithms at 100-mm depth, we need to find the relationship between ER and image contrast, which is defined as the lowest level of the main-lobe diffraction shape. Image contrast increases monotonically with ER. Table I lists the measured average ER (first row) and the measured average image contrast (second row)
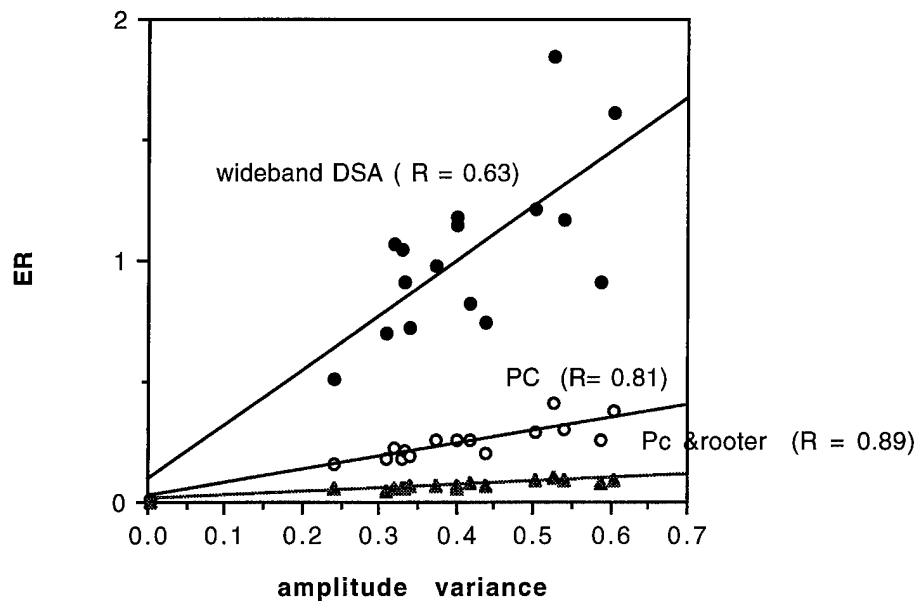
**Figure 14.** Linear regression plots of ER, after wideband DSA (upper), phase conjugation (middle) and phase conjugation and square rooter (bottom), versus wavefront amplitude variance.

when different correction methods as well as no correction are used [11]. The relationship between ER and image contrast can be predicted by using ER and image contrast obtained from PC (or any correction method) as baseline (bold numbers in Table I). For example, the measured image contrast with PC is 19.5 dB. The ER ratio of PC alone to PC and rooter is 25.1 1/6.8 = 3.7, corresponding to an increase of 5.7 dB. Thus, the predicted image

contrast is 19.5 + 5.7 = 25.2 dB, which closely agrees with the measured value 25.4 dB. The third row in Table I lists the predicted image contrast based on the measured ER. The predicted values are in reasonably good agreement with the measured values except for the pair without correction. The reason is due to ER measurement error in images without correction. For some severely distorted images, it is often difficult to identify the mainlobe region.
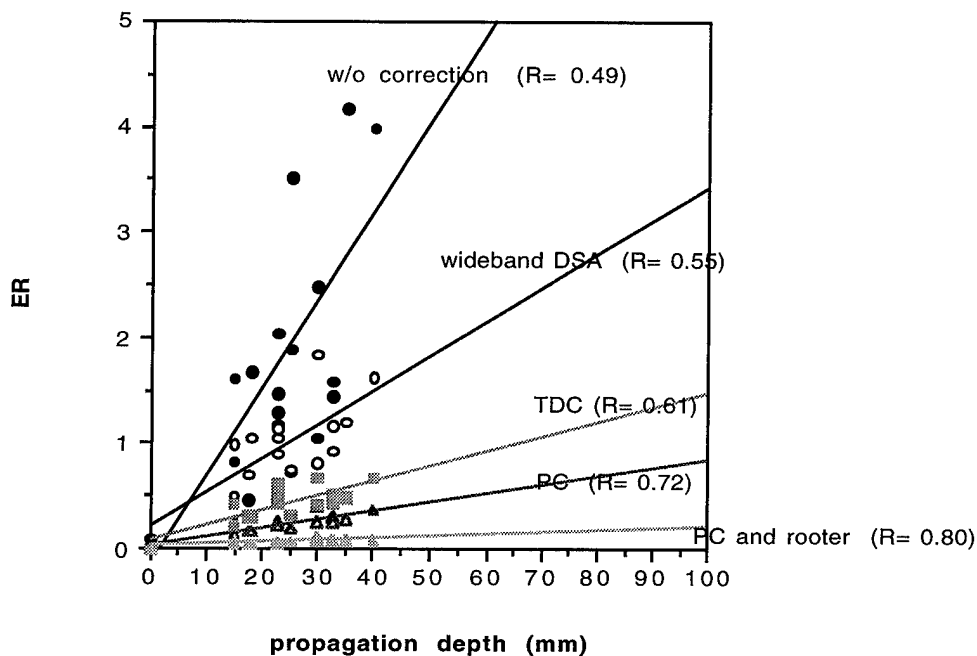
**Figure 15.** Linear regression plots of ER versus propagation depth obtained from without correction (solid circle), wideband DSA (circle), TDC (solid square), PC (triangle), and PC and rooter (solid triangle). The correlation coefficients are given by R. One outlier was removed from (a).

**Table I.** Relation of ER and image contrast (predicted and measured).

| | Without Corr. | TDC | PC | Wideband DSA | BPT | PC & Square Rooter | BPT & Square Rooter | PC & Fourth Rooter |
|---|---|---|---|---|---|---|---|---|
| ER | 214.7% | 44.2% | **25.1%** | 103.5% | 12.8% | 6.8% | 3.7% | 2.1% |
| Image contrast | | | | | | | | |
| Measured | 4.2 (dB) | 19 | **19.5** | 14.8 | 24.0 | 25.4 | 29.4 | 31.1 |
| Predicted | 10.2 (dB) | 17 | **19.5** | 13.3 | 22.4 | 25.2 | 27.8 | 30.3 |

At 100-mm depth, ER after PC reaches 85% which corresponds to 14.0 dB image contrast. Therefore, PC, the best linear phase correction procedure at the aperture, is likely to result in only ~ 14 dB image contrast at this depth. ER after wideband DSA reaches 324.3%, which corresponds to only ~ 8.4 dB image contrast. ER after PC and rooter reaches 22%, which provides ~ 20.1 dB image contrast. ER after TDC reaches 148%, which offers only ~ 11.8 dB image contrast.

The data used to test the analysis developed in Section II are sparse; nevertheless, they provide information for designers of next-generation high-quality breast scanners.

## V. DISCUSSION

### A. Application to Diffuse Scattering Medium.
The compression operation upon wavefront amplitude, in addition to phase deaberration or BPT, introduced here is applicable to a diffuse scattering medium. Experiments with TDC and rooter and TDC alone show that ER can be reduced from 44.2% to 28.6%, the ratio of which indicates 1.3 dB improvement in image contrast. However, experiments with PC and rooter and PC alone show that ER can be reduced from 25.1% to 6.8%, which is about 6 dB improvement in image contrast. The large difference is due to the fact that PC corrects phase in every signal spectrum, while TDC makes a single correction which applies to all frequencies. The consequence is that TDC leaves significant phase residual. Therefore, to successfully improve image contrast, good phase deaberration is the first crucial step to reduce ER, followed by amplitude compression such as rooter.

### B. Application to Coherent Interference upon Pulsed-Echo Imaging.
High-resolution, high–dynamic range breast imaging implies seeing a black cyst 60 dB weaker than a bright speckled target. In this article, we show that 30 dB image contrast on reception is obtainable by taking low-order rooters provided that phase error is completed compensated. In pulsed echo, refracted energy from the targets insonified by the subbeam will arrive at angles of 1–3° from the target direction [11] and therefore in the side-lobe region of array. The side-lobe level of the receiving beam will be ~ −30 dB. The average level of refracted multipath is found to be −10 dB relative to the target image [11], and therefore the average multipath signal level entering the system is ~ (10 + 30) dB = −40 dB below the echo strength of the illuminated target. Cancelation algorithms [12] must suppress these multipath signals to achieve 60 dB contrast resolution. Hence, about 20 dB further cancelation is required.

## VI. CONCLUSIONS

We conclude, through analysis and experiment, that (1) matched filtering compensation algorithms while optimal for detection are not suitable for imaging in distributed scattering, because the algorithms increase wavefront amplitude variance and therefore decrease image contrast; and (2) low-order rooters upon wavefront amplitude, akin to inverse filtering, in addition to phase deaberration can significantly improve image contrast without encounter stability problem. Further study is needed to optimize the required degree of compression as a function of SNR and image contrast.

Incoherent scattering and coherent multipath affect an image differently. Scattering reduces target strength, broadens the image lobe, and increases background level, while refraction creates coherent multipath interference which produces false targets or image artifacts. Adaptive compensation algorithms developed so far are useful to partially remove the scattered energy and coherently add it back to the coherent image. The result is the improvement of both lateral and contrast resolution to a large extent. The ratio of image lobe to artifacts is also improved because of the strengthening of the coherent filed by descattering processes.

## APPENDIX

Let $s(u)$ represent the complex angular source distribution, where $u = \sin(\theta)$ and $\theta$ is the angle from the array normal. Its complex radiation field in the axis of the receiving array in a homogeneous medium is the inverse Fresnel transform of $s(u)$ or inverse Fourier transform of $s(u)$ after correcting for near-field curvature and is denoted as $E_o(x)$. In an inhomogeneous medium, the radiation field is $i(x) = \alpha W(x)E_o(x)M(x)$, where $w(x)$ is the aperture weighting function, $M(x) = A_t \exp(j\phi_t)$ is the medium-induced distortion, and $\alpha$ is a constant to reflect any signal loss. The complex image is

$$\hat{s}_i(u) = \alpha F[W(x)E_o(x)M(x)]$$

$$= \alpha f(u) * s(u) * F(M(x)) \quad \text{(A1)}$$

where $F(M(x)) = \mu(u)$ is the angular impulse response of the medium. $F$ denotes Fourier transform. The subscript $i$ denotes inhomogeneous medium. For $\alpha = 1$ and $M(x) = 1$, the complex

image corresponds to the image in homogeneous medium and is denoted as $\hat{s}_h(u)$.

The derivation is made with discrete rather than continuous variables. Thus, $x$ is replaced by $n = 1, 2, \cdots N$, where $N =$ number of elements in the array. The following assumptions are made:

1. Medium-induced amplitude and phase errors are uncorrelated.
2. The phase errors of $\phi_t(n), n = 1, 2, \cdots N$, are statistically uncorrelated random variables with a common probability density function (pdf).
3. The amplitude errors of $A_t(n), n = 1, 2, \cdots N$, are statistically uncorrelated random variables with a common pdf.

The complex image $s_i(u)$ can be written as

$$\hat{s}_i = \alpha F[E_o(n)A_t(n)] = \alpha \sum_{n=1}^{N} E_o(n)A_t(n)\exp(jkndu) \quad (A2)$$

where the aperture taper $W(n)$ has been chosen as unity.

The image intensity is the product of Equation (A2) and its complex conjugate:

$$\hat{s}_i(u)\hat{s}_i^*(u) = \alpha^2 \sum_{n=1}^{N} \sum_{m=1}^{N} E_o(n)E_o^*(m)A_t(n)A_t(m)\exp(j(\phi_t(n)$$
$$- \phi_t(m)))\exp(jk(n - m)du)$$
$$= \alpha^2 \left\{ \sum_{n=m}^{N} E_o(n)E_o^*(n)A_t^2(n) \right.$$
$$+ \sum_{n \neq m}^{N} E_o(n)E_o^*(m)A_t(n)A_t(m)\exp(j(\phi_t(n)$$
$$\left. - \phi_t(m)))\exp(jk(n - m)du) \right\} \quad (A3)$$

The average intensity is

$$\overline{\hat{s}_i(u)\hat{s}_i^*(u)} = \alpha^2 \left\{ \sum_{n=m}^{N} E_o(n)E_o^*(n)\overline{A_t^2(n)} + \sum_{n \neq m}^{N} E_o(n)E_o^*(m) \right.$$
$$\times \overline{A_t(n)A_t(m)\exp(j(\phi_t(n))\exp(-j\phi_t(m))}$$
$$\left. \times \exp(jk(n - m)du) \right\}$$
$$= \alpha^2 \left\{ \sum_{n=m}^{N} E_o(n)E_o^*(n)(\sigma_{A_t}^2 \right.$$
$$+ (\overline{A_t})^2) + \sum_{n \neq m}^{N} E_o(n)E_o^*(m)$$
$$\left. (\overline{A_t})^2\overline{\exp(j\phi_t)}^2\exp(jk(n - m)du) \right\} \quad (A4)$$

where

$$\overline{A_t(n)A_t(m)} = \overline{A_t(n)}\,\overline{A_t(m)} = \overline{A_t}^2$$

and

$$\overline{\exp(j\phi_t(n))\exp(-j\phi_t(m))} = \overline{\exp(j\phi_t(n))}\,\overline{\exp(-j\phi_t(m))}$$
$$= \overline{\exp(j\phi_t)}^2$$

because of assumptions (2) and (3), respectively.

$$\overline{\hat{s}_i(u)\hat{s}_i^*(u)} = \alpha^2 \left\{ \sum_{n=m}^{N} E_o(n)E_o^*(n)(\sigma_{A_t}^2) + \sum_{n=m}^{N} E_o(n)E_o^*(n) \right.$$
$$\times (1 - \overline{\exp(j(\phi_t)}^2)(\overline{A_t})^2 + \overline{A_t}^2\overline{\exp(j(\phi_t)}^2 \sum_{n=1}^{N} \sum_{m=1}^{N} E_o(n)E_o^*$$
$$\left. \times (m)\exp(jk(n - m)du) \right\} \quad (A5)$$

The term $\overline{A_t}^2\overline{\exp(j(\phi_t)}^2 \sum_{n=m}^{N} E_o(n)E_o^*(n)$ is added to the second term of (A4), resulting in the third term of (A5). The same term is subtracted from (A4), resulting in the second term of (A5).

$$\overline{\hat{s}_i(u)\hat{s}_i^*(u)} = \alpha^2 \left\{ \sum_{n=m}^{N} E_o(n)E_o^*(n)(\sigma_{A_t}^2) + \sum_{n=m}^{N} E_o(n)E_o^*(n) \right.$$
$$\left. \times (1 - \overline{\exp(j(\phi_t)}^2)(\overline{A_t})^2 + (\overline{A_t})^2\overline{\exp(j(\phi_t)}^2\hat{s}_h(u)\hat{s}_h^*(u) \right\} \quad (A6)$$

Integration with respect to $u$ on both side of Equation (A6) yields

$$\int_{main\ lobe} \overline{\hat{s}_i(u)\hat{s}_i^*(u)}\ du + \int_{side\ lobe} \overline{\hat{s}_i(u)\hat{s}_i^*(u)}\ du$$
$$= \alpha^2 \left\{ \int_{main\ lobe} \left[ \sum_{n=m}^{N} E_o(n)E_o^*(n)(\sigma_{A_t}^2) + \sum_{n=m}^{N} E_o(n)E_o^*(n) \right. \right.$$
$$\left. \times (1 - \overline{\exp(j(\phi_t)}^2)(\overline{A_t})^2 \right] du + \int_{main\ lobe} (\overline{A_t})^2\overline{\exp(j(\phi_t)}^2\hat{s}_h$$
$$\times (u)\hat{s}_h^*(u)\ du + \alpha^2 \left\{ \int_{side\ lobe} \left[ \sum_{n=m}^{N} E_o(n)E_o^*(n)(\sigma_{A_t}^2) \right. \right.$$
$$+ \sum_{n=m}^{N} E_o(n)E_o^*(n)(1 - \overline{\exp(j(\phi_t)}^2)(\overline{A_t})^2 \right] du$$
$$+ \int_{side\ lobe} (\overline{A_t})^2\overline{\exp(j(\phi_t)}^2\hat{s}_h(u)\hat{s}_h^*(u)\ du \right\} \quad (A7)$$

$$ER \overset{\Delta}{=} \frac{Energy - outside\ main\ lobe}{Energy - inside\ main\ lobe}$$

$$= \frac{\int_{side\ lobe} \Sigma_{n=m}^{N} E_o(n)E_o^*(n)\ du\}}{\{\sigma_{A_t}^2 + (1 - \overline{\exp(j(\phi_t)}^2)\overline{A_t}^2\}}{\int_{main\ lobe} (\overline{A_t})^2\overline{\exp(j(\phi_t))}^2\hat{s}_h(u)\hat{s}_h^*(u)\ du} \quad (A8)$$

where $\int_{side\ lobe} (\overline{A_t})^2\overline{\exp(j(\phi_t)}^2\hat{s}_h(u)\hat{s}_h^*(u)\ du$ is small compared with the rest of the side-lobe terms and is dropped from the numerator and $\int_{main\ lobe} [\Sigma_{n=m}^{N} E_o(n)E_o^*(n)(\sigma_{A_t}^2) + \Sigma_{n=m}^{N}$

$E_o(h)E_o^*(n)(1 - \overline{\exp(j(\phi_t)^2)}(\overline{A_t})^2]\ du$ is small compared with another main-lobe term and is dropped from the denominator. Since $\overline{A_t}$ is close to unity and $\overline{\exp(j(\phi_t)}$ is also close to unity when the phase error is moderate, the right side of Equation (A8) is $C\{\sigma_{A_t}^2 + (1 - \overline{\exp(j(\phi_t)^2)})\}$, where

$$C = \frac{\int_{side\ lobe} \Sigma_{n=m}^N E_o(n)E_o^*(n)\ du}{\int_{main\ lobe} \hat{S}_h(u)\hat{S}_h^*(u)\ du}$$

which is related to the source properties only. When the phase error is moderate, $1 - \overline{\exp(j(\phi_t)^2} \approx \sigma_{\phi_t}^2$ and ER $\approx C\{\sigma_{A_t}^2 + \sigma_{\phi_t}^2\}$.

## REFERENCES

1. G. E. Trahey, P. D. Freiburger, L. F. Nock, and D. C. Sullivan. "In vivo measurements of ultrasonic beam distortion in the breast," *Ultrason. Imag.* **13**, 71–90 (1991).

2. M. Moshfeghi and R. C. Waag. "In vivo and in vitro ultrasound beam distortion measurements of a large aperture and a conventional aperture focused transducer," *Ultrasound Med. Biol.* **5**, 415–428 (1988).

3. B. D. Steinberg. "Scattering from a multiple random phase screen model of a random inhomogeneous medium," *J. Acoust. Soc. Am.* (submitted).

4. Q. Zhu and B. Steinberg. "Modelling, measurements and correction of wavefront distortion produced by breast specimens," in *Proceedings of an IEEE Ultrasonic Symposium*, 1994, pp. 1613–1617.

5. S. W. Flax and M. O'Donnell. "Phase aberration correction using signals from point reflectors and diffuse scatterers: Basic principles," *IEEE Trans. Ultrason. Ferroelec. Freq. Control* **35**, 758–767 (1988).

6. E. H. Attia and B. D. Steinberg. "Self-cohering large antenna arrays using the spatial correlation properties of radar clutter," *IEEE Trans. Antennas Prop.* **AP-37**, 30–38 (1989).

7. L. Nock, G. E. Trahey, and S. W. Smith. "Phase aberration correction in medical ultrasound using speckle brightness as a quality factor," *J. Acoust. Soc. Am.* **85**, 1819–1833 (1989).

8. M. Fink. "Time reversal of ultrasonic fields—part I: Basic principles," *IEEE Trans. Ultrason. Ferroelec. Freq. Control* **39**, 555–566 (1992).

9. D.-L. Liu and R. C. Waag. "Correction of ultrasonic wavefront distortion using backpropagation and reference waveform method for time-shift compensation," *J. Acoust. Soc. Am.* **96**, 649–660 (1994).

10. Q. Zhu and B. D. Steinberg. "Large-transducer measurements of wavefront distortion in the female breast," *Ultrason. Imag.* **14**, 276–299 (1992).

11. Q. Zhu and B. D. Steinberg. "Deaberration of incoherent wavefront distortion: An approach toward inverse filtering," *IEEE Trans. Ultrason. Ferroelec. Freq. Control* (in press).

12. Q. Zhu and B. Steinberg. "Coherent cancellation of refraction artifacts," in *20th International Symposium on Ultrasonic Imaging and Tissue Characterization*, June 1995, pp. 1367–1370.

13. M. O'Donnell and S. W. Flax. "Phase aberration measurements in medical ultrasound: Human studies," *Ultrason. Imag.* **10**, 1–11 (1988).

14. D.-L. Liu and R. C. Waag. "Time-shift compensation of ultrasonic pulse focus degradation using least-mean-square error estimates of arrival time," *J. Acoust. Soc. Am.* **95**, 542–555 (1994).

15. Q. Zhu, B. D. Steinberg, and R. Arenson. "Wavefront amplitude distortion and image sidelobe levels—part II: In vivo experiments," *IEEE Trans. Ultrason. Ferroelec. Freq. Control* **40**, 754–762 (1993).

16. L. M. Hinkelman, D.-L. Liu, R. C. Waag, Q. Zhu, and B. D. Steinberg. "Measurement and correction of ultrasonic pulse distortion produced by the human breast," *J. Acoust. Soc. Am.* **97**, 1958–1969 (1995).

17. D. Carpenter and G. Kossoff. "Correction of distortion in US images caused by subcutaneous tissues: Results in tissue phantoms and human subjects," *Radiology* **195**, 563–567 (1995).

18. Q. Zhu and B. D. Steinberg. "Wavefront amplitude distortion and image sidelobe levels—part I: Theory," *IEEE Trans. Ultrason. Ferroelec. Freq. Control* **40**, 747–753 (1993).

19. A. Ishimaru, *Wave Propagation and Scattering in Random Media* (Academic Press, New York), 1978.

20. M. Born and E. Wolf, *Principles of Optics* (Pergamon Press, New York), 1980.

21. L. M. Hinkelman, D.-L. Liu, L. A. Metlay, and R. C. Waag. "Measurements of ultrasonic pulse arrival time and energy level variations produced by propagation through abdominal wall," *J. Acoust. Soc. Am.* **95**, 530–541 (1994).

22. Y. Sumino and R. C. Waag. "Measurements of ultrasonic pulse arrival time differences produced by abdominal wall specimens," *J. Acoust. Soc. Am.* **90**, 2924–2930 (1991).

23. B. D. Steinberg, *Principles of Aperture and Array System Design* (Wiley, New York), 1976.

24. B. D. Steinberg. "Radar imaging from a distorted array: The radio camera algorithm and experiments," *IEEE Trans. Antennas Prop.* **AP-29**, 740–748 (1981).

# Regular Issue Papers

# Deaberration of Incoherent Wavefront Distortion: An Approach Toward Inverse Filtering

Qing Zhu, *Member, IEEE*, and Bernard Steinberg, *Life Fellow, IEEE*

*Abstract*—Techniques for the correction of ultrasonic wavefront distortion are compared using measured pulse transmission through human breast specimens. The measured data were obtained by recording the pulse signals on each element of a linear array that was moved in elevation to synthesize a two-dimensional aperture. The one-way point spread functions were reconstructed using matched filtering technique, phase conjugation, time-delay compensation, and backpropagation followed by phase conjugation, each with and without amplitude compression. Two measures of performance were compared, the mainlobe diffraction shape and the ratio of the energy outside the mainlobe to the energy inside the mainlobe. Matched filtering, which compensates the phase distortion but also increases the variation in the modulus, performs more poorly than other techniques with respect to both measures. Phase conjugation and time-delay compensation, which leave the magnitude of the wavefront unchanged, have similar beamwidths but phase conjugation is consistently superior with respect to energy ratio. The backpropagation method, which models wavefront distortion using a phase screen at a computed position between the source and aperture, is shown to perform better. The use of a novel amplitude compression that approaches inverse filtering improves the performance of the compensation techniques significantly. This is because inverse filtering optimizes image fidelity, in contrast, for example, to matched filtering, which optimizes SNR. With the amplitude compression method, the results of the one-way experiments show that the mainlobe shape can be recovered down to −30 dB.

## I. INTRODUCTION

U LTRASONIC WAVEFRONT DISTORTION which includes phase aberration and waveform distortion develops as coherent waves propagate through an inhomogeneous medium, such as the breast. Wavefront distortion sources inside the breast can be modeled as incoherent scattering and coherent multipath interference. Scattering reduces the target strength, broadens the image lobe [1],[2], raises the background level and therefore lowers the image contrast [3]. Multipath interference produces ghost image artifacts or false targets in addition to true targets in the

image [4]. The interference problem is more severe when the aperture is large for high spatial resolution.

Adaptive compensation of wavefront distortion is an active area of current research [5],[6]. Two basic phase deaberration algorithms have been developed in [7]–[9]. The algorithms adjust time delays of received waveforms at different elements of a phased array to compensate delay errors due to an inhomogeneous medium and consequently reduce the scattered energy. Although these two algorithms have been derived from different optimization criteria, their performances are similar; they minimize time delay errors or phase errors but leave waveform *distortion* intact [10]. Nevertheless, phase deaberration algorithms are useful to partially remove phase distortion and build up the strength of the coherent field. Waveform distortion remains, as does residual phase distortion, and together these produce a significantly high background level in the image.

The compensation of wavefront distortion presents a more difficult problem, because there is no general way to reduce waveform distortion. Liu and Waag [11] have improved the time-delay type compensation algorithm by backpropagating the received waveforms to an optimal distance and then performing time-delay compensation at this distance. Backpropagation partially compensates waveform distortion produced by wave propagation from the backpropagation distance to the receiving aperture. We have developed a novel toward inverse filtering approach (TIF) which is a spectrum-amplitude compression technique that, when used in combination with phase deaberration and backpropagation, provides a general means of reducing waveform distortion and therefore reducing the incoherent background level in the image.

## II. TOWARD INVERSE FILTERING APPROACH (TIF)

The following discussions use the correction of a point source image as a means to compare different correction methods and to introduce TIF. But TIF is not limited to point source targets and is applicable to a diffuse scattering medium (see Section V, D), such as the breast. In the remaining text, wavefront amplitude and phase refer specifically to the complex spectral amplitude at each discrete

DEABERRATION TRANSFORMATIONS

MF = matched filter (SNR)
DSA = dominant scatterer algorithm
TRM = time reversal mirror
PC = phase conjugation
TDC = time-delay compensation
BPT = Backpropagation and time-delay compensation
SR = square rooter (compromise amplitude weight)
IF = inverse filter (fidelity)

o  complex sample measured in array  $f = a \exp(j\phi)$
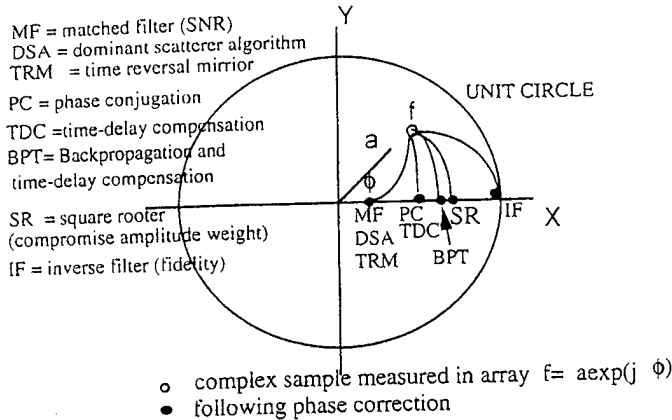●  following phase correction

Fig. 1. Deaberration transformations. $f$ is distortion vector for instantaneous sample of the radiation field. Transformations to the real axis all correct phase. Left (MF) maximizes SNR but increases amplitude distortion. Right (IF) maximizes imaging fidelity but increases noise. SR is good compromise.

frequency within the signal band. The correction method is developed in frequency domain; it allows for frequency dependent changes in both phase and amplitude. TIF combines a spectrum amplitude compression operation with phase deaberration.

Consider complex signal vectors $S_0(x) = A_o \exp(j\psi_o)$ and $S(x) = A \exp(j\psi)$ received across an array in the absence and presence of distortion, respectively. The ratio of $S$ to $S_0$ is a multiplicative distortion vector $f = a \exp(j\phi)$. Fig. 1 shows such a distortion vector $f$ for some instantaneous sample of the radiation field. The optimum compensation transformation is the right-most one, which carries the distortion component of the complex sample to the intersection of the x-axis and the unit circle, for then both amplitude and phase are corrected. The left-most transformation is matched filtering (MF), which squares the amplitude and conjugates the phase. MF is theoretically optimum for maximizing SNR on a white, Gaussian channel. It is an optimum solution for detection (radar) but not so when fidelity is an important criterion, as in imaging. But it does satisfy the requirement for phase correction. Examples of MF algorithms are dominant scatterer algorithm (DSA) [12] and time reversal mirror (TRM) [13]. We should expect that MF algorithms are useful when wavefront distortion resides principally in phase, with amplitude relatively unaffected. Otherwise MF algorithms would be less effective than if amplitude were ignored and phase only were corrected. By squaring the wavefront amplitude, the MF algorithms increase amplitude variance which contributes to the increase of energy in the sidelobe region [3].

A phantom consisting of a random phase screen placed at a receiving transducer models the situation where the element signal samples are correct in amplitude and are distorted only in phase by a random additive component. Phase aberration correction (PAC), consisting of phase conjugation (PC), is then the optimum compensation (see Section V, A). The signal amplitude is unchanged and the phase error is completely compensated by conjugation. This operator is represented by the 2nd (from the left) transformation. Time delay compensation (TDC) [7]–[9] is in the same class.

The right-most transformation which corrects both amplitude and phase is the inverse filter (IF). It is theoretically ideal for fidelity but has drawbacks. Because the IF adjusts the channel gain to be the reciprocal of the signal strength, at points in the receiving aperture where signal strength is weak the enhanced channel gain raises the noise to the point where SNR can be impaired. This is particularly troublesome when there is coherent refractive interference in the receiving array. A second potential problem, which we have avoided by not working too close to the IF point, is that an IF is unstable when the distorting medium has zeroes in the complex plane. Thus the right-most transformation carries the correction too far.

The complex weights of MF, PC, and IF are, respectively, $a$, $1$, and $a^{-1}$, each multiplied by $\exp(-j\phi)$. The signal after weighting is $a^2$, $a$, and $1$. The first and last are far from optimum for the reasons given. The 4th from the left transformation SR is a compromise. The correction vector is $a^{-1/2} \exp(-j\phi)$. The signal after weighting is $a^{1/2}$ (called later rooter). Another transformation to the right of the rooter is fourth rooter (signal amplitude is $a^{1/4}$ after weighting). In general, the correction vector is $a^{-(M-1)/M} \exp(-j\phi)$ and signal amplitude is $a^{1/M}$ after transformation of the Mth rooter; this operation is a *toward inverse filtering* (TIF) approach. In Section IV, we demonstrate that low order rooters (rooter and fourth rooter) when combined with phase deaberration at the aperture can significantly improve contrast resolution without encountering the stability problem.

Backpropagating the received wavefront to an optimal backpropagation distance and performing phase deaberration at this optimal distance (BPT) [11] provides first order correction of wavefront amplitude distortion due to propagation from the backpropagation distance to the receiving aperture and therefore performs better than phase deaberration at the aperture. In Section IV, we demonstrate experimentally that BPT transformation is somewhere to the right of TDC and PC, and left of PC and rooter. We also demonstrate that square rooter in addition to BPT can significantly improve the performance of BPT.

The rooter transformation upon wavefront amplitude is a nonlinear compression operation. Other nonlinear amplitude compression functions which converge toward the inverse filtering solution may also be used in place of the Mth rooter.

## III. EXPERIMENTS

### A. In Vitro Measurement

The 2-D wavefront measurement system and procedure were described in detail in [14] and are summarized here for convenience. A breast tissue specimen was placed in

the specimen holder with the skin facing the direction of the receiving transducer. The source was a hemispherical transducer emulating a virtual point source. The 2-D array consisted of a 92-mm 1-D linear array translated 46 mm perpendicular to its axis to form a synthetic 2-D array 92 mm × 46 mm. The element pitch in the receiving transducer was 0.72 mm and a reflecting mask reduced the receiving elevation to 1.44 mm. Transmission was one-way. Frequency was 3.7 MHz. Bandwidth was 2 MHz. Waveforms were measured at each element, from which 2-D wavefronts were reconstructed as functions of time.

Breast tissue specimens were obtained fresh from reduction mammoplasty surgery and were stored frozen; they were later defrosted and degassed for the experiments. Each specimen was essentially planar and had a surface area of at least $7 \times 11$ cm$^2$. The average thickness was 26.9 mm. The tissue donors were women ranging in age from 18 to 65 with a mean age of 34 years.

Three groups of measurements were made. The primary set consisted of independent measurements using nine different specimens. In addition, two specimens were employed for sequential measurements in which an approximately 1-cm layer was removed from the bottom of the specimen before each subsequent measurement. For three other specimens, a pair of measurements was made with the source in each of two positions located 12 mm apart in the array direction. A total of 16 measurements were made. Water measurement was also made for comparison. In the following analysis, the sequential measurements were treated as measurements from different samples because the samples resulting from approximately 1-cm removal from the original samples were replaced into the sample holder after cutting, and their relative positions to the 2-D transducer aperture changed unpredictably. The pair measurements resulting from 12 mm lateral source translation were also treated as measurements from different samples because the measured parameters and the point-source image properties were changed due to the highly inhomogeneous nature of the breast tissue.

## B. Data Processing

Pulse arrival time at each element was calculated by using a differential edge detector to locate the first negative peak of the pulse. Geometric effects were removed by fitting a two-dimensional, fourth-order polynomial to the calculated arrival time surface and subtracting the result. The reasons for using fourth-order polynomial fitting were given in [11]. 3-D image data were calculated by Fourier decomposition of the temporal waveforms at each $(x, y)$ position in the aperture, calculation of a complex CW 2-D image at each Fourier frequency in the focal plane by using the angular spectrum technique [15], and summation of the 2-D images to form the 3-D transient image. The final 2-D image used in this report was obtained by detecting the peak pressure value at each $(xf, yf)$ position in the image plane within the transient period. Contour maps of

2-D point source images at different thresholds are used to quantitatively evaluate image quality.

Before Fourier decomposition, the received pulse at each element was temporally weighted by a 10-point cosine taper over the trailing 10 points of a 40-point time window that contained the main arrival pulse. The original 40-point interval was padded with zeros to a 128-point interval.

In step one, a frequency range (0.31–6.25 MHz) that contained most of the signal energy was chosen. This range corresponds to the 3rd through 41st harmonic of the FFT of a signal sampled at 20 MHz over a 6.4 $\mu$s interval containing 128 points.

In step two, the complex signals in the $128 \times 32$ spatial aperture were zero padded symmetrically to $256 \times 64$ before each harmonic component in the 2-D aperture was focused in the image plane via the angular spectrum technique. Spatial raised cosine taper was employed. The system bandwidth is about 50%; therefore, $Q = \frac{f_0}{\Delta f} \approx 2$, where $f_0$ is the central frequency. For such $Q$, the first sidelobes (due to finite aperture size) in both principal axes remain [16] and are reduced to about $-30$ dB level by employing the raised cosine taper [17].

## C. Implementation of Correction Methods

Two basic phase deaberration algorithms, time-delay compensation (TDC) and phase conjugation (PC), and two wavefront compensation algorithms, wideband DSA and BPT, were applied to each measured 2-D wavefront set and their effects upon focusing were compared. TIF was implemented by taking rooter and fourth rooter on wavefront amplitude in combination with PC, BPT, and TDC; its effects upon focusing were compared with the other four deaberration algorithms.

*TDC:* An arrival time fluctuation profile at the aperture is calculated in three steps.

Step 1—A reference waveform with good signal-to-noise ratio is first selected from geometrically corrected waveforms. The selected waveform is continuously modified to reduce the effect of the arbitrariness in the initial selection as waveforms in the aperture are cross-correlated with it. The modification is accomplished by time-shifting and adding a new waveform to the reference pulse if the peak value of the correlation function between the new waveform and the current reference waveform is greater than 0.8. The average total number of waveforms that are incorporated into the final reference waveform selection is 2690 (std. 391), which accounts for 66% (std. 9.5%) of the total pulses. The average is calculated upon a total of 16 *in vitro* samples. This selection procedure is similar to the one developed in [11].

Step 2—The arrival time fluctuation profile is first calculated from cross-correlation peaks of geometrically corrected waveforms and the reference waveform when the peak values of the correlation function between the waveforms and the reference waveform are greater than 0.7. At

this step, the average total number of waveforms that are incorporated into the calculation of the arrival time profile is 3518 (std. 173), which accounts for 86% (std. 4.2%) of the total pulses.

Step 3—For the bad waveforms with cross-correlation peaks less than 0.7, the arrival time fluctuations at these positions are calculated as follows: one, calculate cross-correlation peaks between each bad waveform and neighbor waveforms (within a 5 by 5 spatial window) that are incorporated in Step 2; two, select those neighbor waveforms having cross-correlation peaks, calculated in one, greater than 0.5; three, calculate the average of arrival time fluctuation from arrival time differences between the bad waveform and the selected neighbor waveforms, and the arrival time fluctuations of the corresponding neighbor positions. This average is assigned to the bad waveform position. A justification of this step is that, for badly distorted waveforms, they are dissimilar to the reference waveform to a large extent, but they are somewhat similar to the waveforms in the closest neighborhood which are reasonably correlated with the reference waveform. After this step, the average total number of pulses that are incorporated into the calculation of the arrival time profile is 3966 (std. 41), which accounts for 97% (std. 1%) of the total pulses.

For the waveforms that have not been incorporated into the calculation of the arrival time profile after Step 3, arrival time fluctuations at these positions are assigned to zero. The calculated average arrival time fluctuation of the entire 16 profiles is 37.6 ns with a 10.5 ns standard deviation.

Except for TDC, the following correction procedures were implemented upon the complex wavefront at each frequency after Fourier decomposition. The image formation procedures after using each correction method were the same as the procedures described in part B steps 2 and 3.

*PC:* Let $A_f(x,y)\exp(j\phi_f(x,y))$ represent the complex signal at each frequency after Fourier decomposition, where $A_f$ and $\phi_f$ are functions of positions $(x,y)$ in the 2-D array at frequency $f$. The complex weight vector of phase conjugation is $w_f = \exp(-j\phi_f)$ and the signal after weighting is $A_f$. The image formation after phase conjugation is the same as described in part B, steps 2 and 3. Phase conjugation at each frequency within the signal band (without amplitude weight) provides perfect phase compensation except for a $2\pi$ phase jump. The result is better than TDC because of the removal of residual phase error. The wavefront amplitude distortion remains, however. The objective here is to evaluate the limit of phase compensation and the extent of the wavefront amplitude distortion effect.

*Wideband DSA:* The complex weight vector of DSA at each frequency is $w_f = A_f\exp(-j\phi_f)$ and the signal after weighting is $A_f^2$.

Wideband DSA is an approximation of the TRM receive mode developed in [18]. The difference between wideband DSA and TRM receive mode is the scanning procedure.
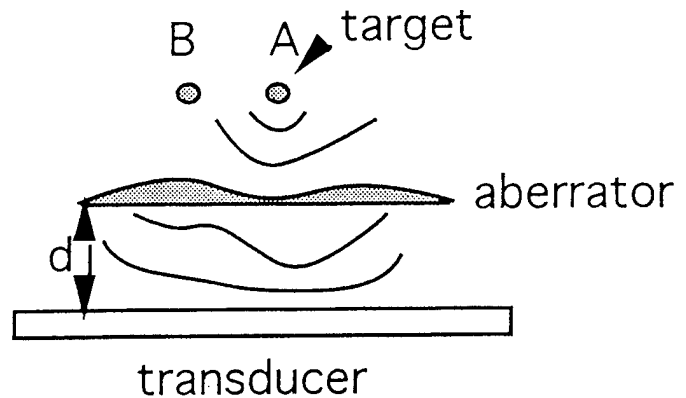


Fig. 2. Scanning configuration.

At target position A (Fig. 2), wideband DSA and TRM receive mode produce exactly the same responses, because of the reciprocity principle. At nontarget position B, wideband DSA uses linear geometry between A and B to scan the beam while the TRM receive mode could backpropagate the wave to the aberrator position, and then use linear geometry to scan the beam [18]. However, for points that are within the correlation distance of A, wideband DSA and the TRM receive mode should produce similar responses. The correlation distance of the breast is about 4 to 5 mm [14], [19]–[21]. Therefore within a 4 to 5 mm radius, we should expect similar performances of wideband DSA and TRM receive mode. The objective of using wideband DSA here is to evaluate the possible improvement of deaberration due to the additional SNR gain provided by amplitude weighting.

*BPT:* BPT, developed in [11], is implemented by backpropagating the complex wavefront at each frequency after Fourier decomposition to the optimal distance and then using *phase conjugation* at that distance. The use of phase conjugation instead of TDC at the backpropagation distance reduces the complexity in the calculation. The backpropagation distances are taken from [14].

*TIF:*

PC and rooter (PC-rooter)—The weight vector of PC and rooter at each frequency is $w_f = A_f^{-1/2}\exp(-j\phi_f)$ and the signal after weighting is $A_f^{1/2}$.

PC and fourth rooter (PC-fourth rooter)—The weight vector at each frequency is $w_f = A_f^{-3/4}\exp(-j\phi_f)$ and the signal after weighting is $A_f^{1/4}$.

BPT and rooter (BPT-rooter)—BPT and rooter was implemented the same as PC and rooter, but the procedure was done at the optimal back propagation distance after backpropagating each complex wavefront to the optimal distance.

TDC and rooter (TDC-rooter)—TDC and rooter was implemented by correcting delay errors in time domain using TDC, and taking rooter on wavefront amplitude at each frequency.

## IV. EXPERIMENTAL RESULTS

### A. Correction of Scattered Energy

*1. Correction Upon Scattering Samples* Figs. 3(a) and (b) show −6 dB contour plots of images obtained from the water path and the 3.5-cm breast tissue path (brs005). Contour spacing is 1 dB. Abscissa and ordinate are azimuth and elevation in millimeters in the image plane. Fig. 3(a) shows the system diffraction pattern at -6 dB. The azimuthal beamwidth is about 1.5 mm (at a distance of 180 mm), meaning that the point (or lateral) resolution is 1.5/180 or 8.3 mrad. Because the size of the receiving array in elevation is half the size in the array direction, the width of the image in elevation is twice as large as in azimuth. When tissue is present Fig. 3(b), the image lobe is broadened. In Fig. 3(b) the beamwidth has grown from 1.5 mm to 3 mm in azimuth and 3.1 mm to 9.3 mm in elevation and the point resolution has worsened approximately 2:1 in azimuth and 3:1 in elevation. A symmetrical scattering pattern appears when the threshold is reduced. Fig. 3(c) shows a −20 dB contour plot of the sample image brs005. Contour spacing is 2 dB. Energy is spread out over a large area. No distinct structure or multipath lobe can be identified from the image.

Fig. 4(a)–(g) shows the correction result of the sample image brs005 by using different methods. Part (h) is the −30 dB level contour of a water path image. The contour spacings in Fig. 4 are the outer contour levels divided by 10. Fig. 4(a)–(c) shows TDC at −6, −20, and −30 dB levels (see Fig. 3(b) and (c) for comparison). Image quality improved significantly and the system diffraction pattern is restored up to −20 dB level. The symmetric scattering pattern outlined by outer contours at the −30 dB level is caused by residual phase errors after phase deaberration and incoherent amplitude distortion. Fig. 4(d) is the correction result of PC at the −30 dB level. Because of the complete removal of phase errors except for a $2\pi$ jump, the scattering pattern is further improved as compared to Fig. 4(c). Fig. 4(e) is the result of BPT, and the scattering pattern is much better than that of PC at the aperture. The optimum backpropagation distance of this tissue sample is 30 mm. Fig. 4(f) is the correction result of PC-rooter at −30 dB. The pattern is very close to the system diffraction pattern (see (h) for comparison). Fig. 4(g) is the result of wideband DSA at the −30 dB level. The correction result is worse than those of other methods (see Section V, C).

*2. Correction Upon Samples with Well-defined Multipath* In most breast samples, scattering and coherent interference are both present. Fig. 5(a) and (b) are −10 dB contour plots of images obtained from the water path and the 4-cm breast tissue path (brs006). Contour spacing is 2 dB. In tissue image Fig. 5(b), three lobes instead of one central image lobe appear. Inner contours of the image lobe are close to the system diffraction pattern (Fig. 5(a)) while the outer contours are highly irregular due to scattering. The point resolution is worsened by approximately
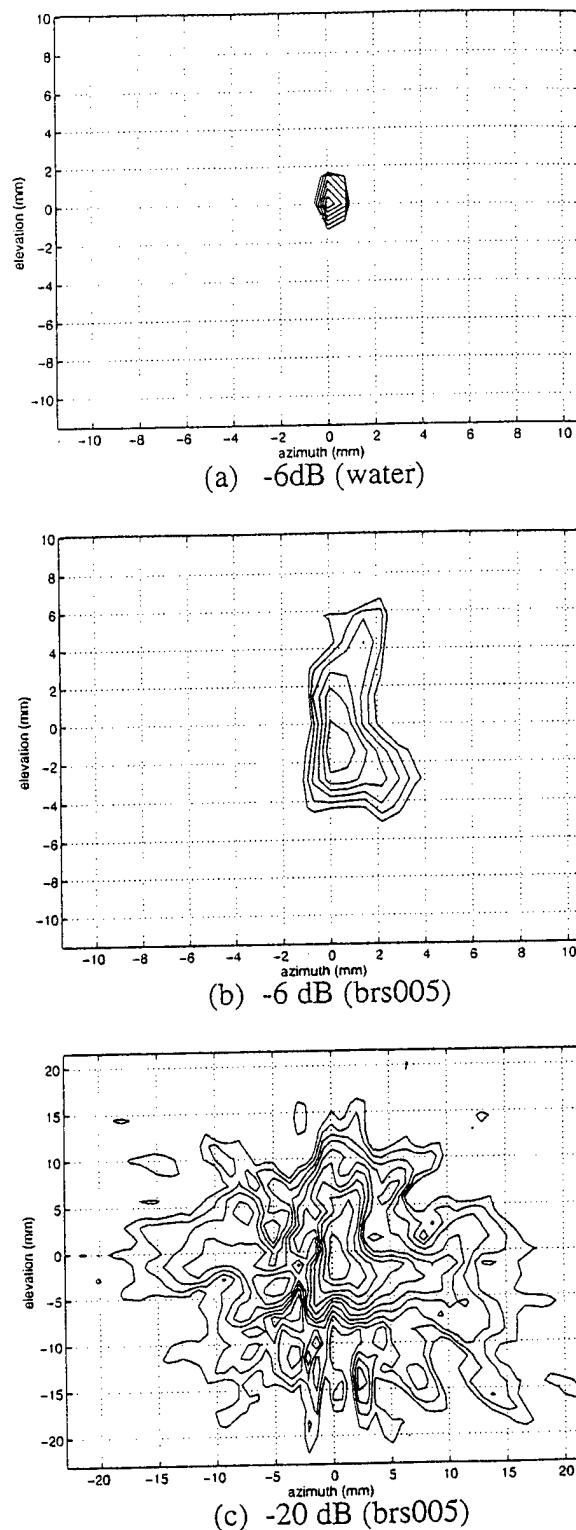


(a)  -6dB (water)



(b)  -6 dB (brs005)



(c)  -20 dB (brs005)

Fig. 3. 2-D contour maps of point source images. (a) Water data showing diffraction pattern of system. Outer contour is −6 dB level. (b) Measured through the 3.5-cm tissue (brs005), showing asymmetric scattering effect. Outer contour is −6 dB level. (c) Image brs005 at −20 dB contour level. The outer contour shows symmetrical scattering pattern. No distinct structure or multipath is observed. Note the change of scale from (a) and (b).
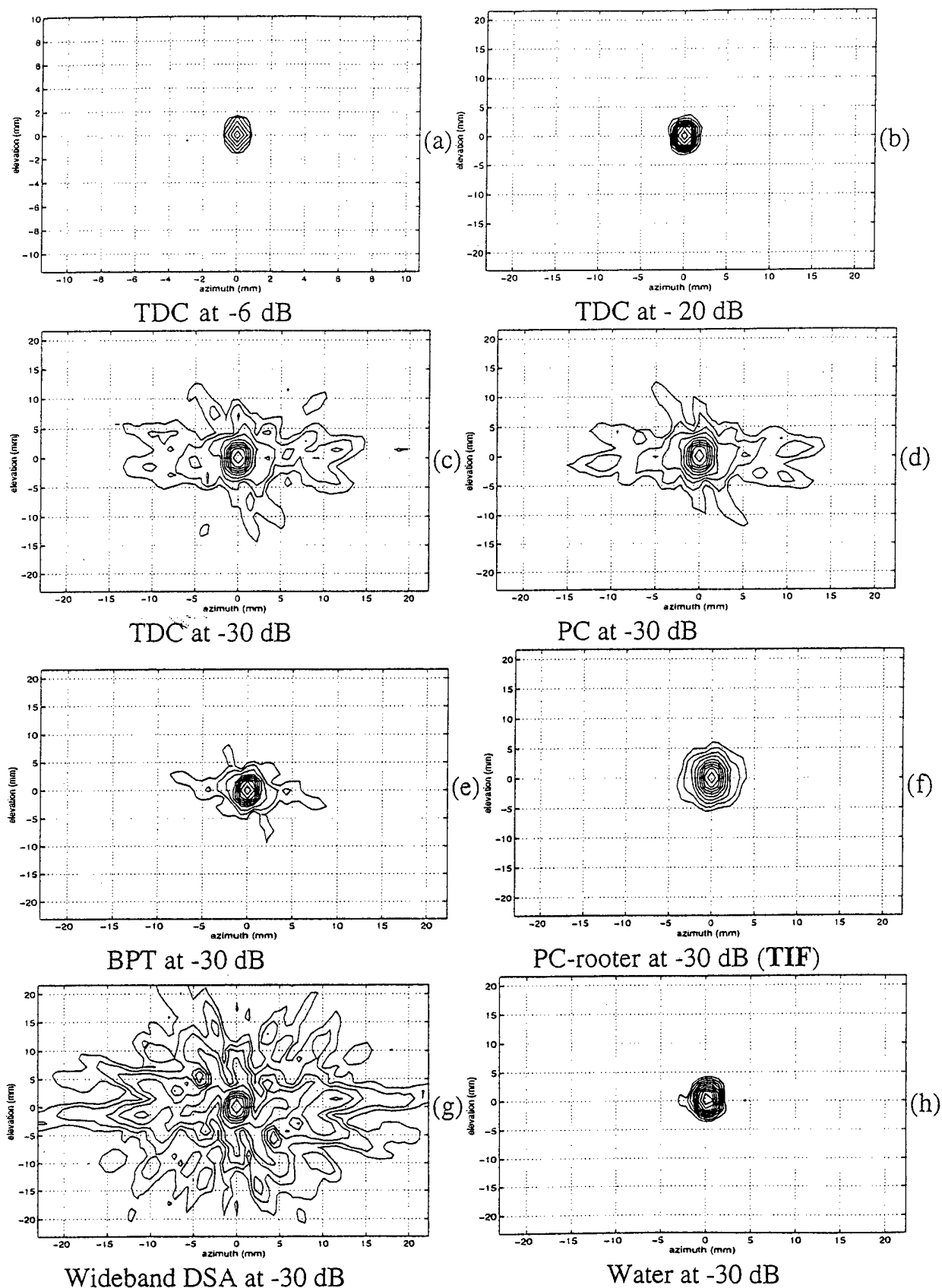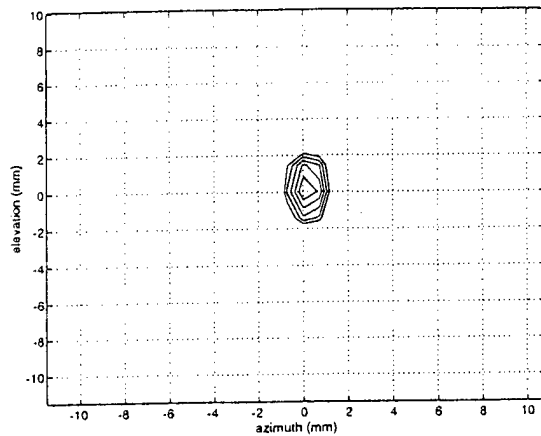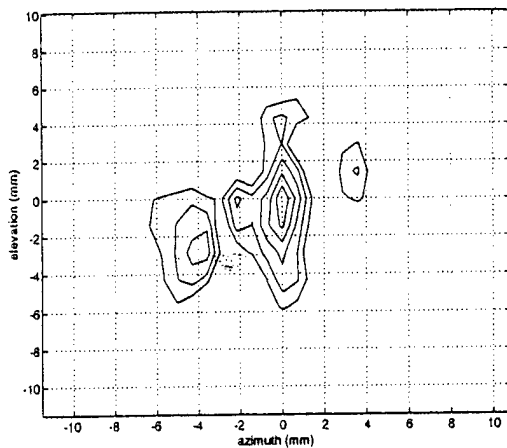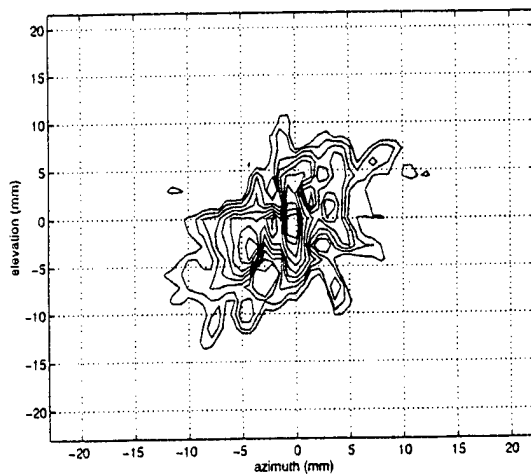
Fig. 4. Distortion corrected contour maps of the sample image brs005 (see Fig. 3(b) and (c) for comparision) (a) TDC at −6 dB. (b) TDC at −20 dB. (c) TDC at −30 dB. (d) PC at −30 dB. (e) BPT at −30 dB. (f) PC-rooter at −30 dB. (g) Wideband DSA at −30 dB. (h) Water at −30 dB. Note the scale change of (b)–(h) from (a).

(a) -10 dB (water)



(b) -10 dB (brs006)



(c) -16 dB (brs006)

Fig. 5. 2-D contour maps of point source images. (a) Water data showing diffraction pattern of system. Outer contour is −10 dB level. (b) Measured through the 4-cm tissue (brs006), showing highly asymmetric interference pattern. Outer contour is −10 dB level. (c) Image brs006 at −16 dB contour level. The outer contour shows more symmetrical scattering pattern. Note the change of scale from (a) and (b).
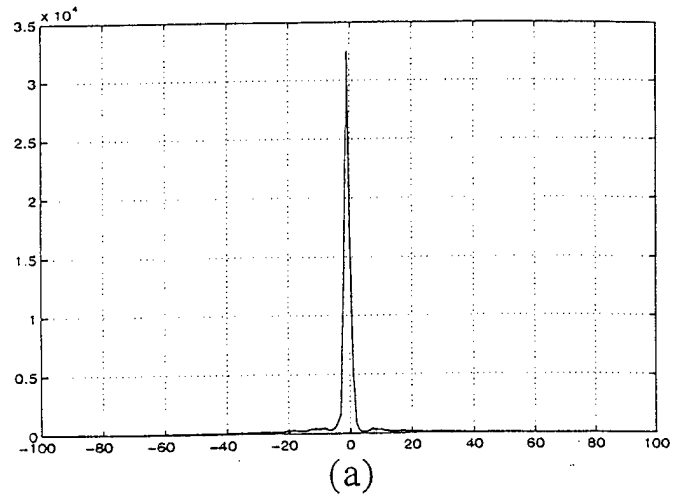


(a)
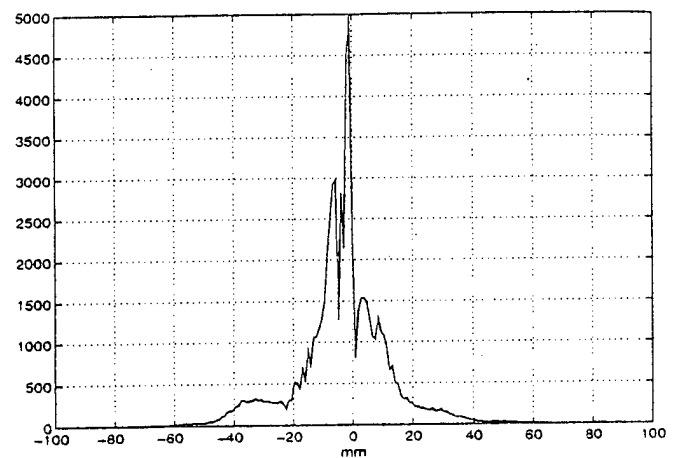


(b)

Fig. 6. (a) 45 degree cuts of 2-D images; water. (b) brs006.

2:1 in azimuth and 3:1 in elevation. Two refractive lobes appear at $(-4, -2.5)$ and $(3.5, 1.5)$, and their strengths are −6 and −8 dB. A closer examination is obtained from 45 degree cuts (Fig. 6) of the Fig. 5(a) and (b) images. In Fig. 6(a), the peak sidelobe is −36 dB, which is the best we can obtain from the measurement system. In the tissue image, two large sidelobes (−6 dB and −8 dB) appear on either side of the mainlobe. The two nulls between the lobes are deep (left: −13 dB below peak, right: −15 dB), which is a typical coherent interference phenomenon.

A symmetric scattering pattern generally appears when the threshold is reduced, as shown Fig. 6(c) with a −16 dB threshold contour and contour spacings of approximately 1.5 dB. The outer contours show a roughly symmetric pattern typical of scattering while the inner contours show an asymmetric lobular interference pattern.

Fig. 7 shows correction results of the sample image brs006 after applying different methods. The contour spacings are the outer contour levels divided by 10. Fig. 7(a) is the −16 dB contour map of applying TDC (see Fig. 5(c) for comparison). Image quality improved significantly because of the minimization of the phasefront distortion caused by
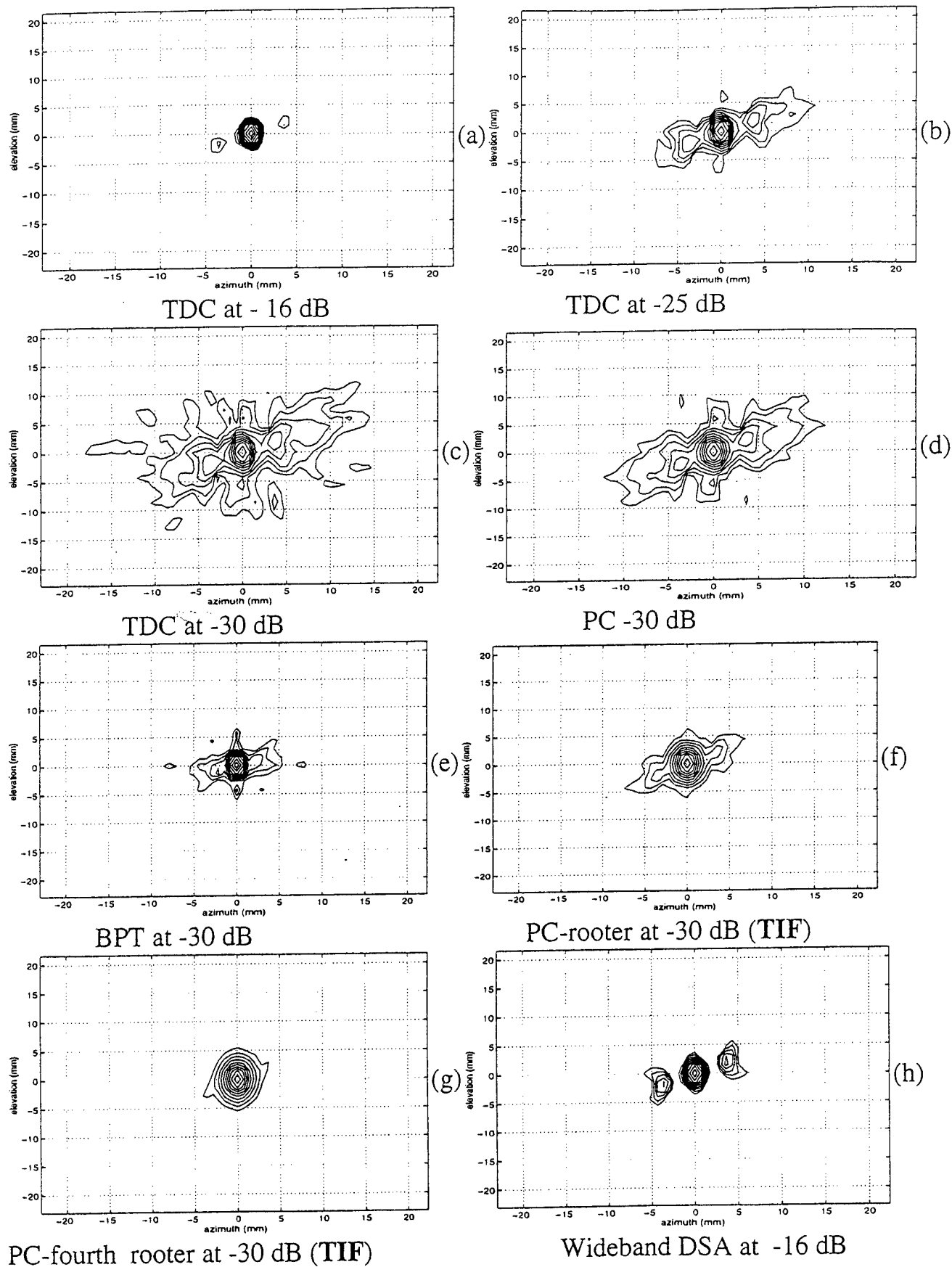
Fig. 7. Distortion corrected contour maps of the sample image brs006 (see Figs. 5(b) and (c) for comparision) (a) TDC at −16 dB level, (b) TDC at −25 dB level, (c) TDC at −30 dB level, (d) PC at −30 dB level, (e) BPT at −30 dB, (f) PC-rooter at −30 dB, (g) PC-fourth rooter at −30 dB, (h) Wideband DSA at −16 dB. Artifacts are 5 dB higher than time-delayed correction shown in Fig. 7(a).

scattering. The area within the −16 dB inner contour is reduced by a factor of 11. The mainlobe pattern is close to the system diffraction pattern, although the area is still 1.6 times larger than the area in water at the same level. Two large lobes remain as expected and appear as two additional sources. Fig. 7(h) is the correction result at a −16 dB level of applying wideband DSA. It is evident that the procedure enhances interference in this example; the artifacts are 5 dB higher than in Fig. 7(a). The reason is given in [3]. Figs. 7(b) and (c) show −25 and −30 dB contour plots of TDC. In Fig. 7(b) the outer contours show an asymmetric interference pattern with scattered energy distributed around the two interference lobes. In Fig. 7(c) the outer contours show the more symmetric scattering pattern caused by incoherent wavefront amplitude distortion and residual phase distortion. Fig. 7(d) is the result of PC at −30 dB. The approximately symmetric scattering pattern outlined by outer contours in (c) is improved due to better phase deaberration. The energy is more concentrated around the image lobe and interference lobes. Part (e) is the result of BPT, and the scattering pattern is further improved as compared with the result of PC at the aperture. The backpropagation distance of this sample is 50 mm. Part (f) is the result of PC-rooter at −30 dB. The pattern is very close to the system diffraction pattern. PC-fourth rooter shown in Fig. 7(g) restores the diffraction-limited image to a −30 dB level.

It is interesting to note that the strengths of the two interference lobes are also reduced by 8 dB after TDC and PC. They are further reduced by 5, 7, and 15 dB after BPT, PC-rooter, and PC-fourth rooter, respectively. The improvement comes from the scattered energy which is originally distributed around the mainlobe and each of the refracted multipath lobes. This energy is coherently added back, by the deaberration process, to the dominant lobe, which in this case is the mainlobe. The overall result is an improvement of the image lobe to the interference lobe ratio.

Determination of whether interference was coherent or scattered was based upon whether or not large lobes could be removed by applying phase-deaberration algorithms. Another indicator is whether or not a lobe location moves (scattering) or remains relatively the same (refraction) after the phase deaberration process. Both means were used to identify whether these lobes were produced by refraction or scattering. Large lobes in nine samples are believed to be caused by the interference process. In these samples, we have found an average of a 10 dB (std. 4dB) improvement in the range of 5 to 16 dB after TDC, due to the coherent strengthening of the mainlobe.

## B. Statistics

*1. Point Resolution and Refractive Artifacts* We analyzed images at different contour levels and classified the total of 16 samples into three categories: primarily scatter (4 samples), more scatter than refraction (3 samples), and scatter plus well-defined refraction (9 samples). Statistics

TABLE I
STATISTICS OF INCREASE IN −6 dB BEAMWIDTH (PERCENT).

| Sample size | Classification | Azimuth | Elevation |
|---|---|---|---|
| 4 | A | 130 (std. 131.3) | 100 (std. 96.5) |
| 3 | B | 50 (std. 53.3) | 30 (std. 30.0) |
| 9 | C | 30 (std. 33.3) | 40 (std. 42.2) |

A. Primarily scatter
B. More scatter than refraction
C. Scatter plus well-defined refraction

TABLE II
STATISTICS OF REFRACTED LOBES FROM 9 *In Vitro* BREAST SAMPLES.

| | Average | Std. Dev. |
|---|---|---|
| Number of refractive lobes | 2 | 0.53 |
| Relative peak strength (dB) | 10 | 4.7 |
| Distance from primary lobe (deg) | 1.8 | 0.57 |

of -6 dB point resolution of three groups is given in Table I. The average beam-broadening as compared with water is 70% in azimuth and 57% in elevation. These numbers are larger than the result reported in [21] where an 18% increase in beamwidth at the same threshold is observed. This is likely due to the different aperture sizes used. For the samples with refractive artifacts, the point resolution is evaluated upon the central image lobe. The percentage increase in beamwidth of the scatter group is significantly larger than that of the other two groups. It is obvious that point resolution is not enough to evaluate image distortion when multiple lobes are present. Statistics of refractive lobes of the third group is given in Table II. In this group, we found 1–3 refractive lobes at levels between −4 and −17 dB (peak value), all within a radius of 1–3°.

*2. A Measure of Contrast* Contrast is the measure used to quantitatively evaluate improvement upon image quality through the use of different correction algorithms. Image contrast is the metric of the brightness point in an image to the peak background, i.e., it defines the dynamic range window between target strength and background (noise, scatter, refractive artifacts). It is similar to sidelobe level as a measure of quality of a radiation pattern [17]. In a point source image, the measurement can be made by direct observation of the background peak. However, in most cases the background peak occurs on the skirts of the main diffraction lobe of the target and its amplitude cannot be directly discerned. Its effect is to distort the mainlobe. In these cases, contrast is measured down to the lowest level at which mainlobe diffraction shape is maintained. The mainlobe diffraction shape is identified when the elevation-image width to the horizontal width is approximately a 2 to 1 ratio, and the outermost image contour has an elliptical shape. The evaluation is done by visual inspection at each contour level until the criteria are met. At the levels selected, 65% of ratios are within 0.1 of 2 to 1, 27% within 0.2 of 2 to 1, and 8% within 0.3.

TABLE III

STATISTICS OF THE LOWEST LEVEL OF MAINLOBE DIFFRACTION SHAPE (DB).

| Diffraction pattern (dB) w/o correction | | TDC | PC | Diffraction pattern after correction (dB) | | | | |
|---|---|---|---|---|---|---|---|---|
| | | | | Wideband | BPT | PC-rooter | BPT-rooter | PC-fourth rooter |
| A | −0(0) | −18.8(1.9) | −19.0(2.2) | −14.8(2.6) | −24.3(2.1) | −25.3(3.0) | −29.5(2.7) | −32.3(2.8) |
| B | −5.8(1.3) | −19.7(2.3) | −19.7(3.5) | −14.7(1.5) | −23.7(0.6) | −25.3(2.1) | −29.3(2.3) | −30.7(1.2) |
| C | −6.1(3.5) | −19.3(2.7) | −19.6(2.5) | −14.8(2.5) | −23.9(2.4) | −25.4(2.5) | −29.3(3.0) | −30.7(1.4) |

The average levels (std. dev) of the restored mainlobe diffraction shape before and after corrections of the three groups classified earlier are given in Table III. The mainlobe shape is restored up to −19.3 (2.4) and −19.5 dB (2.6 dB) by using two phase-deaberration algorithms, TDC and PC, respectively. The fact that the correction result of TDC is very close to that of PC suggests that the limit of phase correction with respect to the selected metric has been achieved by TDC. Further improvement requires correction algorithms that can take wavefront amplitude distortion into account. Wideband DSA is able to restore the mainlobe shape to −14.8 dB (2.3 dB). This result is about 5 dB worse than that of using two phase-deaberration algorithms. The cause is the increase of wavefront amplitude variance by squaring the amplitude. Wavefront amplitude variance contributes to the energy in the sidelobe region [3]. BPT at an optimal backpropagation distance improves the performance of PC at aperture by 5 dB. PC-rooter restores the mainlobe diffraction shape to −25.4 dB (2.6 dB). The correction result of BPT is similar to PC-rooter. PC-fourth rooter achieves a −31.1 dB (1.7 dB) level, which is about a 12 dB improvement beyond two phase deaberration algorithms. This level is very desirable for a high quality ultrasound echo scanner. BPT-rooter further improves BPT by another 5 dB.

The restored mainlobe diffraction levels among different groups are similar when different correction methods are used. But the improvements are, in general, 6 dB larger in the scatter group than that of the other two groups because the mainlobe shape is distorted at zero dB in the scatter only group.

*3. Depth-dependent Distortion and Correction* Scattered energy increases with the propagation depth $D$. Using first order approximation, it is shown analytically in [3] that wavefront amplitude variance $\sigma_{A_t}^2$, and phase variance or arrival time variance $\sigma_\tau^2$, linearly increase with depth. $\sigma_{A_t}^2$ is calculated as follows: calculate energy at each $(x, y)$ position at the aperture by summing the energy over the time window, calculate amplitude at each $(x, y)$ position by taking the square root of the energy, calculate the reference amplitude profile which is the fourth order polynomial fit of the measured amplitude profile, and calculate normalized amplitude variance of the measured amplitude profile divided by the reference amplitude profile. The calculation of $\sigma_\tau^2$ is described in Section III, C. Fig. 8 shows the linear regression plots of $\log(\sigma_\tau^2)$ and $\log(\sigma_{A_t}^2)$ vs. $\log(D)$. A total of 16 independent measurements with sample thickness ranging from 1 to 4 cm (see Section III, A) are included
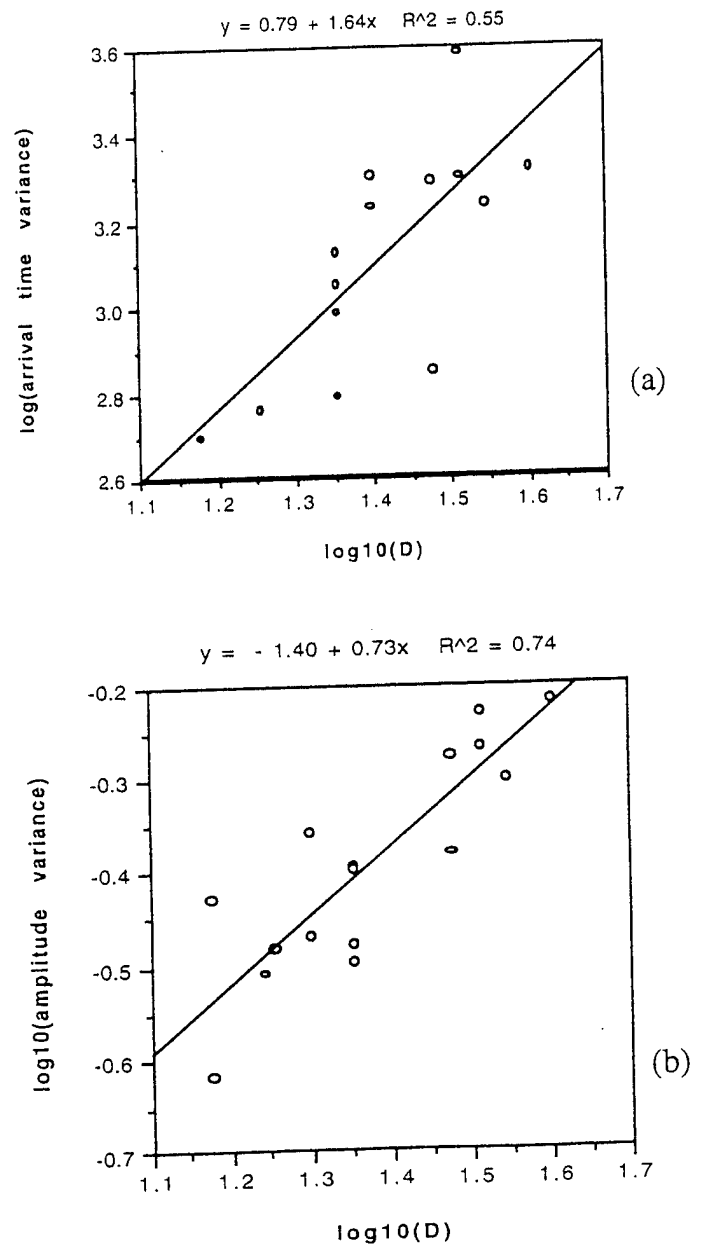


Fig. 8. Linear regression of (a) $\log(\sigma_\tau^2)$ vs. $\log(D)$ and (b) $\log(\sigma_{A_t}^2)$ vs. $\log(D)$. $D$ is in millimeters, arrival time variance $\sigma_\tau^2$ is in ns$^2$ and $\sigma_{A_t}^2$ is the normalized amplitude variance (no dimension).
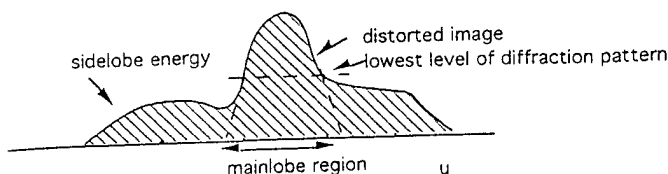
Fig. 9. ER measurement. Mainlobe region of distorted image is identified by extrapolating between image peak and the lowest level of diffraction pattern (see the two dashed lines). Mainlobe and sidelobe energies of the distorted image are obtained by integrating the energy inside and outside the mainlobe region.

in the regression study. Two outliers are removed from Fig. 8(a). The correlation coefficients are 0.55 and 0.74, respectively. The slopes are in the order of unity. In both plots, the linear relationships are statistically significant[1]. The low correlation coefficient in Fig. 8(a) is due to the difficuty of estimating arrival time profiles when the waveforms are highly distorted. However, the general growth of $\sigma_\tau^2$ with depth $D$ indicates that scattered energy increases with $D$.

A quantitative measure of scattered energy at the image plane is the energy ratio ER, which is defined as the energy outside the main image lobe to the energy inside the main image lobe. It is shown analytically in [3] that ER linearly grows with the propagation distance $D$. ER is directly related to image contrast and is calculated by taking the ratio of energies measured outside the mainlobe region and inside the mainlobe region. The mainlobe region is identified by linear extrapolation between the peak image value and the outer contour of the mainlobe diffraction pattern at the lowest recognizable level. Fig. 9 illustrates the measurement procedure. Fig. 10(a) upper curve is the linear regression plot of ER vs. $D$ without correction. One outlier was removed from the data. ER in water image is 0.088, which is included in the data points to represent system performance at zero depth. The correlation coefficient is 0.49 and the linear relationship is significant. The low correlation coefficient is due to the difficulty of identifying the diffraction pattern for some severely distorted images. In Fig. 10, all regression lines are extrapolated to 50 mm propagation depth, which is considered the average penetration depth of breast under compression.

The performances of descattering algorithms deteriorate with propagation depth. The rest of the regression curves in Fig. 10(a) and all regression curves in Fig. 10(b) show ER vs. propagation depth when seven different correction methods are used. The regression curve obtained from PC show in Fig. 10(a) is also included in Fig. 10(b) for comparison. ERs in water alone data provided the values at zero depth. The correlation coefficients of regression curves are indicated in Fig. 10 by R. The linear relationships are statistically significant for all curves. The average values of ER (std. dev.) are given in Table IV.
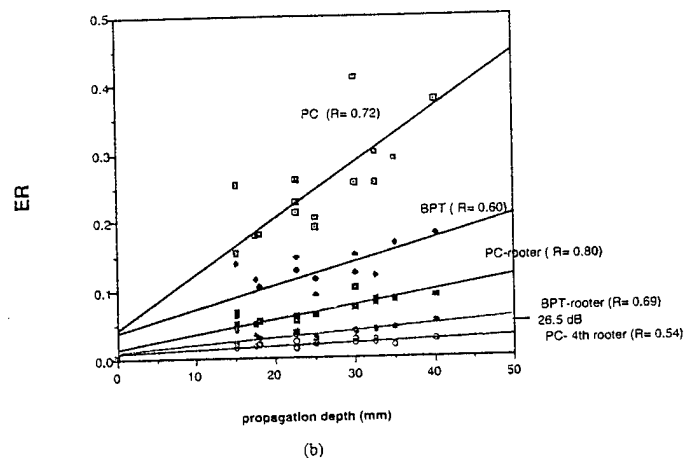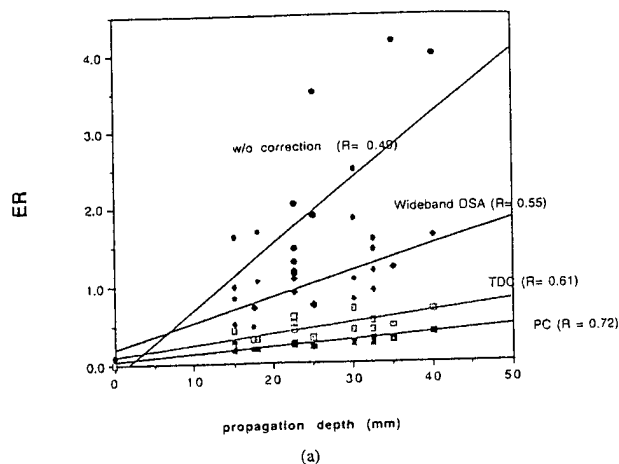


(a)



(b)

Fig. 10. (a) Linear regression curves of ER vs. propagation depth obtained from without correction and three correction procedures. (b) Results of ER vs. propagation depth obtained from five correction procedures. The vertical scales of (b) is the predicted image contrast (see text).

The performance of wideband DSA is the lowest among all correction procedures. Data sets of wideband DSA, PC and PC-rooter are clearly separated with averages 103% (std. 33.9%), 25% (6.9%), and 6.8% (1.6%), respectively. The ER ratios of wideband DSA and PC, and PC and PC-rooter are 4.1 and 3.7, respectively. These results agree very well with the factor of 4 prediction given by analysis in [3]. The average ER after TDC is 19% more than that of PC while the averages of the lowest level at which mainlobe diffraction shape is maintained are the same when TDC and PC are used. This implies that the residual phase error due to imperfect phase correction contributes primarily to energy in the sidelobe lobe region. BPT reduces the average ER by 12.2% below that of PC and is the best among the linear operations. The performance of PC-rooter at the aperture is better than that of BPT. At 50 mm depth, the PC-rooter curve reaches 0.12 which is about the average ER level with BPT correction at the average 2.7 cm propagation depth. Therefore, this ER is likely to result in 24 dB image contrast at this depth. At 50 mm, the regression curves of BPT-rooter and PC-fourth rooter reach

---

[1]The linear relationship is statistically significant ($\alpha = 0.05$) if the correlation coefficient is greater than 0.53 for sample size 14 and 0.497 for sample size 16.

TABLE IV
Statistics of ER Before and After Corrections.

| w/o Corr. | TDC | PC | Wideband DSA | BPT | PC-rooter | BPT-rooter | PC-fourth rooter |
|---|---|---|---|---|---|---|---|
| 214.7% (std. 130.1%) | 44.2% (13.4%) | 25.1% (6.9%) | 103.5% (33.9%) | 12.8% (2.9%) | 6.8% (1.6%) | 3.7% (0.7%) | 2.1% (0.4%) |

0.06 and 0.03, respectively. These ERs are about the average levels of PC-rooter and BPT-rooter obtained from the average 2.7 cm depth. These results indicate that focusing with image contrast of 25 to 29 dB throughout the 50 mm propagation depth may be achievable by taking the low order root on wavefront amplitude in combination with phase deaberration at the aperture or with BPT.

Image contrast, the lowest level of the mainlobe diffraction shape, increases monotonically with ER. The relation of the two can be predicted by using ER and image contrast obtained with PC (or any correction method) as a base line (bold numbers in Table V). For example, the measured image contrast with PC is 19.5 dB. The ER ratio of PC alone to PC-rooter is 25.1/6.8 = 3.7, corresponding to an increase of 5.7 dB. Thus the predicted image contrast is 19.5 dB + 5.7 dB = 25.2 dB, which closely agrees with the measured value 25.4 dB. Table V lists the measured ER (first row), predicted image contrast from the measured ER (second row), and the measured image contrast (third row). The predicted and measured image contrasts are in reasonably good agreement except for the pair without correction. The reason is due to ER measurement error in images without correction. For some severely distorted images, it is often difficult to identify the mainlobe region.

Refracted energy exhibits a different depth distortion effect than scattered energy. The strengths and the numbers of interference lobes depend on orientations, curvatures, sizes, and numbers of refractive bodies in the insonified medium, and may not be directly related to propagation depth. Although the chance of incident rays passing through more refractive bodies increases with the propagation depth, the strengths of interference lobes resulting from multiple refraction may not be significant compared with those resulting from single refraction. One quantitative measure of coherent interference phenomenon is the ratio of a large interference lobe or artifact to image lobe. For nine samples that were determined to have significant levels of coherent interference, the ratio varied randomly from sample to sample and showed no increase with thickness. The average strength (peak value) is 10 dB (std. 4 dB). Another quantitative measure is the total number of large refractive lobes in each image (Table II). The average is 2 and standard deviation is 0.53. The lobe number is independent of propagation depth. The refractive lobes are tightly clustered around the main lobe with an average radius of 5.6 mm (std. 1.8 mm) which is about 2 degrees. This is because the speed variations across glandular tissue and fat boundaries are small (5–10%).

## V. Discussion

### A. Comparison of TDC and PC

Experimentally we found that PC and TDC, which leave the magnitude of the wavefront unchanged, have similar performance with respect to beamwidth but PC is consistently superior with respect to energy ratio. The following analysis explains the reason.

We model the received pulse as the transmitted pulse, $p(t)$, convolved with the medium induced distortion, i.e., $r(t, x_i) = p(t) * m(t, x_i)$, where $m(t, x_i)$ is the impulse response of the medium from the source position to the receiver element $x_i$. Assume that system noise is negligible. The estimation of the arrival time profile of $r(t, x)$ across the receiving aperture is calculated by cross correlation of neighboring signals as:

$$O = \max_{\tau} \left[ \int_{-\infty}^{+\infty} p(t) * m(t, x_i) \times p(t) * m(t - \tau, x_j) dt \right].$$

The quality of the estimated profile is highly affected by the waveform distortion $m(t, x_i)$ across the receiving aperture, i.e., the estimation of arrival time profile is coupled with the wavefront amplitude distortion. In the frequency domain, $R(\omega, x_i) = P(\omega) \times M(\omega, x_i)$, where the medium distortion $M(\omega, x_i)$ has amplitude $a(\omega, x_i)$ and phase $\exp(j\omega t_0(x_i))$. Since $\exp(j\omega t_0(x_i))$ is decoupled from the amplitude of $R(\omega, x_i)$ by multiplication, the phase conjugation operation at each frequency completely compensates $t_0(x_i)$ independent of amplitude error. Therefore, PC is better than TDC in correcting residual phase error, which primarily contributes to the energy in the sidelobe region.

### B. Importance of Better Phase Correction

We have shown in Table IV that PC, the best phase deaberration procedure at the aperture and ideal for a point target, improves ER 19% more than TDC, while the averages of the lowest level at which mainlobe diffraction shape is maintained are the same by using both procedures. This implies that residual phase error due to imperfect phase correction of TDC primarily contributes to the energy in the sidelobe region. Therefore, better phase deaberration procedures that improve the performance of TDC are valuable to improve the contrast resolution.

The procedure to calculate TDC profile used in this paper is ad hoc. Steps 2 and 3 in the TDC calculation (Section III) smooth the arrival time fluctuation estimate to a

TABLE V
RELATION OF ER AND IMAGE CONTRAST (PREDICTED AND MEASURED).

|  | w/o Corr. | TDC | PC | Wideband DSA | BPT | PC-rooter | BPT-rooter | PC-fourth rooter |
|---|---|---|---|---|---|---|---|---|
| ER | 214.7% | 44.2% | 25.1% | 103.5% | 12.8% | 6.8% | 3.7% | 2.1% |
| (predicted) | −10.2 (dB) | −17.1 | −19.5 | −13.3 | −22.4 | −25.2 | −27.8 | −30.3 |
| (measured) | −4.2 (dB) | −19.3 | −19.5 | −14.8 | −24.0 | −25.4 | −29.4 | −31.1 |

certain extent. To test the effect of the ad hoc smoothing, another TDC estimate procedure was used. We call this procedure nonsmoothing TDC. In this procedure, the reference waveform selection in the previous TDC estimate was unchanged, but steps 2 and 3 were replaced by simply calculating the cross-correlation peaks of correlation functions between geometrically corrected waveforms and the reference waveform. The image formation was the same as before. Contrast and ER after using nonsmoothing TDC, were measured. The average level of the lowest mainlobe diffraction shape is −18.9 dB (std. 2.4 dB) and the average ER is 41.4% (11.2%). The corresponding results of using smoothing TDC are −19.3 dB (std. 2.4 dB) and 44.2% (13%). Thus, smoothing does not significantly improve image quality. The reasons are an average 86% of pulses are highly correlated with the reference waveform (correlation coefficient 0.7) and arrival time fluctuations calculated at these positions are reasonably good, and for 14% of pulses that are not correlated well with the reference waveform, estimation errors of arrival time fluctuation occur at these positions. But signals at these positions are, in general, weak and therefore arrival time estimation errors at these positions contribute little to image quality.

## C. Effects of Amplitude Weight of Compensation Vector

The complex weights of MF, PC, and PC-rooter are, respectively, $A_f$, 1 and $A_f^{-1/2}$, each multiplied by $\exp(-j\phi)$. The signal after weighting is $A_f^2$, $A_f$ and $A_f^{1/2}$. By using first order approximation, it is shown in [3] that the variance of $A_f^2$ is about four times larger than $\sigma_{A_t}^2$ while the variance of $A_f^{1/2}$ is about four times smaller when a narrowband waveform is used, where $\sigma_{A_t}^2$ denotes the variance of $A_f$. These increases and decreases in amplitude variance account for the linear increase and decrease in sidelobe energy ER [3]. Experimentally, we measured a 4.1 and 3.7 increase and decrease in ER compared with the ER of using PC when wideband DSA and PC-rooter are used, respectively (Table IV). The results agree with the analysis and indicate that intelligent use of amplitude weighting is crucial for improving image contrast.

## D. Application of TIF to Pulse-echo and Diffuse Scattering Medium

TIF is applicable to wavefront compensation on receive in pulse-echo. The received wideband waveforms are
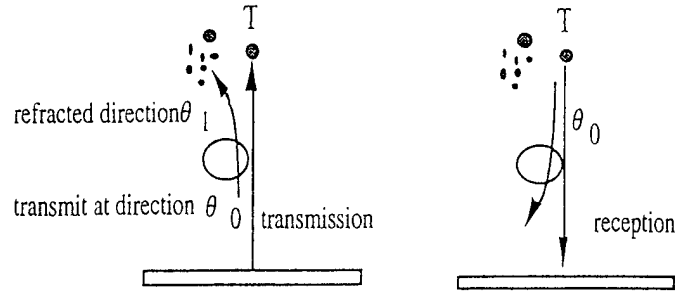


Fig. 11. Effect of refraction upon pulse echo imaging (simplest case with no interference echo signal coming back from targets insonified by subbeam).

treated exactly as in one-way propagation, i.e., they are decomposed using Fourier decomposition technique and TIF can be implemented at each discrete frequency. TIF does not require a point target in the medium. Our experiments with square root amplitude weighting and the time domain correction algorithm TDC have shown that ER can be reduced by 15.6% on average relative to TDC alone.

## E. Significance of Coherent Interference in Pulse-echo Imaging

A coherent interference phenomenon was demonstrated in the 1-way transmission model and experiments. Its impact upon 2-way echo scanning is illustrated in Fig. 11. A transmitting beam illuminates a tumor or target T (part a). Because of refraction, a subbeam is split from the original beam and insonifies targets along $\theta_1$. On reception, if no echo signal is coming back from the targets illuminated by the subbeam (simplest case), the receiving beam upon T (part b) may split in the same fashion as the transmitting beam (reciprocity) and a dual image may result. This simplest case corresponds exactly to the situation in the 1-way transmission experiments reported in this paper, and in [13]–[15], where an active point source instead of a passive point target is used. In reality, refracted energy from the targets insonified by the subbeam will arrive at angles of 1 to 3° from the target direction and, therefore, in the sidelobe region of array. The sidelobe level of the receiving beam will be ∼ −30 dB as achieved by the procedure described in this paper. The average level of refracted multipath is found to be −10 dB relative to the target image and therefore the average multipath signal level entering the system is ∼ (10+30) dB below the echo strength of the

illuminated target. Cancellation algorithms [22] must further suppress these multipath signals to achieve a −60 dB contrast resolution, which is essential for preventing contamination of otherwise black cysts with scattered and/or refracted echo energy and thereby causing them to look like speckled tumors.

## VI. Conclusions

The evidence of both scattering and refraction is observed from point source images obtained from *in vitro* breast samples with thickness varying from 1 to 4 cm. Scattering reduces target strength, broadens the mainlobe and increases background level and, therefore, lowers the image contrast. Refraction creates coherent multipath interference that produces false targets in addition to the true target in the image. Scattered energy increases with the propagation depth while refracted energy does not appear to increase with the depth.

Phase deaberration algorithms are useful to partially remove scattered energy and build up the strength of the coherent image. As a result, the diffraction-limited image is restored up to −20 dB level for average thickness of 2.7 cm. Better phase deaberration procedures are valuable to improve energy ratio and therefore image contrast. Improvement of a diffraction-limited image to the −30 dB region requires wavefront-deaberration algorithms that can further remove scattered energy caused by wavefront amplitude distortion and consequently strengthen the coherent image. BPT reduces wavefront amplitude variance and provides 5 dB improvement in addition to that of using phase deaberration procedures at the aperture. Wideband DSA increases wavefront amplitude variance and the result is 5 dB worse than phase-deaberration procedures alone for the tissue thickness studied. TIF, which combines low-order-root spectrum-amplitude compression with phase-deaberration or BPT, can further reduce the amplitude variance and restore the diffraction-limited image to the −30 dB region. Linear regression analysis of ER vs. propagation depth indicates that high quality focusing as far as 50 mm propagation depth is possible.

The ratio of multipath artifact to image lobe is improved by an average of 10 dB when phase deaberration is used and further improved by another 10 dB when the low order root upon wavefront amplitude, in addition to phase deaberration or in addition to backpropagation and phase deaberration, is used. The improvement comes from the coherent build-up of the target strength by descattering.

TIF is applicable to wavefront compensation on receive in pulse-echo and experiments are currently underway.

## Acknowledgments

## References

[1] M. Moshfeghi and R. C. Waag, "*In Vivo* and *in Vitro* Ultrasound Beam Distortion Measurements of a Large Aperture and a Conventional Aperture Focused Transducer," *Ultras. Med. Biol.*, vol. 5, pp. 415–428, 1988.

[2] G. E. Trahey, P. D. Freiburger, L. F. Nock, and D. C. Sullivan, "*In Vivo* Measurements of Ultrasonic Beam Distortion in the Breast," *Ultrason. Imag.*, vol. 13, pp. 71–90, 1991.

[3] Q. Zhu and B. D. Steinberg, "Modelling and Correction of Incoherent Wavefront Distortion," *International Journal of Imaging Systems and Technology*, Second Issue, 1997.

[4] Q. Zhu and B. D. Steinberg, "Large-Transducer Measurements of Wavefront Distortion in the Female Breast," *Ultrason. Imag.*, vol. 14, pp. 276–299, 1992.

[5] ONR Workshop on Ultrasonic Wavefront Deaberration, In conjunction with 20th International Symposium on Ultrasonic Imaging and Tissue Characterization, June 5–6, 1995, Arlington, VA.

[6] Phase deaberration section, 1996 IEEE Ultrasonics Symposium Proceedings.

[7] S. W. Flax and M. O'Donnell, "Phase Aberration Correction using Signals from Point Reflectors and Diffuse Scatterers: Basic Principles," *IEEE Trans. Ultrason., Ferroelect., Freq. Contr.*, vol. 35(6), pp. 758–767, 1988.

[8] E. H. Attia and B. D. Steinberg, "Self-Cohering Large Antenna Arrays Using the Spatial Correlation Properties of Radar Clutter," *IEEE Trans. Antennas Propagat.*, vol. AP-37(1), pp. 30–38, 1989.

[9] L. Nock, G. E. Trahey, and S. W. Smith, "Phase Aberration Correction in Medical Ultrasound using Speckle Brightness as a Quality Factor," *J. Acoust. Soc. Amer.*, vol. 85(5), 1989.

[10] Q. Zhu, B. D. Steinberg and R. Arenson, "Wavefront amplitude distortion and image sidelobe levels - Part I and II", *IEEE Trans. Ultrason., Ferroelect., Freq. Contr.*, vol. 40(6) pp. 747–762, Nov. 1993.

[11] D.-L. Liu and R. C. Waag, "Correction of Ultrasonic Wavefront Distortion Using Backpropagation and Reference Waveform Method for Time-shift Compensation," *J. Acoust. Soc. Amer.*, vol. 96, pp. 649–660, 1994.

[12] B. D. Steinberg, "Radar Imaging from a Distorted Array: The Radio Camera Algorithm and Experiments," *IEEE Trans. Antennas Propagat.*, vol. AP-29(5), pp. 740–748, 1981.

[13] M. Fink, "Time reversal of ultrasonic fields part I: basic principles," *IEEE Trans. Ultrason., Ferroelect., Freq. Contr.*, vol. 39, pp. 555–566, 1992.

[14] L. M. Hinkelman, D-L. Liu, and R. C. Waag, Q. Zhu, and B.D. Steinberg, "Measurement and Correction of Ultrasonic Pulse Distortion Produced by the Human Breast," *J. Acoust. Soc. Amer.*, vol. 97(3), pp. 1958–1969, 1995.

[15] J. W. Goodman, *Introduction to Fourier Optics*, (McGraw-Hill, New York, 1968.

[16] B. D. Steinberg and H. Subbaram, *Microwave Imaging Techniques*, Chapter 3, New York: Wiley, 1991.

[17] B. D. Steinberg, *Principles of Aperture and Array System Design*, New York: Wiley, 1976.

[18] C. Dorme and M. Fink, "Focusig in transmit-receive mode through inhomogeneous media: The time reversal matched filter approach," *J. Acoust. Soc. Amer.*, vol. 98, pp. 1155–1162, 1995.

[19] Q. Zhu, B. D. Steinberg and R. Arenson, "Correlation Distance of the Female Breast," *J. Acoust. Soc. Amer.*, Aug. 1995.

[20] G. E. Trahey, P. D. Freiburger, L. F. Nock, and D. C. Sullivan "In Vivo Measurements of Ultrasonic Beam Distortion in the Breast," *Ultrason. Imag.*, vol. 13, pp. 71–90, 1991.

[21] P. D. Freiburger, D. C. Sullivan, B. H. LeBlanc, S. W. Smith, and G. E. Trahey, "Two Dimensional Ultrasonic Beam Distortion in the Breast: In vivo measurements and effects," *Ultrason. Imag.*, vol. 14(4), pp. 398–414, 1992.

[22] Q. Zhu and B. D. Steinberg, "Correction of Multipath Interference Using Coherent CLEAN Deconvolution Technique and Spatial Location Diversity," 1995 IEEE Ultrasonics Symposium Proceedings, pp. 1367–1370.

**Qing Zhu** (S'91–M'92–M'93) received the B.S. degree in Applied Mathematics in 1983 from Northern Jiao-Tong University, Beijing, China, the M.S. degree in Biomedical Engineering in 1987 from the Chinese Academy of Medical Sciences, Beijing, China, and the Ph.D degree in bioengineering in August 1992 from the University of Pennsylvania.

She is currently an Assistant Professor of Radiology of the University of Pennsylvania. Her research interests are ultrasonic wave propagation in an inhomogeneous medium, ultrasonic wavefront aberration correction, high-resolution ultrasonic imaging, design of shaped ultrasound transducers, adaptive signal processing, near infrared optical imaging, and acousto-optical interaction.

Dr. Zhu is a member of American Institute of Ultrasound in Medicine, the American Association for the Advancement of Science, and SPIE Biomedical Optics Society.

**Bernard D. Steinberg** (S'48–A'50–A'60–SM'64–F'66–LF'90) received the B.E. and M.S. degrees from the Massachusetts Institute of Technology, Cambridge, MA, and the Ph.D. degree from the University of Pennsylvania, Philadelphia, PA, all in electrical engineering.

He is a Professor of Electrical Engineering and Director of the Valley Forge Research Center, University of Pennsylvania. The two primary research topics of the laboratory are high resolution microwave imaging based upon adaptive self-calibration of huge, distorted antenna arrays and high resolution medical ultrasound imaging in inhomogeneous and refractive media. The arrays may be real, synthetic, or combinations of both. He is the author of two books in this field, *Principles of Aperture and Array System Design: Including Random and Adaptive Arrays* (Wiley, 1976), and *Microwave Imaging with Large Antenna Arrays: Radio Camera Principles and Techniques* (Wiley, 1983), and co-author of *Microwave Imaging Techniques* (Wiley, 1991).

He was Co-founder and Vice President of Research and Engineering of General Atronics Corporation, Wyndmoor, PA, and Co-founder and Chairman Emeritus of Interspec, Inc., Ambler, PA, a company specializing in ulrasonic imaging equipment for cardiologists.

Dr. Steinberg is a Life Fellow of the IEEE, a member of URSI, Commission B (Fields and Waves), Sigma Xi, and AAAS, and has served as Distinguished Lecturer of the IEEE Antennas and Propagation Society.

# COUPLING ULTRASOUND AND LIGHT METHODS TO INCREASE DETECTION SENSITIVITY AND SPECIFICITY OF ULTRASOUND

Quing Zhu[a], Member IEEE, Britton Chance[b], Daniel Sullivan[a], Tim Dambro[a]
[a]Radiology Department
[b]Biochemistry and Biophysics Department
University of Pennsylvania
Philadelphia, PA 19104

**Abstract** —— The objective of this research is to investigate the potential use of combining near infrared (NIR) diffuse light and ultrasound methods to increase the detection sensitivity and specificity of small breast lesions by conventional ultrasound. A novel imaging system which combines these two methods has been introduced. A NIR phased array positioner capable of providing the line-of-sight to a small target in a scattering medium is incorporated into an ultrasound imaging system. This combined system has been tested using models consisting of a single emulated tumor of a few mm size buried in a scattering phantom. In each test, the combined system was mechanically translated to scan for the small object. At each scanning position, optical amplitude and phase data and an ultrasound image were acquired. The object line-of-sight information was coded into ultrasound images after scanning. Ultrasound images without and with line-of-sight information were graded on a five-point scale by two radiologists. Receiver-Operator Characteristic (ROC) curves of ultrasound and combined methods were measured. ROC curves of the combined method were much higher than ultrasound alone. Average areas under ROC curves of ultrasound alone and combined method were 51.7% and 82.5%, respectively. This difference in area is statistically significant ($p < 0.05$). In conclusion, the combined method affords a significant improvement in detection sensitivity and specificity compared with conventional ultrasound in this phantom study.

# I. INTRODUCTION

Ultrasound is frequently used in conjunction with mammography to differentiate simple cysts from solid lesions. When all criteria for a simple cyst are strictly adhered to, the accuracy of ultrasound is 96%-100% [1]. However, results with respect to early detection of small solid lesions remain disappointing [2]. Ultrasound sensitivity in the detection of palpable solid masses less than 2 cm in size is 71% which is about 10% less than the sensitivity of physical examination [3]. The sensitivity in the detection of small invasive lobular carcinomas (<1 cm) is only 25% [4]. Ultrasound specificity is low due to the considerable overlap of benign and malignant lesion characteristics [5-6]. This may be caused by the fact that even when tissues are pathologically different, their ultrasound properties may be quite similar [7].

Medical Optical Imaging and Spectroscopy is a rapidly advancing field [8]. The emphasis is on diffusion waves in the near infrared (NIR) region: essentially 750 to 850 nm are required where a window of the lowest tissue absorption permits the penetration of light through the necessary 10-20 cm of a large human breast [9]. NIR light is expected to have high sensitivity and specificity because certain characteristics differ in tumors and normal breast tissue: 1) The amount of blood needed to serve the tumor's metabolic needs is increased over that of normal background tissue; 2) Hemoglobin desaturation in tumors is increased due to the high oxygen demand of cancers; 3) Light scattering properties of the tumor are expected to be enhanced due to the increased mitochondria population with respect to the background of normal cells [10]; 4) The angiogenesis phenomenon [11] allows tumor identification by observing the delivery of contrast agents, such as the well-characterized NIR absorber indocyanine green (ICG), through the permeable vascular beds to the extravascular space surrounding the tumor. The intense absorption band of ICG at 800 nm affords a high contrast of the tumor extravascular space as compared with the background capillary network of the normal tissue. In addition, ICG has an interesting

2

# COUPLING ULTRASOUND AND LIGHT METHODS TO INCREASE DETECTION SENSITIVITY AND SPECIFICITY OF ULTRASOUND

Quing Zhu[a], Member IEEE, Britton Chance[b], Daniel Sullivan[a], Tim Dambro[a]

[a]Radiology Department

[b]Biochemistry and Biophysics Department

University of Pennsylvania

Philadelphia, PA 19104

**Abstract** —— The objective of this research is to investigate the potential use of combining near infrared (NIR) diffuse light and ultrasound methods to increase the detection sensitivity and specificity of small breast lesions by conventional ultrasound. A novel imaging system which combines these two methods has been introduced. A NIR phased array positioner capable of providing the line-of-sight to a small target in a scattering medium is incorporated into an ultrasound imaging system. This combined system has been tested using models consisting of a single emulated tumor of a few mm size buried in a scattering phantom. In each test, the combined system was mechanically translated to scan for the small object. At each scanning position, optical amplitude and phase data and an ultrasound image were acquired. The object line-of-sight information was coded into ultrasound images after scanning. Ultrasound images without and with line-of-sight information were graded on a five-point scale by two radiologists. Receiver-Operator Characteristic (ROC) curves of ultrasound and combined methods were measured. ROC curves of the combined method were much higher than ultrasound alone. Average areas under ROC curves of ultrasound alone and combined method were 51.7% and 82.5%, respectively. This difference in area is statistically significant ($p < 0.05$). In conclusion, the combined method affords a significant improvement in detection sensitivity and specificity compared with conventional ultrasound in this phantom study.

# I. INTRODUCTION

Ultrasound is frequently used in conjunction with mammography to differentiate simple cysts from solid lesions. When all criteria for a simple cyst are strictly adhered to, the accuracy of ultrasound is 96%-100% [1]. However, results with respect to early detection of small solid lesions remain disappointing [2]. Ultrasound sensitivity in the detection of palpable solid masses less than 2 cm in size is 71% which is about 10% less than the sensitivity of physical examination [3]. The sensitivity in the detection of small invasive lobular carcinomas (<1 cm) is only 25% [4]. Ultrasound specificity is low due to the considerable overlap of benign and malignant lesion characteristics [5-6]. This may be caused by the fact that even when tissues are pathologically different, their ultrasound properties may be quite similar [7].

Medical Optical Imaging and Spectroscopy is a rapidly advancing field [8]. The emphasis is on diffusion waves in the near infrared (NIR) region: essentially 750 to 850 nm are required where a window of the lowest tissue absorption permits the penetration of light through the necessary 10-20 cm of a large human breast [9]. NIR light is expected to have high sensitivity and specificity because certain characteristics differ in tumors and normal breast tissue: 1) The amount of blood needed to serve the tumor's metabolic needs is increased over that of normal background tissue; 2) Hemoglobin desaturation in tumors is increased due to the high oxygen demand of cancers; 3) Light scattering properties of the tumor are expected to be enhanced due to the increased mitochondria population with respect to the background of normal cells [10]; 4) The angiogenesis phenomenon [11] allows tumor identification by observing the delivery of contrast agents, such as the well-characterized NIR absorber indocyanine green (ICG), through the permeable vascular beds to the extravascular space surrounding the tumor. The intense absorption band of ICG at 800 nm affords a high contrast of the tumor extravascular space as compared with the background capillary network of the normal tissue. In addition, ICG has an interesting

2

redshifted fluorescence property [12]. It absorbs radiation at the source wavelength of 780 nm and reradiates photons at 830 nm. In this process, the tumor extravascular space is converted into a source of secondary diffuse waves with reduced background. Finally, the contrast agents could be linked to tumor-specific antibodies or to specific sites in the tumor such as their mitochondria membranes.

A simple optical phased array system (OPAS) for object positioning has been constructed [13] that measures the interference of intensity-modulated diffuse light signals at detector positions equidistant from two spatially separated sources. In the absence of heterogeneities (Fig.1. a) the signals will cancel, and the null plane or line is always at the bisecting plane or line and the deviation between null and biosecting lines is zero. If a hidden absorber is present in the medium (Fig.1b), the balance of the sources on the bisecting line is perturbed and the null line will deviate from it. This deviation, depending on the relative positions of the sources and the absorber, is used as an indicator in the scanner to detect an inhomogeneous object with respect to the background. The line-of-sight of the absorber is obtained from this newly formed null line through scanning. This type of "pointing" device affords highly sensitive localization of a few mm diameter tube obscured deep within a highly scattering material to an accuracy of better than $1^o$. *In vivo* experiments have demonstrated clear-cut amplitude nulls and sharp phase transitions [13],[34]. Complete information about object shapes and optical properties requires time-consuming tomographic approaches to data acquisition and inversion [14-15]. Because of the diffuse nature of light propagation in human tissue, high resolution optical images are intrinsically difficult to obtain. The NIR light is strongly scattered by human tissues. Typical reconstructions can distinguish simple structures of approximately 1 cm in size; sharp edges are typically blurred by a few millimeters [7].

Ultrasound, on the other hand, has real time imaging capability and the imaging capability of ultrasound equipment has been steadily improving. More recently, the result reported by Stavros et al. is very encouraging [16]. Although no lesion size was documented in [16], of 125 malignant lesions, 123 were correctly classified as intermediate or malignant (98.4% sensitivity). Coupling OPSA into an ultrasound system will increase ultrasound detection sensitivity and specificity while maintaining ultrasound real time imaging capability and resolution. Furthermore, the combined system is low cost and efficacious, which meets the challenges of health care reform.

## II. BASIC PRINCIPLES

The principle of object detection by OPAS is described briefly below. The density of photons at position r of *intensity-modulated light*, U(r), traveling in an infinitely-large homogeneous scattering medium can be described by diffusion theory and expressed in the frequency-domain as [17]

$$U(r) = \frac{1}{4\pi v D r} e^{-kr} \tag{1}$$

where $D = \dfrac{1}{3(\mu_a + \mu_s')}$, $k = \sqrt{\dfrac{\mu_a - i\omega/v}{D}}$ ,

D is the diffusion coefficient, $\mu_a$ and $\mu_s'$ are absorption and reduced scattering coefficients, $v$ is the speed of light in the medium, and $\omega$ is the modulation frequency of the light source. Since k is a complex number, Eq.1 can be rewritten as

$$U(r) = \frac{1}{4\pi v D r} e^{-k_r r} e^{-ik_i r} \tag{2}$$

where $k_i r$ corresponds to a phase shift produced by traveling in the scattering medium with respect to the source.

A phased array system consists of one in-phase (i.e. initial phase=0°) and one out-phase source (i.e. initial phase=180°) as shown in Fig. 2. The total photon density at position r is

$$U(r) = \frac{1}{4\pi vD}[\frac{1}{r_1}e^{-k_r r_1}e^{-ik_i r_1} + \frac{1}{r_2}e^{-k_r r_2}e^{-i(k_i r_2 + 180^o)}]$$  (3)

where r, $r_1$, and $r_2$ are related by $r_1 = \sqrt{r^2 + a^2 - 2ra\cos(\theta)}$ and $r_2 = \sqrt{r^2 + a^2 + 2ra\cos(\theta)}$. In this case, the intensities for the two in-phase and out-phase sources are assumed the same, and the separation between the two sources is 2a. Eq. 3 indicates that the photon density at the bisecting line of the array, i.e. $r_1=r_2$, is equal to zero due to the cancellation of the two sources; the phase shift relative to the extremes of $0^o$ an $180^o$ is expected to be $90^o$ and the amplitude is theoretically zero but practically determined by the system noise. When a small heterogeneity is present in the medium, the balance of the sources on the bisecting line will be destroyed and the null line will bias toward the object. The object line-of-sight is obtained from the newly formed null line through scanning.

## III. METHODS

A. Experimental set-up

Mechanical assembly of the optically guided ultrasound system is shown in Fig.3. A coaxial probe is assembled by mounting two laser diode sources (in- and out-phase sources) and an ultrasound transducer on a plastic holder. A Photo-Multiplier Tube (PMT) optical detector is mounted on the opposite side of the coaxial probe. The separation of the source and the detector can be changed from several cms to 15 cm depending on the size of a testing phantom. The coaxial probe and optical detector assembly is translated laterally by a stepping motor in the X direction to scan an object. The coupling between the coaxial probe and a scattering phantom described later was made using the standard ultrasound coupling gel. In a typical experiment, the step size used is 1 mm. The optical wavelength is 780 nm and the modulation frequency is 5 KHz. The ultrasound probe is a 64-element phased array operating at 5 MHz center frequency and the ultrasound system used is a GE RT 3600 commercial scanner located at the Angiography Section of the Radiology

Department. The focal depth of the scanner can be changed from 1 cm to 4 cm and we used 4 cm in all experiments.

## B. Data acquisition

The detailed description of OPSA can be found in Ref. [18] and data acquisition is described here. The optical amplitude and phase data at each lateral position were acquired through a 12 bit A/D converter (AD 2210, Real Time Devices, Inc) and stored on a PC. The ultrasound B-scan image at each lateral position was captured using a video board (ComputerEyes/RT, Digital Vision, Inc). The resolution of the image grabber is 200 x 320 with 8 bit 256 gray levels.

## C. Scattering phantom

A scattering phantom was made of an acrylamide gel (Boehringer Mannheim Biochemicals Corporation) which is typically used as an electrophophresis gel for DNA studies and is also used to construct ultrasound phantoms [19-20] . Scattering particles at optical and ultrasound wavelength scales were added to the acrylamide solution before the gel was formed. First, the premixed acrylamide and bis-acrylamide powder was dissolved in distilled and degassed water. 20% concentration of Intralipid (Kabi Pharmatica) was added to the acrylamide solution to dilute the solution to a 0.5% intralipid concentration. The optical scattering parameter $\mu s$ at this concentration closely matches $\mu s$ of human tissue. Second, scattering particles made of glass spheres (Jenson Scientific) were added to the solution. The mean diameters of the spheres were 112, 150 and 205 $\mu m$ and the estimated particle density based on the calculation given in [21] should produce Rayleigh amplitude distribution. In order to produce polymerization, components of ammonium persulfate and tetramethylethylenediamine (known as TEMED) were added. The outer dimensions of the scattering phantom were 7.5 cm x 12 cm x 14 cm.

Objects of several mm sizes were inserted in the scattering phantom during experiments.

D. Experimental procedure

Since we are to compare the two detection methods, ultrasound alone and ultrasound-light, it is necessary to select a metric for comparison. Receiver-Operator Characteristic (ROC) curves are commonly used to depict figures of merit for clinical methods of detecting lesions or differentiating among diseases [22-23]. Each ROC curve indicates the trade-offs between sensitivity and specificity that are available from a diagnostic method, and thus describes the inherent discrimination capacity of that method. A higher ROC curve would indicate greater discrimination capacity, because a larger value of sensitivity at each value of false-positive-fraction (FPF = 1-specificity) or, equivalently, a smaller value of FPF at each sensitivity, can be achieved on a higher curve if an appropriate confidence threshold is used. Similarly, a lower ROC curve would indicate less discrimination capacity.

Three different experimental approaches can be used to measure ROC curves, namely, yes-no, rating and forced choice methods [24]. The rating method is more efficient and is almost always used in practice [23]. In this approach the observer is required to select one of several categories of confidence, usually represented by numerical ratings, to report his impression of the likelihood that lesions or targets are present or absent. These categories can be given qualitative labels such as (1) definitely or almost definitely absent, (2) probably absent, (3) may be present, (4) probably present, and (5) definitely or almost definitely present. It is not necessary for different observers to interpret these category labels in the same way; the essential requirement is that the labels provide an unambiguously ordered set of categories for each observer's relative confidence

7

in the two states of truth. We have adapted the rating method to measure ROC curves of ultrasound and ultrasound-light methods.

It is well known that weak targets in a sequence of images are more readily detected than in a single image. Thus triple images taken in 1 mm steps at the neighborhood of the optical phase transition and amplitude null were selected in each test. The criteria of triple image selection are: (1) identify the minimum point of the amplitude null from the optical amplitude curve, or in the case that the minimum is not unique, choose the point which is closest to $90^o$ from the optical phase transition curve; (2) select the corresponding ultrasound image at the same lateral position as the second image in the triple; (3) select images taken 1 mm left and right of the second image as the first and third images in the triple. Since the optical assembly and ultrasound probe are coaxially mounted, the object in the triple images always appears along the ultrasound scan axis. To avoid giving any prior knowledge to human observers about the object location, we chose different image windows in different tests to randomize the object location. In each test, the image windows used for triple images were the same and the object position shift was caused by the 1 mm lateral translation of the imaging system.

All triple images without and with optical information were evaluated by 2 experienced radiologists in the Breast Imaging Section of the Radiology Department using the evaluation form shown in Table I. They were informed that the images were obtained at slightly different lateral positions (1mm) and that they could mentally average these images to filter out artifacts and noise. For ultrasound-alone images, the observers were told that they should look for possible lesions or targets in the entire image. For the images coded with optical line-of-sight information, the observers were instructed to look for possible lesions or targets in the neighborhood along the line-of-sight direction. Observers were also told that targets might be hypoechoic or hyperechoic. Triple images with no

lesion or target present were also presented to observers during the trials. The positive and negative sets of images were presented to observers in random order.

## IV. RESULTS

Fig.4 shows optical amplitude and phase responses when concentric black-plastic tubes of 1.9 and 1.7 mm diameters filled with 0.5% intralipid were inserted into the scattering phantom at approximately 6 cm cm depth. The testing object is an optical absorber which also generates an inhomogeneous ultrasound echotexture, as some tumors may do, as shown in Fig.5. The sharp phase transition and amplitude null correspond to the object line-of-sight. Three ultrasound images taken at phase transition and amplitude null positions (16, 17, 18 mm) are shown in Fig.5. The image of the object, indicated by an arrow, is highly obscured by speckle noise. However, one observer picked up the target and marked category 4 on the evaluation form. When the same images coded with optical line-of-sight information, shown by dashed lines in Fig.6, were presented to the observer, his detection confidence increased from category 4 to 5. Another observer completely missed the target in ultrasound-alone images and marked category 1 on the form. When the images with object line-of sight information were presented, the observer picked up the target and selected category 3 on the form. This example shows the improvement in detection sensitivity when the combined method is used.

Figs.7-9 show another example. A 4.5 mm white Teflon bar was inserted into the scattering phantom and was imaged using the combined system. The testing object is an optical scatterer which generates a slightly hyperechoic echotexture as shown in Fig.8. The optical amplitude and phase responses are shown in Fig.7. The triple images taken at the neighborhood of optical phase transition and amplitude null (20, 21, 22 mm) are shown in Fig.8 with the object indicated by an arrow (upper one) in the images. One observer missed the target entirely and marked category 1 on the evaluation form. When the images

with object line-of-sight (Fig.9) were presented, the observer identified the target and circled category 3 on the form. Another observer missed the target completely and selected an artifact, pointed by an arrow (lower one), and circled category 4 on the form. Once the images with object line-of-sight were presented, the observer identified the target and circled category 3 on the form. This example shows the combined method can significantly improve detection sensitivity and specificity of ultrasound.

We have studied a total of 30 positive trials and 21 negative trials. In the positive trials, the testing objects used are black Delrin rods, black rubber sticks of different stiffness, black plastic tubes or concentric tubes filled with 2.5µg/ml ICG or 5% intralipid, and white Teflon rods. The sizes of the testing objects range from 1.6 mm to 8.2 mm, and the average is 3.64 mm with 1.97 mm standard deviation. In the case of non cylindrical object, geometric mean is used in the calculation. These testing objects are either optical absorbers or scatterers which emulate to a large extent tumor optical properties. The acoustics reflectivity of these materials varies from hyperechoic, heterogeneous to slightly hypoechoic. In the negative trials, images of the scattering phantom obtained at three consecutive lateral positions in 1 mm steps were presented. ROC data of positive and negative trials of two independent readings obtained from the two observers were shown in Table II and III. The first section, consisting of the first row of the table, lists the 5 categories used in the evaluation. The second section shows four quantities based on positive trials; and the third shows the corresponding quantities based on negative trials. The first row in section (2) shows the frequency of the occurrence of the correct target identification and the use of the corresponding category when the ultrasound method is used. The second row is the sensitivity or conditional probability (P(T/t)) of the observer responding target T at the correct location when target t at that location was present. The third and fourth rows are the same quantities as the first two but the method used is ultrasound-light. The first row in section (3) shows the frequency of the occurrence of

false positives and the use of the corresponding category when the ultrasound method is used. The second row is 1-specificity or condition probability ($P(T/n)$) of the observer responding target T when no target was present. The third and fourth rows are the same quantities when the ultrasound-light method is used.

The calculation of $P(T/t)$ using both methods is strictly forward when the observer identified the correct target or did not detect any target during positive trials. But there were cases in positive trials in which the observer picked up artifacts instead of the correct target. The locations of artifacts could be anywhere when ultrasound is used, but they are constrained along the object line-of sight when ultrasound-light is used. For these cases, we classified them into category 1 in positive trials, because with regard to the correct target the observer reported no target present. Since these cases correspond to false positives, we added them to the 21 negative trials. Thus the total negative trials of observer 1 in first reading is 29 and second reading is 32, and observer 2 in first reading is 33 and second reading is 34. For the total 21 negative trials, optical data did not shown any phase transitions and amplitude nulls. Therefore, these trials were classified as category 1 under the ultrasound-light method.

Average empirical ROC curves of ultrasound (solid) and ultrasound-light (dashed) of the two independent readings for the two observers are shown in Fig.10. The superior performance of ultrasound-light is shown by the higher ROC curves. The fact that ultrasound ROC curves are close to the major diagonal indicates that the detection information is very poor in this phantom study and that targets can only be recognized at a slightly better than chance level. The area under the ROC curve provides a measure of discriminatory efficacy: an area of 100% denotes an ideal system and 50% denotes an ineffective system. The calculated areas under ROC curves of ultrasound and ultrasound-light of observer #1 are 53.9% and 79.2%, and of observer #2 are 49.5% and 85.8%. The

mean values are 51.7% for ultrasound and 82.5% for ultrasound-light, respectively. Following the statistical test procedure given in [33], the difference in area between the two methods is statistically significant (p<0.05, see Appendix for detail).

In the human observer study, each observer performed two independent readings with positive trials presented in slightly different orders. In the first reading, each positive trial was evaluated in the order of ultrasound and ultrasound-light instead of random. This procedure took less time for the observers because they were already familiar with ultrasound images before the same images with optical line-of-sight were presented. In the cases that the observers detected targets along the line-of-sight with ultrasound, this procedure might have some psychological effect on the category they chose with ultrasound-light because they might still remember the category they selected with ultrasound method. To test this effect, we presented ultrasound and ultrasound-light images as well as negative images to the two observers in random order at the second independent reading. The ROC data obtained from the two readings for the two observers were given in Tables II and III and the corresponding ROC curves for the two observers are shown in Fig.11. Procedure #1 (first reading) is the ordered test with ultrasound and ultrasound-light images presented in sequence while procedure #2 (second reading) is the random test with ultrasound and ultrasound-light images presented in random order. The results with both testing procedures are consistent which indicate that the observers are based on their own evaluation criteria and are not influenced by the ways that the images are presented. The areas under the ROC curves of procedures #1 and #2 for observer 1 are 57.3% and 50.9% for ultrasound alone and 78.2% and 80.2% for ultrasound-light, while the areas for observer 2 are 44.6% and 50.0% for ultrasound alone and 85.8% and 85.8% for ultrasound-light. The fact that the difference between ultrasound ROC curves measured with the two procedures is larger than the difference between ultrasound-light ROC curves

measured with the two procedures for both observers reflects the chance performance characteristic of ultrasound in this study.

## V. DISCUSSION

The model studies described in the paper have been designed to assess the influence of adding object line-of-sight information upon detection by human observers. The small objects used in the studies are optical anomalies with acoustic reflectivity varying from hyperechoic, heterogeneous to slightly hypoechoic. These anomalies emulate to a large extent tumor optical properties and to some extent tumor acoustic properties (inhomogeneous echogenicity and slightly hypoechoic cases). However, these anomalies as well as the scattering phantom in which they are embedded are obviously inadequate to reproduce all the properties of breast tissue. Clinical studies are planned to further evaluate the combined imaging system.

The ultrasound scanner used for this study is not a state-of-the-art breast scanner, but it is the one available full-time to us for these experiments in the research laboratory. However, the relative improvements in detection sensitivity and specificity when the optical information is added are independent from the scanner *quality* used because the ROC comparisons of ultrasound alone and ultrasound-light are based on a pair of triple images obtained from the same imagery. With a better scanner, we should be able to get similar improvements as reported in this paper with reduced average object size.

In the ultrasound-light image display, the optical null line was simply coded into the corresponding ultrasound images by a dashed line. This display method is simple but it does not use optical information related to the mass of the object. For example, a large mass with higher optical absorption and scattering will produce a sharper phase transition and deeper amplitude null compared with a small mass. In our future studies, we need to

13

code optical phase gradient information with a gray scale bar into ultrasound images. A higher gray level (large gradient) may suggest that observers look for a larger object and a lower gray level (small gradient) may suggest that observers search for a smaller object in a larger area. However, the approximate relation between tissue mass sizes and optical properties needs to be investigated.

To estimate the sensitivity of OPAS, we measured depths of amplitude nulls and spatial intervals of phase transitions for all positive trials. The depth of the amplitude is defined as the difference in dB between the peak and the null in an amplitude profile. Since the two peaks on each side of a null were not exactly the same (See Fig.4a), we used smaller peaks in all cases. The spatial interval of the phase transition was the interval where a phase curve rose from one stable value and settled down at another stable value (See Fig.4b). The two stable values were obtained by averaging 5 to 10 points on each side away from the phase transition. If we denote the difference between the two stable values as D, the spatial interval of the phase transition is quantitatively defined as the difference between the two spatial points where a phase curve exceeds 10%D and reaches 90%D. The measured average depth of amplitude is 8.93 dB (std. 4.58 dB) and the average spatial interval of phase transition is 4.78 mm (std. 1.85 mm) which is about 1 mm larger than the average size of testing objects.

The system noise can cause pointing error by shifting the null line of OPAS. However, as long as the null line is confined in the average transition region, the ultrasound detection would not be affected. For example, if the null line were shifted to the edge of the phase-transition interval (2.39 mm), the pixel shift from the center of the target in the image were only 6 points at the typical 60 mm depth studied. As a matter of fact, the observers had the tendency to search and circle a larger area alone the line-of-sight than the true object size on the image

The resolving power of 2 objects by OPAS is very low and the object separation must be as large as 1 cm [18]. When the object separation is less than approximately 1 cm, OPAS will point to the center of mass of the objects. For this reason, the combined system is optimal for the localization and imaging of an isolated small tumor in the breast. Several clinical studies have been devoted to the determination of multicentric occurrence of breast cancers [25]. McDivitt [26] critically reviewed these data and concluded that the incidence of invasive foci in areas of multicentric cancers was 5-10%. For these cases, the optical amplitude and phase responses may show multiple peaks and the locations of these peaks may also be used as references to determine the centers of the anomalies.

The combined system has been implemented by mechanically translating an ultrasound phased array with OPAS. This choice accommodates the current set-up of OPAS. The optical null line can be electronically steered by varying the amplitude modulation of the two sources [18]. However, scanning parameters, such as sensitivity to off-line object, field of view vs. source separation, etc., need to be studied before the OPAS scan mode can be used. This is a topic for future study.

With current one-dimensional implementation of the combined system, false positives happen along the object line-of-sight. With another OPAS deployed from a different direction than the combined probe, the object position can be located from the intersection of two lines of sight. Therefore, the false positive rate with the combined method can be reduced significantly.

Transmission mode of OPAS is used in our current system set-up. Reflection mode is also possible where a detector is placed at the middle of two laser diode sources [18]. This deployment requires overlapping geometry of an ultrasound array and the light

detector, and can be done by coupling the detector through the ultrasound array with a small light guide. Note that light guides can be quite small, i.e., on the order of 100 micro optical fibers. The penetration depth of reflection mode is about half that of transmission mode, and it is not a problem for most breasts under soft compression when a patient is in a supine position.

There are several possible applications of the combined method. First, the combined method may allow real time implementation of current ultrasonic wavefront compensation algorithms. The female breast and abdominal wall are acoustically inhomogeneous and that limits the ultrasound resolution. Ultrasonic wavefront compensation algorithms adaptively adjust time delays [27-29] and amplitude variations [30-31] of RF signals received from different array elements to compensate tissue induced distortion and therefore to improve spatial and contrast resolution. But, these algorithms require off-line processing because of extensive computations involved. With the combined method, the compensation can be implemented in real time when the need for correction is confined to the neighborhood of object line-of-sight. Second, OPAS combined with low-frequency ultrasound could be used to detect and monitor a small aneurysm or hemorrhage in the brain. Although the optical method alone is able to detect and monitor an anomaly in the brain [32], the size and shape information provided a combined ultrasound-light system would provide valuable information to guide surgery and treatment.

## VI. SUMMARY

A novel imaging method which combines ultrasound and near infrared diffuse light has been introduced in this paper. The combined method utilizes object line-of-sight information provided by a highly sensitive optical positioner to confine human observers along the object direction to search for possible lesions or targets in ultrasound images. As

a result, the detection sensitivity and specificity of a small target of a few mm size have been improved significantly over the conventional ultrasound. The average areas under ROC curves from 2 radiologists are much higher for the combined method (82.5%) than for ultrasound alone (51.7%). Thus the combined method affords a significant improvement in detection sensitivity and specificity compared with conventional ultrasound.

## APPENDIX

We have adapted the approach given in [33] to determine the statistical significance of the difference in average areas measured with ultrasound and ultrasound-light methods. In the approach, the statistic power is calculated via $Z_\beta$ given by

$$Z_\beta = \frac{\sqrt{n}\delta - Z_\alpha\sqrt{2V_1}}{\sqrt{V_1 + V_2}} \tag{4}$$

where $Z_\alpha = 1.645$, for a 5% one-sided test of significance, $\delta = \theta_2 - \theta_1$, is the difference between areas measured with the two methods, $n$ is the sample size used, $V_1 = \frac{\theta_1}{2 - \theta_1} + \frac{2\theta_1^2}{(1 + \theta_1)} - 2\theta_1^2$ and $V_2 = \frac{\theta_2}{2 - \theta_2} + \frac{2\theta_2^2}{(1 + \theta_2)} - 2\theta_2^2$. $Z_\beta = 0.84, 1.28, 1.645$ for 80%, 90% or 95% statistic power.

Taking the averages $\theta_1 = 51.7\%$ and $\theta_2 = 82.5\%$ measured with ultrasound and ultrasound-light methods, $\delta = 0.308$, $V_1 = 0.166$ and $V_2 = 0.087$. With $n = 30$, $Z_\beta$ is 1.469. Therefore, greater than 90% statistic power has been achieved, i.e., we have a high assurance (>90% probability) that the test of significance on samples would yield a statistically significant difference (p<0.05).

## References

[1] Sickles EA, "Detection and Diagnosis of breast cancer with mammography," Perspect Radiology, 1988; 1:36-65.

[2] Jackson V, "The role of US in breast imaging, Radiology 1990; 177: 305-311.

[3] Dam PAV, Goethem MLAV, Kersschot E, Vervliet JV, et al., "Palpable Solid Breast Masses: Retrospective Single-and Multimodality Evaluation of 201 Lesions," Radiology 1988; 166:435-439.

[4] Paramagul C, Helvie MA, Adler DD,"Invasive Lobular Carcinoma: Sonographic Appearance and Role of Sonography in Improving Diagnostic Sensitivity, Radiology 231-234, 1995.

[5] Sickles EA, Filly RA, Callen PW, "Benign breast lesions:ultrasound detection and diagnosis, "Radiology 1984; 151:467-470.

[6] Kopans DB, Meyer JE, Lindfors KK, "Whole-breast US imaging:four-year follow-up." Radiology 1985; 157:505-507.

[7] Goldberg BB, Liu JB, Forsberg F: Ultrasound Contrast agents: A review. Ultrasound Med Biol 20:319, 1994.

[8] Yodh A and Chance B,"Spectroscopy and imaging with diffusing light," Physics Today, March 1995.

[9] Wilson BC, Optical Properties of Tissue, Encyclopedia of Human Biology," Volume 5, Academic Press, Inc. 1991.

[10] Beauvoit B, Evans S, Jenkin T.W, Miller EE, Chance B,"Correlation between light scattering and the Mitochondrial Content of Normal Tissues and Transplantable Rodent Tissues," Anal. Biochem., in press. 1995.

[11] Flakman J," Introduction: angiogensis and cancer," Cancer Biology 1992; 3:47-71.

[12] O'Leary M. A, Boas D A, Chance B and Yodh AG,"Reradiation and Imaging of Diffuse Photon Density Waves Using Fluorescent Inhomogeneities," Journal of Luminescence, Vol. 60-61, PP. 281-286, 1994.

[13] Chance B, Kang K, He L, Weng J, and Sevick E,"Highly sensitive object location in tissue models with linear in-phase and anti-phase multi-element optical arrays in one and two dimensions," Proc. NAtl. Acad. Sci. , vol. 90, pp. 3423-3427, April 1993, Medical Science.

[14] Arridge AR, Schweiger M, Delpy DT, "Iterative reconstruction of near infrared absorption images", in Inverse Problems in Scattering and Imaging, SPIE 1992, V1767:372.

[15] Graber HL, Chang J, Lubowsky J, Aronson R, Barbour R L, "Near-infrared absorption imaging of dense scattering media by steady-state diffusion tomography", in Photon Migration and Imaging in Random Media and Tissues, SPIE 1993, V1888:372.

[16] Stavros TA, Thickman D, Rapp C, "Solid breast nodules: Use of sonography to distinguish between benign and malignant lesions," Radiology 1995; 196: 123-134.

[17] Fishkin JB and Gratton E,"Propagation of photon-density waves in strongly scattering media containing an absorbing semi-infinite plane Bounded by a straight edge," J. Opt. Soc. Am. A 10, 127-140 (1993).

[18] Chance B, Kang K, He L, Liu H and Zhou S,"Precision Location of Hidden Absorbers with Phased-Array Optical Systems, " Rev. Sci. Instru. In press.

[19] Weng L, Ph.D Dissertation, Dept. of Biomedical Engineering and Science Institute, Drexel University, PA, 1990.

[20] Molthen RC, Ph.D Dissertation, Dept. of Biomedical Engineering and Science Institute, Drexel University, PA, 1996.

[21] Sleefe GE, and Lele P, "Tissue Characterization based on scatterer number density estimation," IEEE IEEE Trans. Ultrason. Ferroelec. Freq. Contr., vol 35, No.6., November.

[22] Metz CE., "ROC methodology in radiologic imaging, "Invest. Radiol., vol 21, pp. 720-733.

[23] Swets JA, "ROC analysis applied to the evaluation of medical imagery techniques," Invest. Radiol., vol. 14, pp. 109-121, 1979.

[25] Page DL and Anderson TJ, "Diagnostic Histopathology of the Breast, Chapter 16," 1987.
[26] McDivitt RW 1984 "Breast Cancer Multicententricity in McDivitt RW, Obermann HA, Ozzello L, Kaufman N (eds) The breast. Williams and Wilkins, Baltimore, p 139-148.

[27] Flax, S W and O'Donnell M. "Phase Aberration Correction using Signals from Point Reflectors and Diffuse Scatterers: Basic Principles," IEEE Trans. Ultrason. Ferroelec. Freq. Cont., 35(6):758-767, Nov. 1988.

[28] Nock L., Trahey GE, and Smith SW., "Phase Aberration Correction in Medical Ultrasound Using Speckle Brightness as a Quality Factor," J. Acoust. Soc. Am., 85(5) 1819-1833 (1989).

[29] Liu D-L and Waag RC., "Correction of Ultrasonic Wavefront Distortion Using Backpropagation and Reference Waveform Method for Time-shift Compensation," J. Acoust. Soc. Am. 96, 649-660 (1994).

[30] Zhu Q and Steinberg BD, "Modeling and Correction of Incoherent Wavefront Distortion," Special Issue of International Journal of Imaging Systems and Technology, Second issue 1997.

[31] Zhu Q and Steinberg BD, "Deaberration of Incoherent Wavefront Distortion: A Toward Inverse Filtering Approach," IEEE Trans. Ultrason. Ferroelec. Freq. Cont., in press, 1997.

[32] Gopinath SP., Robertson CS., Contant, CF, Narayan, R. K. Grossman, R. G. and Chance B, "Early Detection of Delayed Traumatic Intracranial Hematomas using Near Infrared Spectroscopy," J. Neurosurgery, 83:438-444.

[33]  Hanley JA and McNeil BJ, "The Meaning and Use of the Area under a Receiver Operating Characteristic (ROC) Curve," Diagnostic Radiology, 143: 29:36, 1982.

[34] Zhou SM, Xie CH, Nioko S, Liu HL and Chance B,  "Phased Array Instrumentation Appropriate to High-Precision Detection and Localization of Breast Tumor," SPIE Proceeding, 1997.

# TABLES

## Table I. Evaluation form

Please check for possible lesions or targets.

Target #1
1. No lesion or target present
2. Probably no lesion or target present
3. Lesion or target may be present
4. Lesion or target probably present
5. Lesion or target definitely present

Target #2
1. No lesion or target present
2. Probably no lesion or target present
3. Lesion or target may be present
4. Lesion or target probably present
5. Lesion or target definitely present
Target #3...
Target #4...

Lesions or targets may be hyperechogenic or hypoechogenic. If you identify any lesions please circle and number them on images.

Table II ROC data of observer #1(First Reading)
A total of 30 positive trails and 29 negative trails

| Section(1) | Category | 1 | 2 | 3 | 4 | 5 |
|---|---|---|---|---|---|---|
| Section(2) | | | | | | |
| US: | Occurrence | 16 | 3 | 5 | 3 | 3 |
| | P(T/t) | 1 | 0.467 | 0.367 | 0.200 | 0.100 |
| US-Light: | Occurrence | 8 | 2 | 6 | 9 | 5 |
| | P(T/t) | 1 | 0.733 | 0.667 | 0.467 | 0.167 |
| Section (3) | | | | | | |
| US: | Occurrence | 16 | 9 | 4 | 0 | 0 |
| | P(T/n) | 1 | 0.448 | 0.138 | 0 | 0 |
| US-Light: | Occurrence | 22 | 1 | 4 | 2 | 0 |
| | P(T/n) | 1 | 0.241 | 0.207 | 0.069 | 0 |

ROC data of observer #1 (Second Reading)
A total of 30 positive trails and 32 negative trails

| Section(1) | Category | 1 | 2 | 3 | 4 | 5 |
|---|---|---|---|---|---|---|
| Section(2) | | | | | | |
| US: | Occurrence | 17 | 2 | 3 | 4 | 4 |
| | P(T/t) | 1 | 0.433 | 0.366 | 0.266 | 0.133 |
| US-Light: | Occurrence | 7 | 4 | 7 | 6 | 6 |
| | P(T/t) | 1 | 0.767 | 0.633 | 0.400 | 0.200 |
| Section (3) | | | | | | |
| US: | Occurrence | 14 | 7 | 11 | 0 | 0 |
| | P(T/n) | 1 | 0.563 | 0.344 | 0 | 0 |
| US-Light: | Occurrence | 24 | 3 | 4 | 1 | 0 |
| | P(T/n) | 1 | 0.250 | 0.156 | 0.031 | 0 |

Table III  ROC data of observer #2 (First Reading)
A total of 30 positive trails and 33 negative trails

| Section(1) | Category | 1 | 2 | 3 | 4 | 5 |
|---|---|---|---|---|---|---|
| **Section(2)** | | | | | | |
| **US:** | Occurrence | 15 | 0 | 4 | 4 | 7 |
| | P(T/t) | 1 | 0.5 | 0.5 | 0.367 | 0.233 |
| **US-Light:** | Occurrence | 6 | 2 | 3 | 7 | 12 |
| | P(T/t) | 1 | 0.800 | 0.733 | 0.630 | 0.400 |
| **Section (3)** | | | | | | |
| **US:** | Occurrence | 4 | 3 | 19 | 5 | 2 |
| | P(T/n) | 1 | 0.879 | 0.788 | 0.212 | 0.061 |
| **US-Light:** | Occurrence | 29 | 0 | 1 | 3 | 0 |
| | P(T/n) | 1 | 0.121 | 0.121 | 0.091 | 0 |

Table III  ROC data of observer #2 (Second Reading)
A total of 30 positive trails and 34 negative trails

| Section(1) | Category | 1 | 2 | 3 | 4 | 5 |
|---|---|---|---|---|---|---|
| **Section(2)** | | | | | | |
| **US:** | Occurrence | 11 | 0 | 4 | 2 | 13 |
| | P(T/t) | 1 | 0.633 | 0.633 | 0.5 | 0.433 |
| **US-Light:** | Occurrence | 5 | 0 | 3 | 8 | 14 |
| | P(T/t) | 1 | 0.833 | 0.833 | 0.733 | 0.467 |
| **Section (3)** | | | | | | |
| **US:** | Occurrence | 5 | 1 | 11 | 12 | 5 |
| | P(T/n) | 1 | 0.853 | 0.823 | 0.5 | 0.147 |
| **US-Light:** | Occurrence | 29 | 0 | 0 | 2 | 3 |
| | P(T/n) | 1 | 0.147 | 0.147 | 0.147 | 0.088 |

FIGURES

# INTENSITY MODULATED LIGHT

laser source (in phase)  laser source (out phase
180 degree)

null plane
or line

no
heterogeneity

heterogeneity

laser detector

laser detector
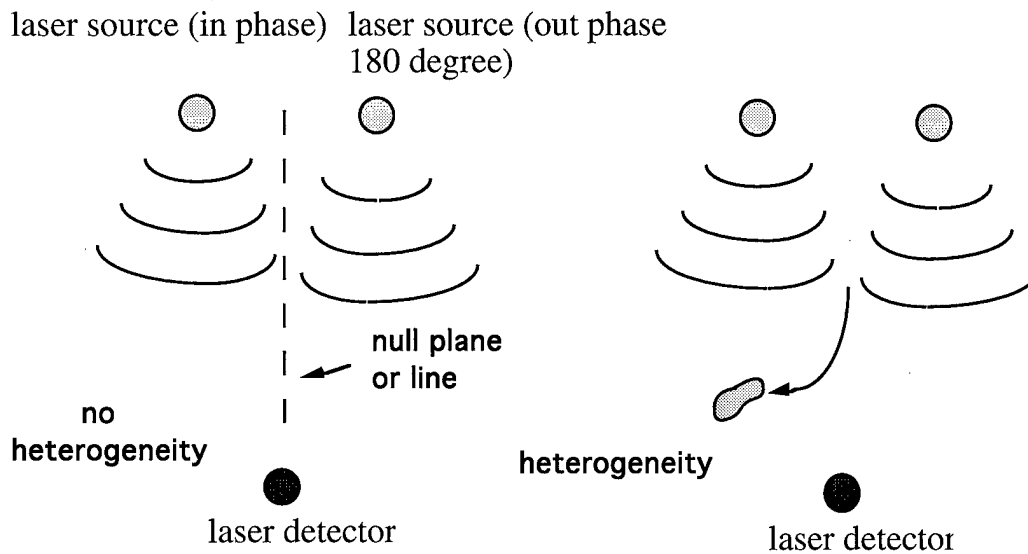
Fig.1. Illustration of object detection by the optical phased array positioner
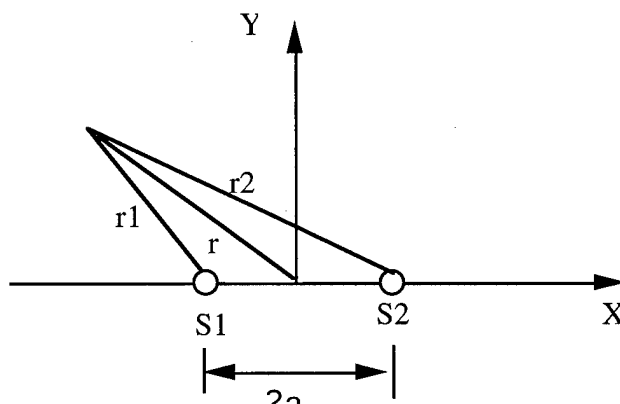
Fig. 2. Optical phased array geometry

2 5
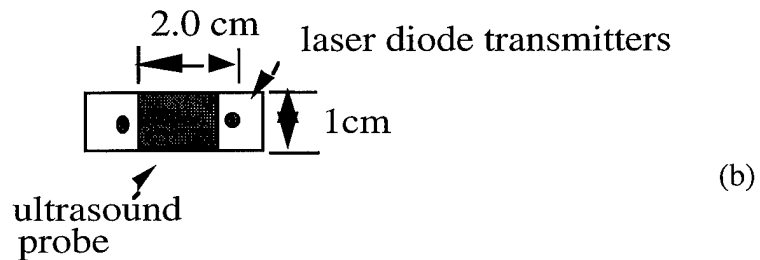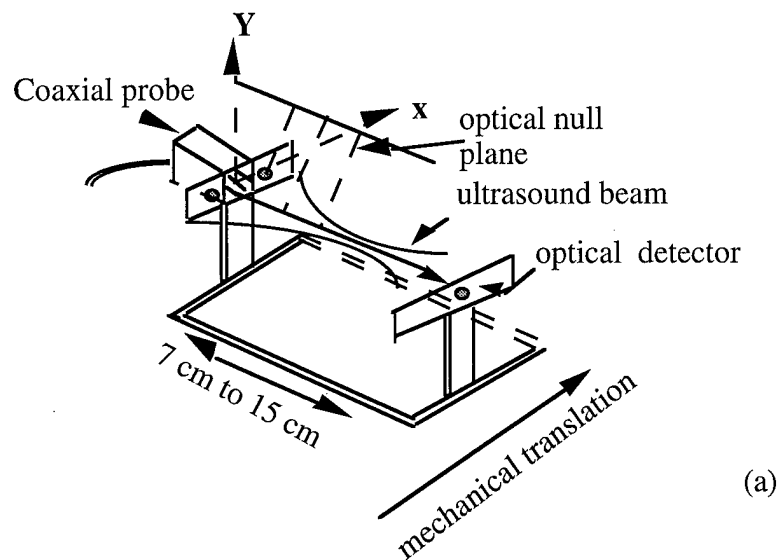
Fig.3. (a) Coaxial ultrasound and optical probe and optical detector assembly. (b) front view of the coaxial probe.
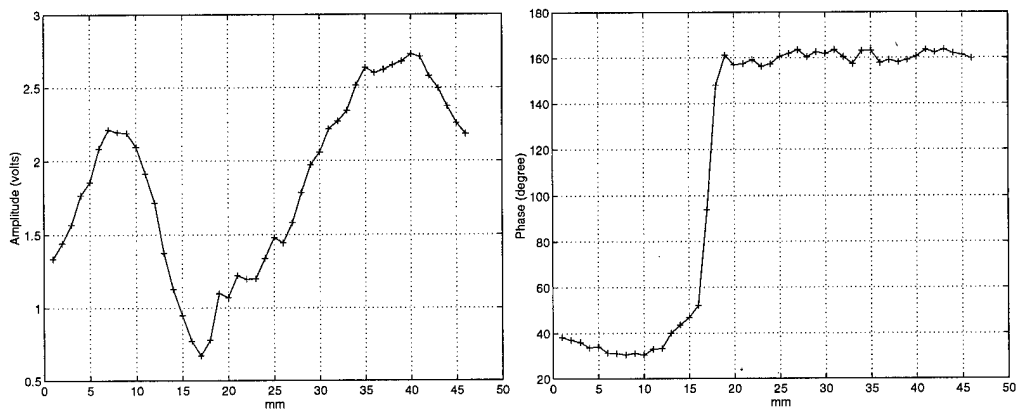
Fig.4. Optical response when concentric black plastic tubes of 1.9 and 1.7 mm diameters filled with 0.5% intralipid were inserted into the scattering phantom. (a) Amplitude response and (b) phase response. The amplitude null and phase transition are indications of the object line-of-sight.
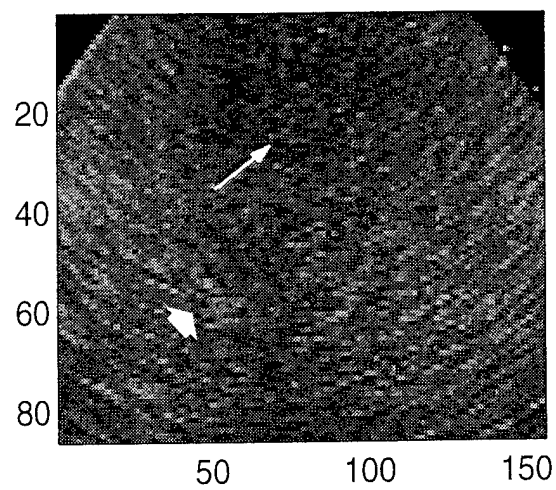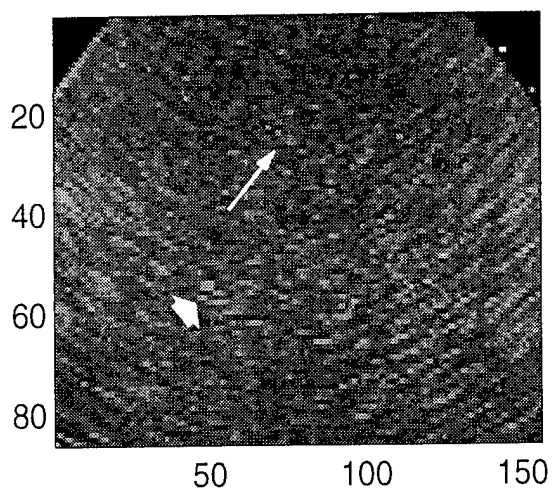
27
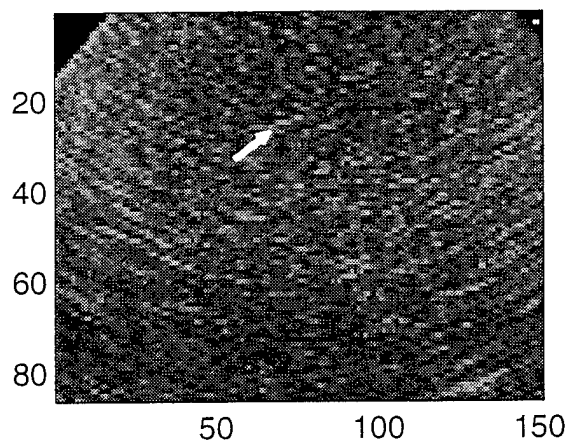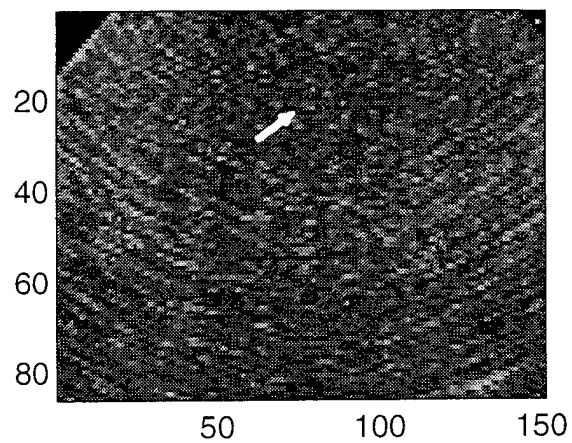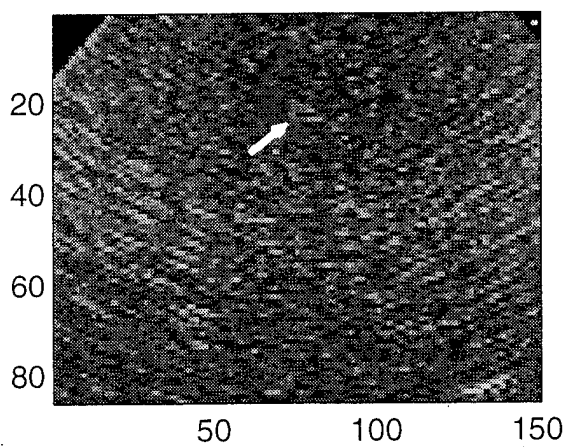
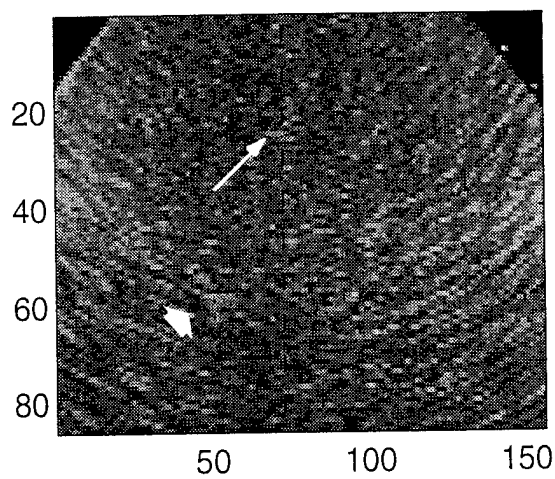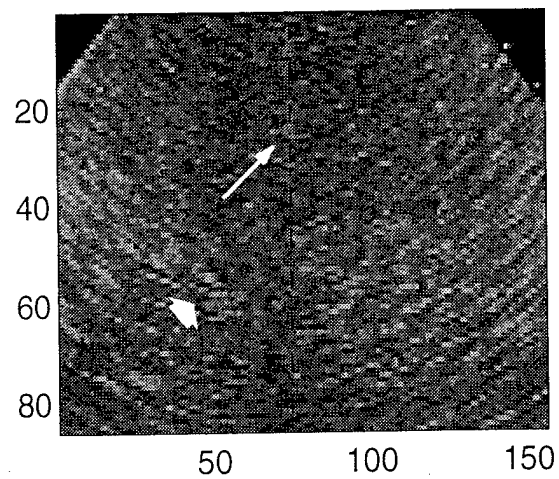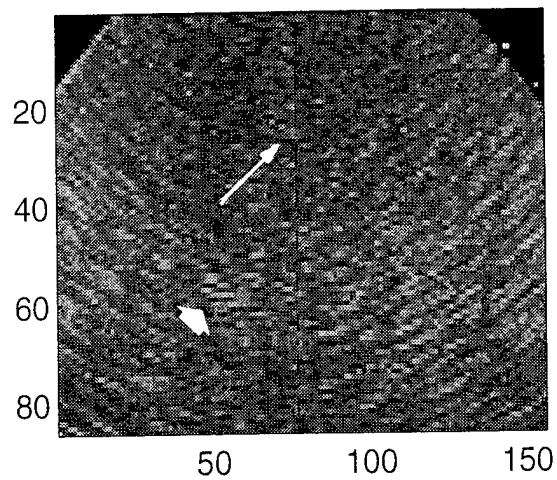Fig.5. The triple images taken at lateral positions 16, 17, 18 mm. Target is indicated by arrow.
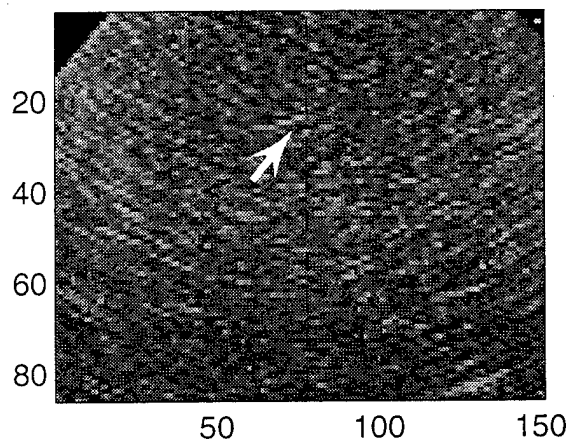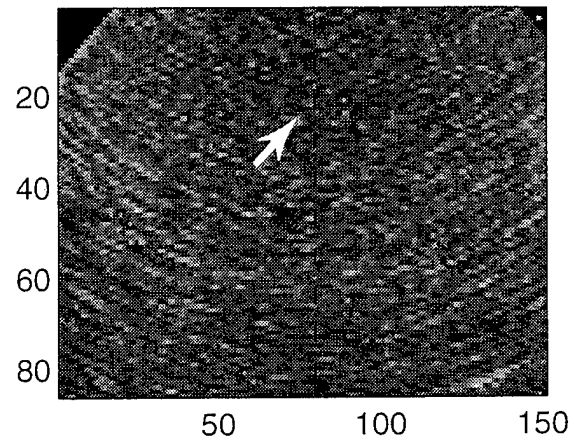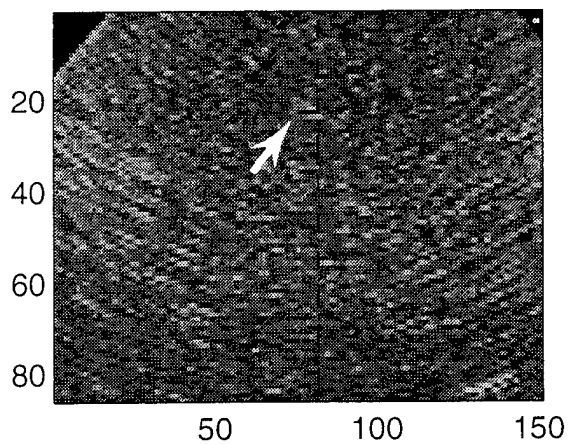
Fig.6. The same triple images as shown in Fig.5 but optical line-of-sight information was coded in the images as indicated by dashed lines. Target is indicated by arrow.
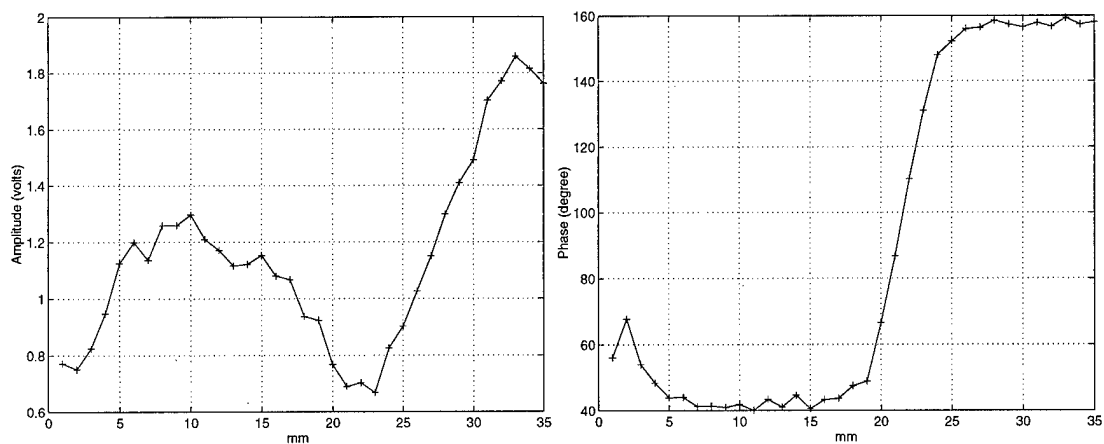
Fig.7. Optical response when a 4.8 mm white Teflon rod was inserted into the scattering

phantom. (a) Amplitude response and (b) phase response. The amplitude null and phase

transition are indications of the object line-of-sight.
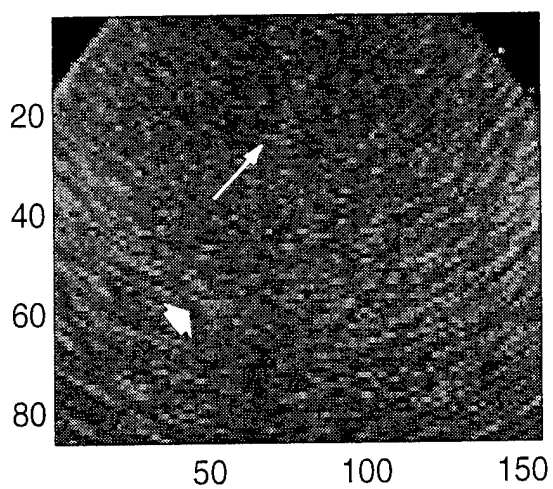
Fig.8. The triple images taken at lateral positions 20, 21, 22 mm. Target and artifact are indicated by arrows. Object is a 4.8 mm white Telfon rod.

Fig.9. The same triple images as shown in Fig.8 but optical line-of-sight information was coded in the images as indicated by dashed lines. Target and artifact are indicated by arrows.
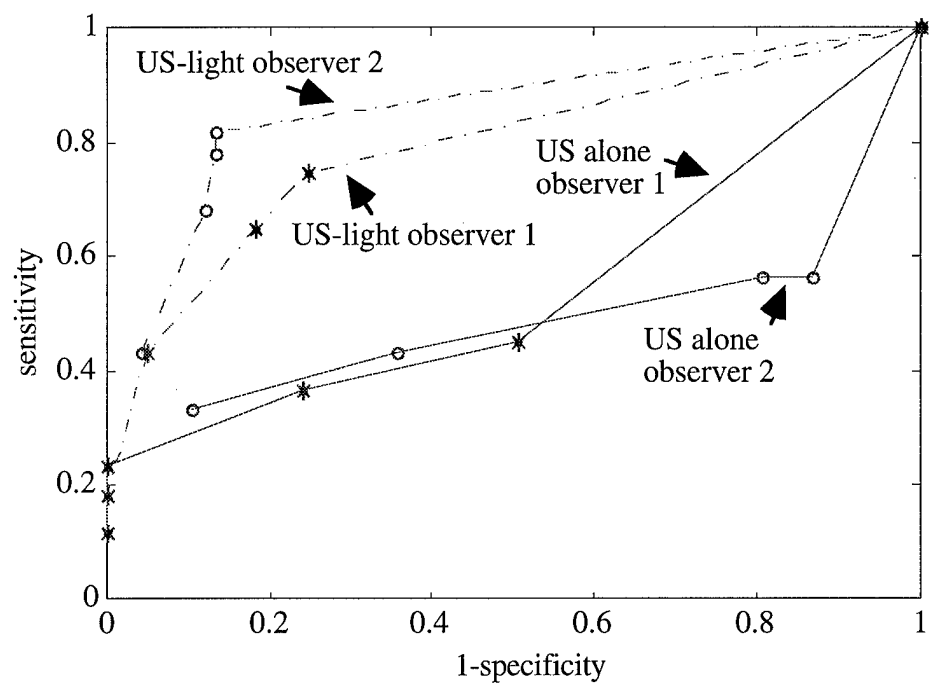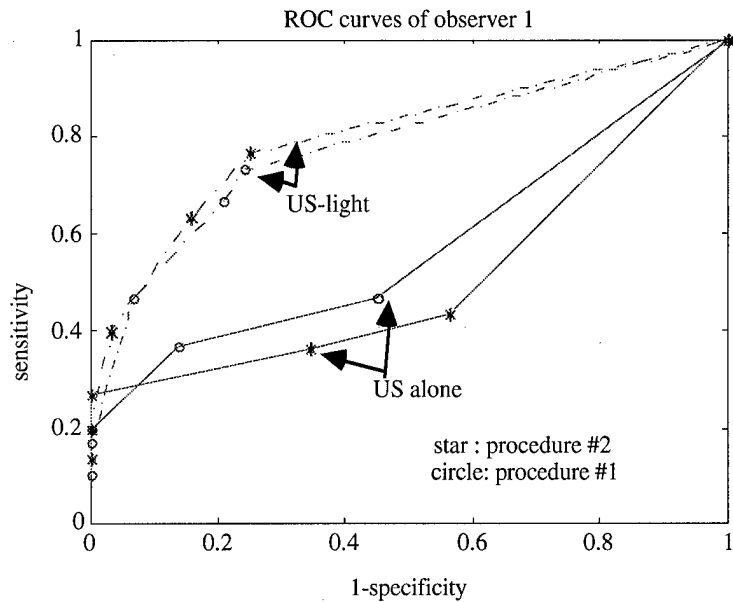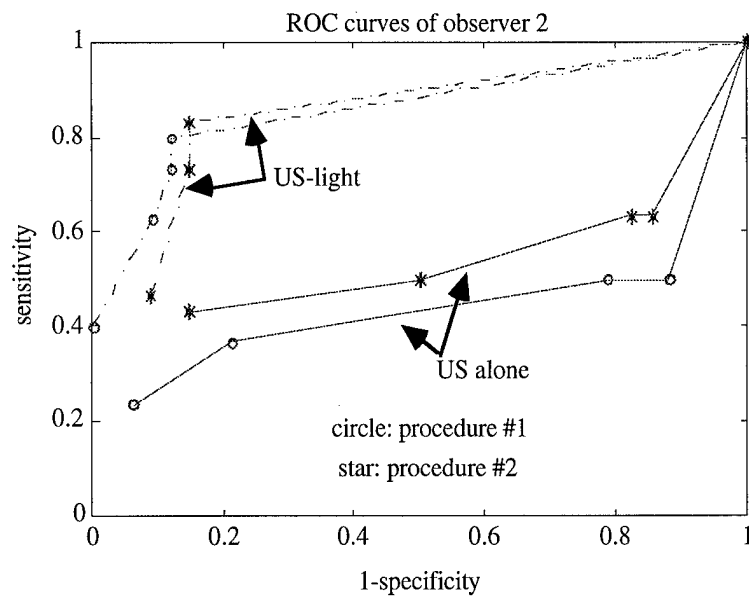
Fig.10. Average ROC curves of two observers. The ROC curves of ultrasound method are plotted in solid lines and ROC curves of ultrasound-light are plotted in dashed lines.

Fig.11. ROC curves measured with two different test procedures. (a) Obtained from observer 1, and (b) from observer 2. Procedure #1 is the ordered test with ultrasound and ultrasound-light images presented in sequence while procedure #2 is the random test with ultrasound and ultrasound-light images presented in random order. The results with both testing procedures are consistent.